

**The Limiting Background in a Detector  
Testing Facility for SuperCDMS at  
SNOLAB**

by

Shuo Liu

A thesis submitted to the Department of Physics, Engineering Physics & Astronomy  
in conformity for the requirements for the degree of Master of Science

Queen's University  
Kingston, Ontario, Canada  
January, 2011

Copyright © Shuo Liu, 2011

## Abstract

SuperCDMS is the next generation of the Cryogenic Dark Matter Search experiment (CDMS), aimed at the detection of the Weakly Interacting dark matter Particles (WIMPs) with the use of phonon and ionization signals in germanium detectors operated at  $\sim 40\text{ mK}$ . The current experiment is operating in the Soudan underground laboratory in northern Minnesota. However, due to limitation of cosmic ray muons, in the next stage of SuperCDMS, the whole experiment will be moved to a deeper site at SNOLAB. This could reduce the influence of extraterrestrial high energy particles to a negligible level, leaving the natural radioactivity locally existing in the laboratory wall rock as the dominating background source. Along with this relocation, newly designed detectors will be implemented to further increase the sensitivity. The prototype of this kind of detector has been manufactured, but it needs to be carefully tested prior to its formal application. To thoroughly examine its performance, especially in an environment that is less affected by cosmic rays, a new detector testing facility is to be built underground at SNOLAB (STF) surrounded by a water tank serving as the passive shield against the natural radioactivity. A series of Monte Carlo simulations have been performed to investigate the effectiveness of the water tank shield, the background level and also the energy spectra of events in the detectors. The goal of  $< 1\text{ neutron/day}$  and  $< 1\text{ Hz}$  of gammas for external sources can be achieved.

# Acknowledgements

I would like to express my gratitude to all those who helped me throughout my years at Queen's.

My deepest gratitude goes first and foremost to my thesis supervisor Dr. Wolfgang Rau for his constant support and guidance. He has walked me through all the stages of my research and also the writing of this thesis. He has set an example of both breadth and depth, whose precision, wisdom and hard work made the Queen's CDMS group rapidly grow during the past two years. Without his consistent and illuminating instruction, this thesis could not have reached its present form.

I am also deeply indebted to Dr. Philippe Di Stefano, who has given me great help and encouragement both in his class and outside the classroom.

The years I have spent at Queen's CDMS group are pleasant and precious. I'd like to give particular thanks to Patrick Nadeau and Joseph Fox, my dear colleges and also good friends who have offered me many help both inside and outside of the lab. My heartfelt thanks to all those who have made the stay at Queen's CDMS group such a pleasure and a privilege: Carlos Martinez, Marc-Antoine Verdier, Yohan Ricci, Chase Crewdson, Kedar Page, Connor Behan, Corey Howard, Maica Clavel, Nasim Fatemighomi.

I also would like to thank Peter Skensved and Bei Cai for offering me their results on the study of the SNOLAB neutron spectrum. Special thanks to Michael Tarka,

who run the SOURCES simulation for me in assistance of my GEANT4 simulation.

Thank you to Victor Golovko who was always ready to answer my questions about the GEANT4 simulation. Without your clear and thorough explanation, my research would have been much more difficult.

Last but not the least, my gratitude also extends to my parents whose assistance and support are never ending.

# Contents

<b>Abstract</b>	i
<b>Acknowledgements</b>	i
<b>List of Tables</b>	vi
<b>List of Figures</b>	viii
<b>1 Introduction</b>	1
<b>2 Dark Matter</b>	3
2.1 $\Lambda$ CDM model . . . . .	4
2.2 Evidence . . . . .	5
2.2.1 Galactic Dynamics . . . . .	7
2.2.2 Gravitational Lensing . . . . .	7
2.2.3 Bullet Cluster . . . . .	8
2.2.4 Cosmic Microwave Background . . . . .	9
2.3 Candidates . . . . .	12
2.3.1 MACHOs . . . . .	12
2.3.2 Neutrinos . . . . .	13
2.3.3 Axions . . . . .	13

2.3.4	WIMPs . . . . .	13
2.4	WIMP Detection . . . . .	17
2.4.1	Collider Production . . . . .	17
2.4.2	Indirect Detection . . . . .	18
2.4.3	Direct Detection . . . . .	21
<b>3</b>	<b>Cryogenic Dark Matter Search</b>	<b>30</b>
3.1	Charge Signal . . . . .	32
3.2	Phonon Signal . . . . .	33
3.2.1	TESs and SQUID . . . . .	34
3.3	Cold Hardware . . . . .	35
3.4	Ionization yield . . . . .	38
3.5	Surface events . . . . .	38
3.6	Current limit . . . . .	39
3.7	SuperCDMS . . . . .	41
<b>4</b>	<b>Monte Carlo Method and GEANT4</b>	<b>42</b>
4.1	Monte Carlo Method . . . . .	43
4.2	The GEANT4 Particle Transport Code . . . . .	43
4.2.1	Terminology . . . . .	44
4.2.2	Validation . . . . .	45
4.3	The Need for Monte Carlo Simulations . . . . .	49
<b>5</b>	<b>Radioactive Backgrounds at SNOLAB</b>	<b>50</b>
5.1	From Soudan to SNOLAB . . . . .	50
5.2	Backgrounds at SNOLAB . . . . .	54
5.2.1	Gamma Backgrounds . . . . .	57

5.2.2	Neutron Backgrounds . . . . .	59
<b>6</b>	<b>GEANT4 Simulation for the SuperCDMS Testing Facility at SNO-LAB</b>	<b>68</b>
6.1	Preliminary Simulation . . . . .	69
6.1.1	Gamma from the laboratory wall . . . . .	71
6.1.2	Neutrons from the laboratory wall . . . . .	72
6.1.3	Radon in the water shield . . . . .	78
6.1.4	$^{60}\text{Co}$ in the water shield . . . . .	81
6.1.5	Conclusion . . . . .	82
6.1.6	Study of influence of cavity size and shape . . . . .	83
6.2	Detailed Simulation . . . . .	85
6.2.1	Geometry . . . . .	86
6.2.2	Surface Spectrum Study . . . . .	90
6.2.3	Results . . . . .	105
6.2.4	Conclusion . . . . .	126
<b>7</b>	<b>Summary</b>	<b>132</b>
	References . . . . .	133

# List of Tables

4.1	Physics processes and models in the simulation . . . . .	47
4.2	Attenuation length of 1 <i>MeV</i> gammas in different materials . . . . .	48
4.3	Mean free path of 1 <i>MeV</i> neutrons in different materials . . . . .	49
5.1	Neutron rates from natural radioactivity and cosmic rays at Soudan .	52
5.2	Muon-induced neutron flux for Soudan and SNOLAB . . . . .	53
5.3	Expected neutron background (10 <i>keV</i> to 40 <i>keV</i> ) for CDMSII at Soudan and SuperCDMS at Soudan and at SNOLAB . . . . .	55
5.4	Norite rock composition . . . . .	56
5.5	Branching ratios (BR) for spontaneous fission of $^{235}\text{U}$ , $^{238}\text{U}$ and $^{232}\text{Th}$ . .	60
5.6	Comparison of neutron yields between SOURCES and the simplified code . . . . .	65
6.1	Nuclear recoils caused by laboratory wall neutrons . . . . .	78
6.2	Most intense gamma from radon and radon progenies' decays . . . . .	79
6.3	Summary on preliminary simulations . . . . .	83
6.4	The 20 most intense gammas from the thorium decay chain . . . . .	95
6.5	The 20 most intense gammas from the uranium decay chain . . . . .	96
6.6	Energy depositions from neutron background simulation . . . . .	107
6.7	Multiple scattering from the neutron background simulation . . . . .	110

6.8	The calculated gamma rate/decay rate for all three radioactive sources	118
6.9	Detector rates in all three laboratory wall gamma simulations.	118
6.10	Detector rates in all three laboratory wall gamma simulations.	119
6.11	Detector rates in all four water shield gamma simulations.	126
6.12	Summary on detailed simulations	127

# List of Figures

2.1	Recent limits on the normalized densities of various universe constituents (matter $\Omega_m = \rho_m/\rho_c$ , dark energy, $\Omega_\Lambda$ ) . . . . .	6
2.2	Rotation curves from a set of spiral galaxies . . . . .	8
2.3	X-ray and lensing image from 1E057-558 . . . . .	9
2.4	Full sky map of temperature of CMB . . . . .	10
2.5	The CMB power spectra . . . . .	11
2.6	WIMPs relic density . . . . .	15
2.7	EGRET gamma ray excess . . . . .	19
2.8	FGST gamma ray excess . . . . .	20
2.9	Upper limits on direct spin-dependent WIMP-proton cross sections .	22
3.1	ZIPs . . . . .	31
3.2	Schematic ionization readout circuit . . . . .	33
3.3	Quasiparticles diffuse from Al layer to TES . . . . .	35
3.4	SQUID amplifier . . . . .	36
3.5	Cutaway view of icebox's innermost can . . . . .	37
3.6	Ionization yield . . . . .	39
3.7	Exclusion curves from the final exposure of the CDMSII . . . . .	40
4.1	20 MeV neutrons on Gd: High Precision Neutron model . . . . .	46

4.2	The geometry of the simulation to calculate the attenuation length for gammas . . . . .	48
5.1	SuperCDMS/CDMSII shield . . . . .	51
5.2	Underground neutron production rate as function of depth . . . . .	53
5.3	Muon flux as a function of depth . . . . .	54
5.4	$^{232}\text{Th}$ chain . . . . .	57
5.5	$^{238}\text{U}$ chain and $^{235}\text{U}$ chain . . . . .	58
5.6	Scheme of $\alpha$ -n interaction . . . . .	61
5.7	Primary neutron spectrum (simplified) . . . . .	63
5.8	Primary neutron spectrum (simplified and revised) . . . . .	64
5.9	Thorium $\alpha$ induced neutron spectrum (SOURCES, before modification)	66
5.10	$\alpha$ induced neutron spectrum (SOURCES, after modification) . . . . .	66
5.11	Three neutron spectra comparison . . . . .	67
6.1	Location of STF . . . . .	69
6.2	Sketch of cutaway view of STF . . . . .	70
6.3	Geometry for the preliminary simulation of gammas from the laboratory wall . . . . .	71
6.4	Energy deposition from $2.6\text{ MeV}$ gammas from the laboratory wall (preliminary simulation) . . . . .	73
6.5	Energy deposition from the laboratory wall gammas (preliminary simulation with the water shield removed) . . . . .	74
6.6	Geometry for the laboratory wall neutrons in the preliminary simulation	75
6.7	Energy spectra of surface neutrons contributed by the whole volume and just by the reflection . . . . .	77

6.8	Energy deposition from the laboratory wall neutrons, preliminary simulation . . . . .	78
6.9	Energy deposition from gammas produced by radon in the water shield	80
6.10	Geometry for the preliminary simulation of $^{60}\text{Co}$ gammas from the steel tank . . . . .	81
6.11	Energy deposition from the $^{60}\text{Co}$ radiation in the steel tank . . . . .	82
6.12	Different regions defined from the preliminary experimental hall . . . . .	84
6.13	Comparison of neutron fluence from different regions . . . . .	85
6.14	Best fit of the F-F section in the tunnel . . . . .	87
6.15	Geometry of the experimental area in the simulation . . . . .	87
6.16	The cryostat and its geometry in the simulation . . . . .	88
6.17	The detector housing and the interior detectors . . . . .	89
6.18	The line source approach . . . . .	91
6.19	Different regions selected from the current geometry . . . . .	92
6.20	Distribution of different escaping particles as collected from the line source test . . . . .	93
6.21	r-histogram for the line source spread . . . . .	94
6.22	Comparison of the fluence of gammas from the thorium decay chain from different regions . . . . .	97
6.23	Comparison of the fluence of gammas from the uranium decay chain from different regions . . . . .	98
6.24	Hypothesis test for the thorium gamma fluence comparison . . . . .	99
6.25	Hypothesis test for the uranium gamma fluence comparison . . . . .	100
6.26	The excess of corner fluence below 500 keV for both decay chain gammas	101
6.27	The line source gamma spectra for the thorium decay chain, the uranium decay chain and for $^{40}\text{K}$ . . . . .	102

6.28	Neutron spectrum as calculated by SOURCES . . . . .	103
6.29	Comparison of the fluence of the background neutrons from different regions . . . . .	104
6.30	Hypothesis test for the neutron fluence comparison . . . . .	105
6.31	The neutron surface spectrum . . . . .	106
6.32	Nuclear recoils from background neutrons . . . . .	108
6.33	Energy deposition from background neutrons (without water shield) .	109
6.34	Coincidence between two detectors in the background neutron simulation	111
6.35	Initial position distribution of the detected background neutrons . . .	112
6.36	2D view of the initial background neutron position distribution in the selected regions . . . . .	113
6.37	Energy distribution of the initial background neutrons in the selected regions . . . . .	115
6.38	Energy deposition from the laboratory wall thorium decay chain gammas	116
6.39	Coincidence between two detectors in the thorium decay chain gamma simulation . . . . .	117
6.40	Initial position distributions of the detected thorium gammas . . . . .	120
6.41	2D view of the initial position distribution for the thorium gammas in the selected regions . . . . .	121
6.42	The bottom region vertex distribution of the detected thorium gammas from different simulations . . . . .	122
6.43	Energy distribution of the initial thorium chain gammas in the selected regions . . . . .	124
6.44	Detector depositions from radon contamination in the water shield .	125
6.45	Position distribution of the primary vertices in the preliminary neutron study . . . . .	130

# Chapter 1

## Introduction

This thesis is to record my graduate research as I worked with the Cryogenic Dark Matter Search experiment. The goal of the CDMS experiment is to find dark matter, the mysterious component of the universe. Chapter 2 gives a brief introduction of the  $\Lambda$ CDM model, the theoretical frame work of current cosmology, and various evidence to support the existence of dark matter. The major dark matter candidates are also listed, which are given by different underlying theories and specific experiments are designed to probe each candidate. The weakly interacting massive particle (WIMP), which is the targeted particle dark matter in the CDMS experiment, is particularly emphasized. Details including its theoretical origin and other competing experiments beyond CDMS are described in the context. CDMS is detecting WIMPs by directly looking for their rare scattering with terrestrial materials. The enormous rate of background radiation places a major obstacle in this endeavor. To distinguish the potential WIMP signal from the backgrounds by which it is awash, CDMS employs cryogenic germanium detectors simultaneously measuring phonon and ionization signals in a well shielded experimental setup. Together with the most recent result from the CDMS experiment, its detector design, readout electronics and cryogenic systems

are discussed in chapter 3.

Since no dark matter signal has been identified from the measurement, CDMS is searching for a new detector design and advanced shielding strategy to increase the sensitivity. A prototype of the newly designed detector has been produced, but its performance test is not complete since the tests are carried out on the Earth surface where the detectors are exposed to numerous sources of background radiation. To continue the test, a new detector testing facility is proposed to be built 2000 m underground at SNOLAB near Sudbury, Ontario, which is also the site for the future generation of the CDMS experiment. At this depth, the cosmic rays are largely blocked, leaving the natural radioactivity from the laboratory wall as the dominating backgrounds source, which could be efficiently mitigated by a sufficient amount of water. The main part of this thesis is a study of the effectiveness of this water shielding via the use of GEANT4 Monte Carlo simulation. In chapter 4, the basic idea and major advantage of the Monte Carlo method is discussed, with an emphasis on the GEANT4 particle transport code. Chapter 5 examines the main natural radioactive sources present at SNOLAB, providing information about the background particles to be studied in the simulations. Chapter 6 gives the results from the analysis of the simulation and the conclusion drawn.

# Chapter 2

## Dark Matter

The nature of the universe has haunted human beings since antiquity. Philosophy is one of the early attempts of our ancestors towards this fascination. Science has long been a branch of this broad subject. Until several hundred years ago, it gradually became independent and eventually overwhelmed other disciplines. Science receives reputation from the secular world by its unprecedented power in shaping our planet, building up confidence inside the ivory tower by providing an authoritative deep insight into fundamentals that otherwise can only be attributed to a deity. By the 1970s, scientists could already explain the world from the smallest inseparable component (quark), to the largest structures that quarks can form in the universe. However, this is far from the whole story. It seems that the unseen, and so far undetected dark components - “dark energy” and “dark matter” dominate the universe. Numerous experiments have been operated in search for them, especially the dark matter, which is only known by its gravitational effects. A thorough understanding of this mysterious existence is not only the goal of modern physicists, but also a recall to the long existing human instinct: to know everything.

## 2.1 $\Lambda$ CDM model

Cosmological observations show the universe is isotropic and homogeneous on the largest scale, while its evolution is never ceasing since the big bang. Thus a theory describing its evolution regardless of local anisotropy is possible. To put the universe into an equation, three categories into which everything in the universe should fall in are proposed: non-relativistic matter, radiation (photons and other relativistic matter) and vacuum energy (dark energy, intrinsic energy density of space itself). Their densities, the quantities that show up in the equation are defined and normalized by a critical density (the density when the universe is “flat”):  $\rho_c \equiv \frac{3H^2}{8\pi G}$  ( $G$  stands for Newton’s Gravitational Constant and  $H$  represents the Hubble parameter). The normalization goes like:  $\Omega_x \equiv \rho_x/\rho_c$ . With these standardized variables, Friedmann equations, or time evolution equations for the universe can be expressed as:

$$\Omega - 1 = \frac{kc^2}{a^2 H^2} \quad (2.1)$$

$$\dot{H} = -H^2(1 + \frac{1}{2}\Omega_m + \Omega_r - \Omega_\Lambda) \quad (2.2)$$

Where  $a$  is the universe scale factor, ever increasing as time elapses.

The  $\Lambda$ CDM model is a combination of above set of equations and boundary conditions measured at present time:  $\Omega \approx 1$  (a nearly ‘flat’ universe), negligible  $\Omega_r$  compared with  $\Omega_{0,m}$  and  $\Omega_{0,\Lambda}$ . It is the concordance model of modern cosmology, with  $\Lambda$  representing the cosmological constant, the simplest candidate for vacuum energy, CDM standing for cold dark matter, indicating dark matter was non-relativistic during the structure-formation period.

This theory is in broad agreement with a range of distinct measurements (Figure

2.1): Experiments towards baryon acoustic oscillations, cosmic microwave background, and Type Ia supernovae are among its supporters. They together provide a constrained set of cosmological parameters:

- Baryon density  $\Omega_{0,b} = 0.0456 \pm 0.0015$
- Dark matter density  $\Omega_{0,cdm} = 0.228 \pm 0.0013$
- Dark energy density  $\Omega_{0,\lambda} = 0.726 \pm 0.015$

This result implies that the unseen cold dark matter contributes 23% of universe total energy density, whereas baryonic matter only makes up 4.6%.

## 2.2 Evidence

Through decades of study, scientists have collected a wide variety of evidence in favor of existence of dark matter. Although the various evidence are superficially distinct from each other, they are all based on gravitational effects: either modern signatures or primordial relics showing influence of unseen material on detectable matter.

The first such attempt is by Fritz Zwicky in the 1930s [2]. He measured redshift of several galaxies in the Coma cluster, which offered information about its dynamics sampled in different positions inside the structure. Because the cluster has been formed for a long time, the virial theorem can be used to calculate its gravitational mass.

$$2 \langle T \rangle = - \langle V \rangle \sim \frac{GM_{cluster}^2}{2 \langle r \rangle} \quad (2.3)$$

He then deduced the total mass of constituent galaxies independently from their luminosity inside the cluster. An unexpected result came out as the gravitational

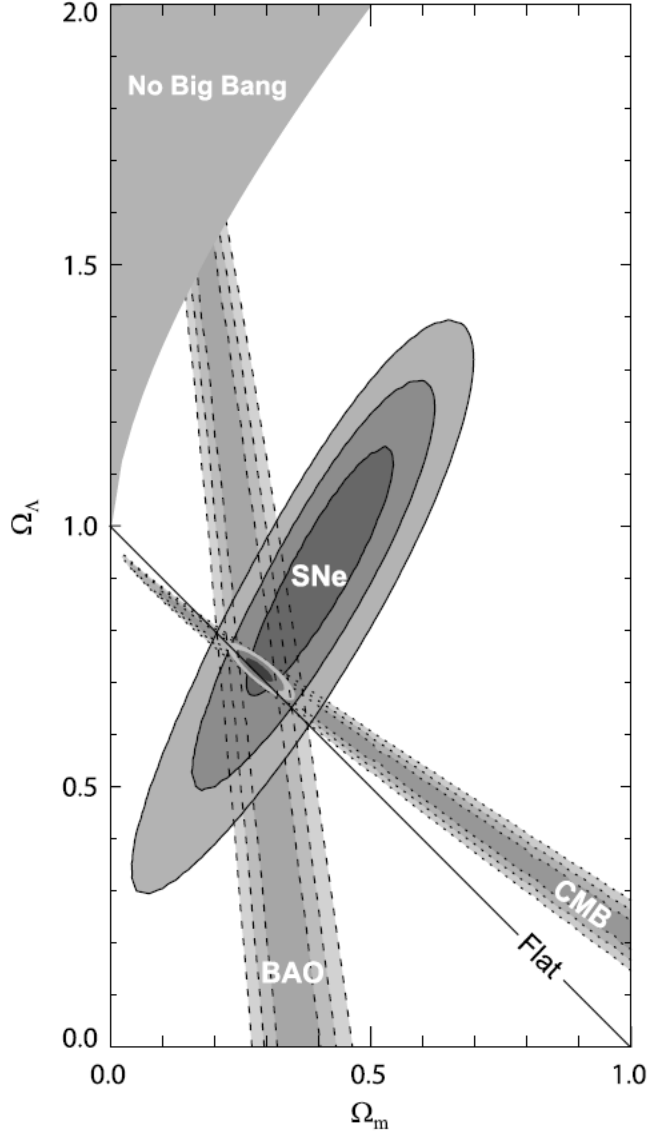


Figure 2.1: Recent limits on the densities of various universe constituents (with  $\Omega_m = \rho_m/\rho_c$  being the matter density and  $\Omega_\Lambda$  being the density of the dark energy). Data from measurements of baryon acoustic oscillations (BAO), the cosmic microwave background (CMB), and Type Ia supernovae (SNe).  $1\sigma$ ,  $2\sigma$ ,  $3\sigma$  confidence regions are presented. Figure from [1]

mass outnumbered the other one by a factor of 400, implying some unseen components dominated the structure. Although his result was inflated by a limited knowledge of the Hubble parameter, modern approaches with more sophisticated technology and

more abundant data sets a similar abnormality.

### 2.2.1 Galactic Dynamics

Dynamics of spiral galaxies are among the most straightforward and intuitive signatures of dark matter. The luminous part of a spiral galaxy is made up of a dense bright central bulge and the surrounding dim dilute halo. By measuring redshift of various spectral features embedded inside a galaxy, its rotation speed curve can be deduced. According to Newtonian dynamics, the rotation curve should rise at a lower radius as the entire bulge is not yet included, and fall down as  $\sim \frac{1}{\sqrt{r}}$  when leaving from the core region. However, this naive expectation goes contrary to observations. The earliest evidence was from 1970, when Rubin and Ford studied Doppler shifts in the Andromeda galaxy and found a plateau in rotational velocity distribution in both disk and outer halo [3]. This indicates the mass of spiral galaxy is proportional to radius ( $M \propto r$ ) if assuming mass is distributed spherically. Light thus does not reflect the real mass of galaxy. A significant fraction of the entire mass is unseen. The missing part is believed to be in the form of dark matter, locating in the galaxy halo. Without the substantial contribution of this 'dark matter halo', the galaxy would fall apart (Figure 2.2).

### 2.2.2 Gravitational Lensing

One of the most prominent conclusions drawn from General Relativity lies in the fact that the path of light can be bent by the matter it passes. The deflection angle  $\alpha$  can be expressed as a function of mass  $M$  and its distance from light  $r$ :

$$\alpha = \frac{4GM}{c^2} \frac{1}{r} \quad (2.4)$$

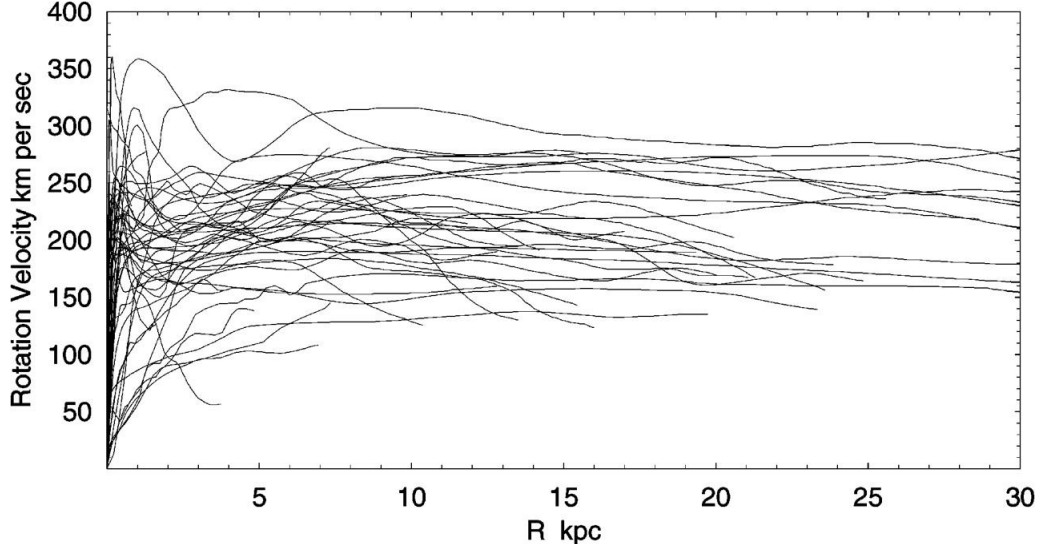


Figure 2.2: Rotation curves from a set of spiral galaxies. Although behaviors close to center region vary dramatically, plateaus can be seen in each of them at large radii. Figure from [4]

By analyzing distortion or multiplication of images from distant background sources, one can deduce the mass distribution of the lensing matter in between that alters the light path. This method is known as gravitational lensing. Because it doesn't require an assumption of virial equilibrium as in the galactic rotation curve method, gravitational lensing serves as an accurate probe in uncovering the amount of dark matter in clusters.

### 2.2.3 Bullet Cluster

The strongest support for dark matter hypothesis to date comes from 1E057-558, better known as “bullet cluster” [5]. This is a pair-cluster consisting of two clusters in the process of colliding with each other. Dark matter does not join the collision due to its non-collisional nature, so do not the luminous galaxies. Galaxies only occupy a small volume inside the clusters, so the chance they can meet each other is very

small in a collision. The collision can only manifest itself by the presence of ICM (intracluster medium). Although ICM is not as bright as stars, it contributes 90% of baryonic mass and occupies vast space in the cluster. It is then denser than stars on large scales and can collide. Since ICM is very hot (10-100 *million K*) and emits X-rays, it is the most prominent feature when observing the bullet cluster. However, ICM is not representing the majority of the cluster's mass. Through careful study of gravitational lensing, the mass distribution of the bullet cluster shows the most massive components of clusters are non-collisional in nature and are not affected by the merging process, indicating dark matter might provide most mass (Figure 2.3).

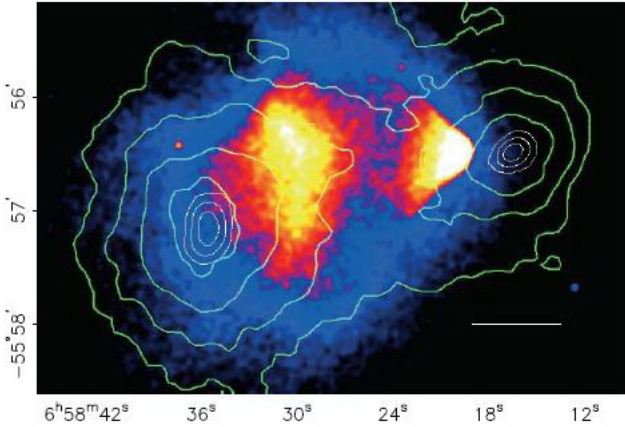


Figure 2.3: X-ray and lensing image from 1E057-558. Figure from [5]

## 2.2.4 Cosmic Microwave Background

Dark matter is supposed to have played an important role in shaping the primordial universe [6]. Its non-collisional nature helps forming over densities presented in the early universe. These over densities, on the order of  $10^{-5}$ , evolve into clumps of matter, and later galaxies as the universe expands. People then seek relics from the early universe to support this hypothesis. A well known evidence of this type is the

cosmic microwave background, or CMB for short.

The big bang brings enormous heat to the primordial universe. It had extremely high temperatures at this point that baryons remained isolated and can't form into atoms. They were instead homogeneously distributed in space, rendering a dense early universe essentially opaque to photons. Photons then bounced frequently on baryons which gave rise to a considerable radiation pressure overlaid on gravity. Due to compelling nature of the radiation pressure, and attraction enforced by gravity, the original homogeneous photon-baryon fluid began to oscillate, from which inhomogeneity first came to the universe. Baryons and dark matter are believed to have different impact on the oscillation: Baryons were confined by radiation from photons thus magnifying the oscillation, while dark matter rarely interacted with photons and essentially reduced the amplitude.

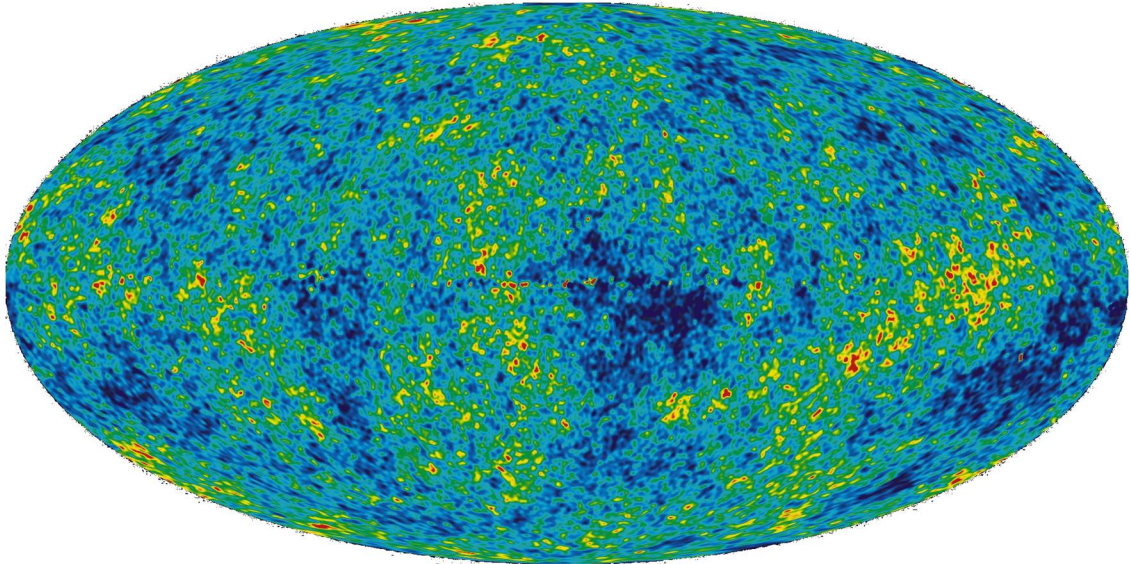


Figure 2.4: Full sky map of temperature of CMB, using WMAP 5 years data [7], indicating small temperature fluctuations. WMAP Science Team

From the knowledge of magnitude of the oscillations, one can get the relative

abundance of baryon and non-baryon components at that time. This information is stored in the CMB, or the redshifted relic of blackbody radiation since "the last scattering". As the universe spreads out, the temperature goes down below the ionization energy of hydrogen, and atoms begin to form and the universe becomes transparent to photons. The photons' last scattering on isolated baryons or electrons results in the CMB, which exhibits inhomogeneity in the universe at that point.

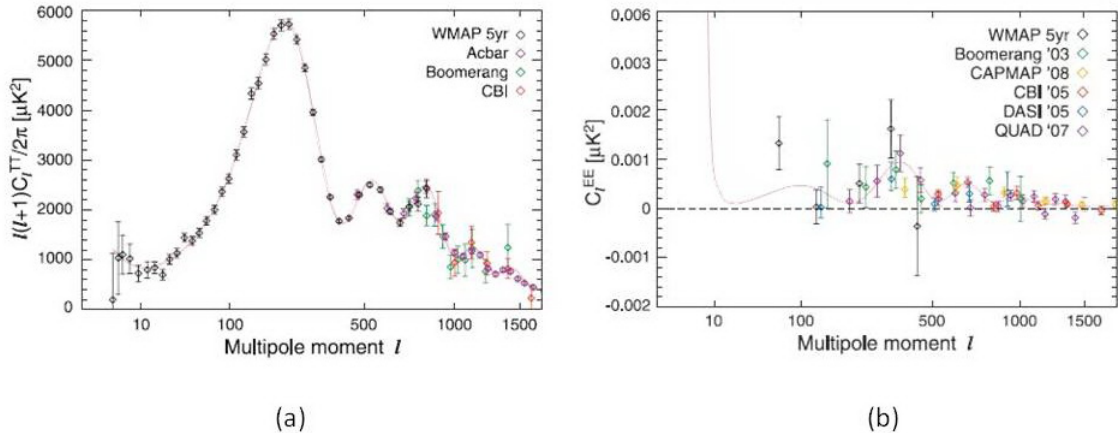


Figure 2.5: The CMB power spectra, data from 5 years WMAP, together with other experiments, drawn from [8]. Curves in both spectra indicate the prediction of the best fit  $\Lambda$  $CDM$  cosmology. (a) Temperature power spectrum, showing temperature anisotropy of CMB; (b) Polarization power spectrum, exhibiting polarization inhomogeneity of CMB.

The CMB is  $2.73\text{ K}$  on average. Fluctuation begins to show up if one traces down to  $10\text{ }\mu\text{K}$ (temperature fluctuation) or  $0.1\text{ }\mu\text{K}$ (polarization fluctuation) scales. By analyzing position and magnitude of peaks presented in the power spectrum (Figure 2.5), one can work out dark matter abundance and other cosmological parameters. Five years efforts by the Wilkinson Microwave Anisotropy Probe (WMAP) provides the best CMB data to date, indicating that non-baryonic dark matter outweighs its

baryonic opponent by contributing 21.4% of total energy density in the universe.

## 2.3 Candidates

The cold, nearly non-interacting, non-baryonic and stable nature of dark matter represents our limited knowledge of this mysterious fundamental cosmological component. Inspired by a wide variety of evidence, many candidates have been proposed. They either have been ruled out or still await confirmation from different experiments. A better understanding of the dark matter is expected to begin the era of new physics beyond the standard model.

### 2.3.1 MACHOs

The simplest and naive solution to the dark matter problem comprises Massive Compact Halo Objects (MACHOs). Possible candidates are non-luminous baryonic objects such as white dwarfs, brown dwarfs, neutron stars, black holes, cold hydrogen gas clouds that inhabit in the galactic halo. Conclusions from big-bang-nucleosynthesis [9] and the cosmic microwave background have independently ruled out the possibility that baryonic MACHOs are the primary constituents of dark matter, as they all predict a approximately 5% contribution from baryons to the total universe energy density.

Besides evidence from the primordial universe, several collaborations have set to study MACHOs directly via gravitational lensing. By measuring change in luminosity of a distant star when MACHOs come in the way between the observer and the source, the EROS experiment has given limits on the presence of those dark objects. Their result published in 2007 denied MACHOs (from  $0.6 \times 10^{-7}$  to 15 solar mass) as a candidate constructing the bulk of dark matter [10].

### 2.3.2 Neutrinos

Neutrinos are experimentally proven dark matter candidates, arising from the Standard Model. They have mass and are non-baryonic particles. But they can't be a major component of dark matter due to their relativistic nature, which would otherwise spoil large scale structure formation.

### 2.3.3 Axions

CP violation in the strong interaction is expected according to quantum chromodynamics (QCD), although experimental evidence has not been found. Unlike in the weak force, where the first observation of CP violation occurred in 1964 when an unbalance was found in a transform between neutral kaons and their antiparticles [11], extra theory is needed to explain the non-observation of strong CP violation. A well known modification was proposed by Peccei and Quinn in 1977 [12]. They suggested a new global  $U(1)$  symmetry, the spontaneous breaking of which results in a CP symmetry in QCD, as well as a new boson, the axion. Axions are hypothetically non-relativistic particles, created non-thermally in the early universe, with a very small mass ranging from the  $\mu eV$  to the meV scale, thus making them wonderful dark matter candidates. Many experiments are looking for axions, although they have not yet been detected. The leading experiment ADMX [13] probes the  $\mu eV$  level is approaching parameter space favored by cosmological models.

### 2.3.4 WIMPs

Dark matter candidates may also be massive non-baryonic particles. The leading hypothetical particle of this type is the weakly interacting massive particle (WIMP). WIMP is the name of a generic class of particles with GeV to TeV masses, moving

non-relativistically, having weak interaction scale cross sections [14]. The lightest Kaluza Klien particle from extra dimension theory [15] and the lightest neutralino from supersymmetry are believed to be the most promising members from this family. Besides strength gotten from physics on the smallest scale, WIMPs are also supported by cosmological hypothesis, as described below.

### Relic from the early universe

WIMPs are believed to have been created after the big bang in the primordial universe. They were initially mixed with baryons and photons in thermal and chemical equilibrium. The balance was fueled by a competition between thermal creation and annihilation of WIMPs. When the universe continued expanding and temperature went down ( $k_B T < M_\chi$ ), thermal creation was eventually becoming inefficient, resulting in an exponential reduction of the WIMP equilibrium density:

$$n_\chi^{(eq)}(T) \simeq g \left( \frac{M_\chi kT}{2\pi\hbar^2} \right)^{3/2} e^{-\frac{M_\chi c^2}{kT}} \quad (2.5)$$

The rate of the competing annihilation process is given by:

$$\Gamma_{\chi\chi} = n_\chi \langle |\sigma_{\chi\chi} v| \rangle \quad (2.6)$$

Where  $n_\chi$  is WIMPs density,  $\langle |\sigma_{\chi\chi} v| \rangle$  is the thermally averaged cross section weighted by velocity. Since the equilibrium density is exponentially reduced as the universe dilutes, at a so called thermal 'freeze out' time, the annihilation process phases out and the remaining WIMPs fix the relic density (Figure 2.6):

$$\Omega_\chi h^2 \simeq \frac{0.1 pb \cdot c}{\langle |\sigma_{\chi\chi} v| \rangle} \quad (2.7)$$

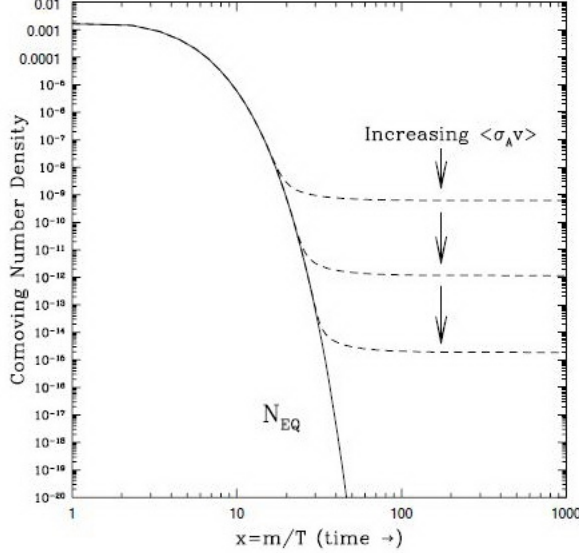


Figure 2.6: WIMPs comoving number density as temperature goes down. The solid line represents the stage when particles are still in thermal equilibrium; the dashed lines indicate the freeze out for different cross sections; The final density is varying as different choices of annihilation cross section. Picture taken from [16]

Equation 2.7 indicates a WIMP-WIMP interaction cross section of the order of picobarn, if implementing the non-baryonic dark matter relic density from recent experiments ( $\Omega_{cdm} h^2 \sim 0.1$ ). This is within the strength of the weak force, implying that the WIMP mass is in the weak scale ( $\sim 100 \text{ GeV}$ ). Particles of this type don't exist in the Standard Model (SM), while physics beyond SM such as supersymmetry, is able to give convenient candidates.

### Supersymmetric WIMPs

Supersymmetry was firstly proposed to explain hierarchy problem: why is the mass of the Higgs boson ( $\sim 100 \text{ GeV}$ ) free of the radiative loop correction which would otherwise raise it to the Planck scale ( $\sim 10^{19} \text{ GeV}$ )? According to the Standard Model, the Higgs boson results from a spontaneous breaking of an  $SU(2) \times U(1)$  gauge symmetry into a  $U(1)$  symmetry, a mechanism that gives a large mass to the

gauge bosons of the weak interaction ( $W^\pm, Z^0$ ). The Higgs is a scalar boson, and thus not subjected to any confining symmetries. The loop correction would make its mass far larger than the weak scale, if no extra physics is available to prevent that. Supersymmetry can elegantly solve this problem by introducing super partners to every SM particle: all super partners have the same quantum numbers as their SM counterparts, but with different statistics - a SM fermion corresponding to a SUSY (Supersymmetry) bosonic particle, a SM boson corresponding to a SUSY fermionic particle. Since bosons and fermions have different statistics, notably different signs, their contributions are canceled out precisely in the radiative correction term, leaving the mass of a particle confined [17].

SUSY particles are heavier than SM particles, otherwise they would have already been discovered in nature. The lightest super partner (the lightest supersymmetric particle, or LSP) is believed to be stable and have a mass in the weak scale ( $\sim 100\,GeV$ ). Its stability comes from a new symmetry, known as R parity. All SM particles have R parity of 1, while super partners all have R parity of -1. If R is conserved, the lightest SUSY particle has no daughter particle to decay into, and thus must be stable.

The weak scale stable LSP was introduced as a Majorana neutralino, a mixture of super partners of photon, Z boson and two lightest Higgs bosons (photino, zino, Higgsinos respectively). A Majorana neutralino is thus a wonderful dark matter candidate [18], for it can annihilate with itself, a property allowing its density to be regulated thermally in the early universe.

The ability that the neutralino can relate physics on various scales makes it a promising WIMPs candidate. A lot of experiments have set out to search for it via different approaches, aimed at new physics beyond the current stage.

## 2.4 WIMP Detection

A WIMP is expected to reveal itself in either direct or indirect detection experiments, though none of these experiments have reported a convincing finding. Besides studies over primordial WIMPs, extremely high energy particle colliders, such as the Large Hadron Collider (LHC) currently operating at TeV energy scale, would produce dark matter particles directly as predicted by supersymmetry.

### 2.4.1 Collider Production

The Large Hadron Collider is probing the energy range where new physics beyond the Standard Model might dominate [19][20][21]. One of its primary goals consists of creating Higgs bosons, a vital evidence in examining the current theory of the hierarchy problem. TeV scale Supersymmetric particles, or WIMP candidates are also believed to be produced in the collider if the underlying theory is correct. Since a WIMP rarely interacts with ordinary matter, detectors surrounding the colliding point would not detect it. But a fairly large amount of missing momenta or energies can be found if a WIMP indeed passes by. Since new colored TeV scale particles are predicted by many WIMP related theories (such as squarks and gluinos from supersymmetry), which might decay into WIMPs and daughter partons, hadronic jets are expected to be another prominent signature during a WIMP production in LHC [22]. Once many WIMP events are reconstructed, the WIMP mass can be statistically confined. However, collider experiments can't fully determine all relevant WIMP properties. Parameters like stability and interaction cross sections are to be discovered by direct and indirect experiments.

## 2.4.2 Indirect Detection

Instead of finding WIMPs locally out of hadron debris, astrophysicists have built large telescopes, looking for traces of dark matter annihilation products. Since dark matter may not be evenly distributed all throughout the universe, in places like galactic cores a WIMP over density is expected, WIMP annihilation would take place where they are densely populated. Annihilation products may include gamma rays, leptons, or neutrinos depending on different theoretical models. They are generally extremely high energy particles due to the high mass of the WIMPs, capable of traveling extragalactic distance to reach terrestrial detectors. Indirect dark matter searches might outweigh direct method when the terrestrial WIMP density is much lower than most direct experiments currently assume.

### Gamma rays

Gamma rays are among the most promising WIMP annihilation signatures, for they can pertain directional information and keep energy rarely altered through long distance transportation. The gamma spectrum is expected to be either in a GeV-TeV range feature overlaid on the cosmological background, or an unusual hard continuum spectrum with a sharp cut off energy at a hypothesized WIMP mass. The former is easily distinguishable in principle, but difficult to be observed in practice, because annihilation channels rendering monoenergetic gamma are suppressed by theory and those gammas are usually merged with backgrounds due to poor telescope resolution. As a result, the not so straightforward continuum spectrum is pursued by nearly all related experiments.

One feasible way to detect such high energy gamma rays is through a space based telescope. The Energetic Gamma Ray Experiment Telescope on the Compton Gamma Ray Observatory (EGRET) is an example. They announced a GeV range gamma ray

excess, and suggested it could be explained by a  $\sim 60\text{ GeV}/c^2$  WIMP annihilation [23](Figure 2.7). However, this result is not decisive and some of its collaborators have already claimed the signal might be due to instrumental calibration errors [24].

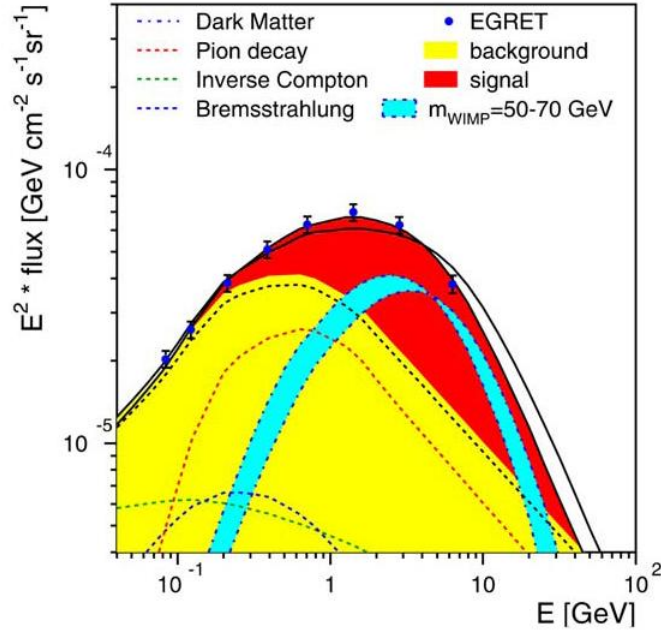


Figure 2.7: The Gamma ray excess claimed by EGRET, the WIMP explanation is also plotted (cyan). Picture taken from [23]

The recently launched Fermi Gamma-ray Space Telescope (formerly known as “GLAST”) provides an unprecedent powerful insight into gamma ray excess. It has just analyzed the first two years of data from a survey of our galactic center [25]. The observed spectrum from within approximately  $1.25^\circ$  ( $\sim 175\text{ parsecs}$ ) of the galactic center cannot be explained by any known astrophysical processes, while gamma emission from a  $7.3\text{GeV}-9.2\text{GeV}$  dark matter annihilation (primarily to tau leptons) provides a good fit to the data (Figure 2.8).

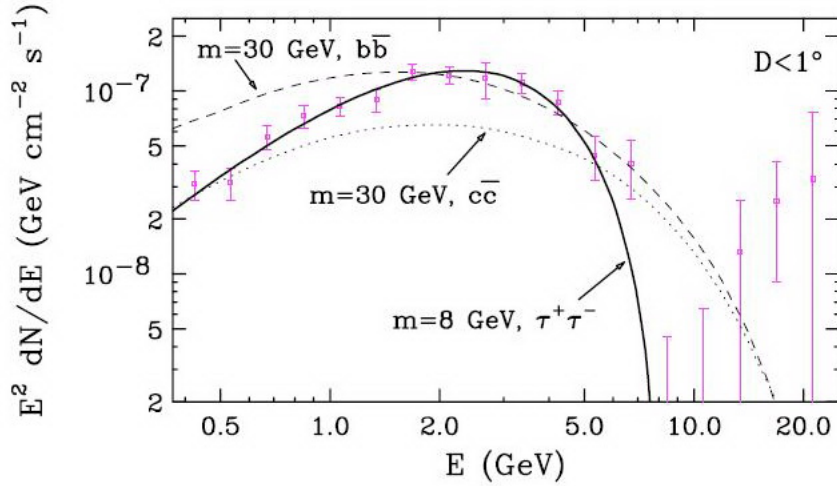


Figure 2.8: Gamma ray excess observed from  $1.25^\circ$  of the galactic center by the Fermi Gamma-ray Space Telescope. Curves predicted based on various WIMP masses are also plotted. Data is particularly well accounted for by a  $\sim 8\text{ GeV}$  dark matter annihilation (primarily to tau leptons). Picture taken from [25]

Compared with space based telescopes, ground based detection is less limited by detector areas and can probe higher energy gamma rays. Experiments of this type are all using Air Cerenkov Telescopes, detecting Cerenkov light emitted by particle showers initiated by high energy gamma rays when they pass through the atmosphere. In 2006, the H.E.S.S collaboration has reported a  $\text{TeV}$  energy gamma ray excess, which was probably produced by a  $\sim 10\text{ TeV}$  WIMP annihilation from the galactic center. However, this argument is barely convincing and can be better explained by other known cosmological sources [26].

## Neutrinos

Besides the Galactic Center, clumps of WIMPs may also aggregate inside the sun or earth. When WIMPs travel through these objects, they scatter once and get into

an orbit, which make them go again and again through the objects. So they have a chance to scatter multiple times and eventually settle close to the center of the Sun or Earth. As the local WIMPs density increases, annihilation becomes possible. However, because of the dense surrounding material, only neutrinos are able to escape and eventually be detected terrestrially, while other annihilation products will either absorbed or moderated on the way out.

With the competing annihilation and capture processes, an equilibrium would be present inside the core, which leads to an annihilating rate mainly driven by the WIMP-matter scattering cross section: spin dependent interaction is dominating for the hydrogen rich Sun, whereas spin independent interaction is prominent on the Earth. This feature naturally bridge from indirect detection to direct detection, allowing a feasible comparison between two approaches. The work done by Kamionkowski et al. [27] indicates that a neutrino telescope is definitely not promising in the spin independent regime, even compared with very small direct experiments. But it overwhelms all current spin dependent direct search experiments in the high WIMP mass range, though its exclusion curve doesn't extend to lower mass and it is more model-dependent than the direct method (Figure 2.9).

The currently running big neutrino telescope, such as the  $1\text{ km}^3$  scale IceCube, is expected to refine its result by extending its curve to lower mass in the coming years.

### 2.4.3 Direct Detection

The Earth is located in the Galactic halo, where dark matter is believed to be relatively dense. Taking a dark matter density of  $\sim 0.3 \text{ GeV}/c^2/\text{cm}^3$ , as deduced from the measurement of the rotation curve, one can estimate an average dark matter

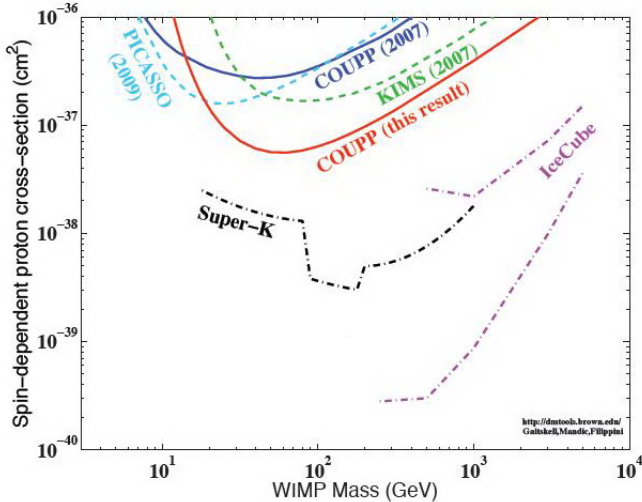


Figure 2.9: Upper limits on spin-dependent WIMP-proton cross sections. COUPP is currently the leading direct search experiment (red solid line), while PICASSO gives better result in low energy range (cyan dashed line). Indirect experiments including Super Kamiokande and IceCube are also plotted, presenting a greater sensitivity but in a rather limited mass range. Picture taken from [28]

flux in Earth's vicinity of:

$$\Phi = \frac{\rho_0 v_0}{M_\chi} \approx 7 \times 10^4 \text{ cm}^{-2} \text{ s}^{-1} \quad (2.8)$$

This relatively high abundance might make it possible to detect dark matter terrestrially and preferably through its interaction with baryons in the laboratory. The interaction is assumed to be in the weak scale, for the cosmology model predicts a weak scale cross section for WIMP annihilation into Standard Model particles. This gives rise to the fact that the WIMP-baryon scattering is an intrinsically rare event, even if the presence of WIMP dark matter is not that uncommon on the Earth. This could be better understood through a calculated interaction rate of WIMPs on a

terrestrial detector [29]:

$$R_0 = \frac{2}{\sqrt{\pi}} \frac{N_A}{A} \frac{\rho_\chi}{M_\chi} \sigma_0 v_0 \quad (2.9)$$

If one takes Avogadro constant  $N_A = 6.02 \times 10^{23}/mol$ , nuclear mass  $A = 73g/mol$  (if the target material is Ge, as adopted by several experiments), WIMP local density  $\rho_\chi = 0.3GeV/cm^3$ , WIMP mass  $M_\chi = 100GeV/c^2$ , WIMP-nucleon scattering cross section  $\sigma_0 = 10^{-36}cm^2$  (one picobarn, typical for weak scale interaction), incident WIMP velocity  $v_0 = 10^{-3}c$  (typical galactic velocity in the solar system), the expected interaction rate is about two events per month in a one-kilogram germanium target mass. This gives the first critical obstacle when carrying out a direct dark matter search experiments, as the counting rate from background radiation is in the Hertz range even if the detector is well shielded.

Another problem is the low interaction energy. When a WIMP particle with mass  $M_\chi = 100GeV/c^2$  interacts with a stationary target nucleus of mass  $m$ , through elastic scattering, as believed by most WIMP models, the averaged kinetic energy of the recoiling target is given by:

$$E_{recoil} = E_\chi \frac{2 \frac{m}{M_\chi}}{(1 + \frac{m}{M_\chi})^2} \quad (2.10)$$

Where  $E_\chi$  is the WIMP's incident kinetic energy. For a typical WIMP velocity of  $\sim 10^{-3}c$ , this gives  $E_\chi \approx 50keV$ . Thus a WIMP will render the target nuclei a  $E_{recoil}$  of the order of  $25keV$  when it hits a Ge detector. This is less than the nuclear binding energy, and only atomic electrons can be excited, which results in a very weak signal that only low-threshold detectors can detect. WIMP can also interact with electrons, but this is not used to track the scattering, because the resulting recoil energy is lower than  $1eV$ , a value beyond the reach of any major detecting technology. WIMP-nucleon interaction is thus the standard probe in any direct search efforts.

A WIMP can interact with a nucleon in two different ways: *spin – independent scattering* where the WIMP ‘sees’ the nuclei as a whole; *spin – dependent scattering* where it only couples with unpaired spins. Either category is promising in uncovering the dark matter enigma. But they require distinct technologies, and thus fueling corresponding experiments in different ways.

### Spin-independent scattering

In a spin-independent interaction, a WIMP views the target nuclei as a collection of undistinguishable nucleons. In the vanishing momentum transfer limit ( $q \approx 0$ ), the cross section is simply a superposition of contribution from all individual nucleons. As  $q$  rises, this no longer stands, due to destructive interference among some of the components, which leads to a reduced overall cross section. This reduction is quantified as a positive nuclear form factor  $F(q)$ , the value of which is always smaller than unity. After these consideration, a differential cross section can be expressed as

$$\frac{d\sigma_{SI}}{dq^2} = \frac{4}{\pi} \mu_{\chi N}^2 [Zf_p + (A - Z)f_n]^2 F^2(q) \quad (2.11)$$

Where  $\mu^{\chi N} = \frac{M_\chi M_N}{M_\chi + M_N}$  is the reduced mass;  $\frac{4}{\pi} \mu_{\chi N}^2$  is the kinematic factor; A and Z are the atomic mass and atomic number of the targeting nuclei;  $f_p$  and  $f_n$  are the coupling constants for proton and neutron respectively, though in most supersymmetry models they are rendered similar values, resulting in a simple quadratic relation between cross section and atomic number:  $\frac{d\sigma_{SI}}{dq^2} \propto A^2$ . So direct search experiments are all building their detectors with heavy nuclei like *Ge* or *Xe*, aimed at a large enhancement of the sensitivity.

## Spin-dependent scattering

The spin-dependent cross section, on the other hand, is dominated by unpaired spins within the entire nucleons. Since nucleon all try to cancel each others contribution, making the nuclei in a stable state by aligning their spins differently, only odd-neutron or odd-proton nuclei show non-vanishing spin and thus spin-dependent coupling with an incoming WIMP. Light nuclei is always preferred, because it can increase nuclear spin per unit mass. The cross section is given by [30]:

$$\frac{d\sigma_{SD}}{dq^2} = \frac{8G_F^2}{(2J+1)v^2} S(q) \quad (2.12)$$

Where  $J$  is the total nuclear spin.  $S(q)$  is equivalent to the nuclear form factor in the spin-independent interaction, but it is distinguished from  $F(q)$  by its dependance on the detailed spin distribution in a given nucleus.

Although many WIMP models predict a higher spin-dependent cross section than the spin-independent, the latter can be easily scaled up by implementing a heavy nucleon, whereas there is very limited choice of nucleus with large value of spin that can enhance the occurrence of the spin-dependent interaction. The spin-independent interaction is thus the dominating approach in the direct dark matter search experiments. CDMS, as the topic of this thesis, is a leading collaboration in this spin-independent effort.

## Backgrounds

Cosmic rays and terrestrial radioactive background place a major challenge to direct detection experiments, as mentioned in the previous paragraphs. Cosmic originated backgrounds can be effectively reduced by setting up experiments deep underground, while ambient backgrounds like natural radioactivity from lab rock remains a prob-

lem.

Electromagnetic radiation is the most frequent background among all types, with a Hertz level counting rate even if the detector is well shielded. However, through careful choice of detection technology, usually a combination of two distinct detecting channels (phonon, ionization, scintillation are the mostly used), the vast majority of electrons/photons can be excluded from the potential WIMP signals. Neutrons, on the other hand, are generally not distinguishable, and are prone to elastic scattering with nuclei, thus behaving similarly to a WIMP. Their influence can only be diminished by either developing an effective shielding strategy, usually with ultra pure water or polyethylene being the moderate material, or through a detailed Monte Carlo simulation to quantize the influence.

One always wants to perform a rare-event search experiment nearly free of background. If assuming the magnitude of the background is  $B$ , and the total WIMP search exposure is  $MT$ , where  $M$  is the total detector mass and  $T$  is the time length of the operation, then this condition is equivalent to  $B \ll 1$  event. Under this condition, all observed events are actual WIMP events. The experiment's sensitivity is proportional to  $MT$  as long as the underlying condition holds. As the total exposure increases, the background level is expected to grow proportionally:  $B \propto MT$ . When  $B > 1$  event, either systematic or statistical uncertainty will step in. If the statistical uncertainty is dominating, the experiment's sensitivity will still grow along an increasing total exposure but more slowly. Because the counting rate is following a Poisson distribution, the standard deviation ( $\sigma$ ) of the expected background level  $B$  is  $\sqrt{B}$ . The uncertainty in determining the background level of the observed events thus limits the sensitivity only grows  $\propto \sqrt{B} \propto \sqrt{MT}$ . The systematic uncertainties are coming from the not well understood part of the experiment, which is a flaw that would be magnified proportionally as the total exposure increases. Thereafter

if systematic uncertainties are the main concern, the sensitivity will stop improving despite of scaling up of total exposure.

Therefore it is worthless to build up larger detectors without a thorough and improving understanding of background limitation. An experiment with no knowledge of this limitation is equivalently having infinite systematic error. No serious study can be done under this condition.

## Detection

There are numerous experiments currently underway within the direct dark matter search community. They can be classified by several criteria, including interaction type (spin-dependent or spin-independent), operating temperature (cryogenic or non-cryogenic), target material (crystal or liquid), background rejection methodology (double channel detectors or just single channel detectors). Below I will briefly discuss a few notable experiments following the classifications stated above, giving a glimpse of their basic techniques.

*EDELWEISS* [31] is similar to the CDMS in taking temperature change in a cryogenic Ge detector as a measurement for total energy deposition, and using both ionization and phonon signals to exclude electromagnetic background radiations.

*CRESST* [32] is another prominent solid-state detectors user. Instead of measuring ionization signals, CRESST takes scintillation signals as the complementary measurement against background radiations. The detector is made up of a pure  $CaWO_4$  crystal. As a particle hits the detector, the phonon signal is collected by a TES thermometer adhered on the crystal, while scintillation light is emitted by excited atoms and absorbed and measured as another phonon signal by a nearby independent cryogenic light detector. The discrimination power comes from the so called quenching factor, a value inversely proportional to light yield: electrons/photons give the highest

light yield, while tungsten gives the least. An advantage of this method is that it gives a discrimination between neutron and WIMP signals (though not very obvious) [33]: neutron is mostly interacting with light nuclei, characterized by a quenching factor of  $\sim 7.4$ , whereas WIMP are prone to interact with tungsten, giving a quenching factor of  $\sim 40$ .

*XENON100* [34] is the most promising among the noble liquid detectors. It is using a 'dual phase'(liquid-gas) technology to produce two scintillation signals upon every incoming particle. The primary scintillation light is emitted in the liquid xenon, giving a full energy measurement. A second signal is produced in the gaseous xenon, as charge carriers drift to the gaseous volume under high voltage, ending up with scintillation light proportional to charges released in the interaction. Both light signals are measured by photomultiplier tubes (PMTs). By analyzing these two signals, electromagnetic radiation can be excluded. Xenon is an ideal target material, as its large atomic mass ( $A \sim 131$ ) greatly enhances spin-independent interaction cross section; its high boiling point ( $\sim 165K$  at 1 atm) facilitates a simpler cryogenic system; its liquid nature makes the sensitive volume easily scaled up by just building larger xenon containers, which is a property shared by all noble liquid experiments, in comparison with a solid state detector which is smaller but with a better energy resolution.

*DEAP* [35] uses a single phase liquid argon detector to produce a single scintillation signal upon particle arrival. Electromagnetic radiation is distinguished through pulse shape discrimination, for nuclear and electron recoils have very different pulse shapes.

*PICASSO* [36] is currently one of the most sensitive direct experiments searching for spin-dependent interaction. Phase-transition detectors are used in PICASSO. They are bubble chambers filled with superheated liquid  $C_4F_{10}$ , working in non-cryogenic environment, only sensitive to particles having  $dE/dx$  larger than a given

threshold. The threshold is closely related to the detector working temperature. Thus by changing the liquid temperature, specific background radiations can be avoided. However, bubble chambers can only tell if an incoming particle is below or above the threshold. In order to resolve the particle's energy, one has to combine data from several runs with different energy thresholds.

# Chapter 3

## Cryogenic Dark Matter Search

As stated in the first chapter, the detection of WIMPs can be challenging in many aspects. Due to rarity of WIMP interactions, experiments with larger exposure are necessary. This can be achieved by either building large mass detectors or extending operation period. However, this is only beneficial when there is a thorough understanding of the background radiation. The background radiation places an obstacle in this enterprise by greatly outnumbering the expected WIMP rate, which calls for the implementation of suppression or discrimination technology. Low energy detection is also required, due to the expected low energy transfer from the WIMP interaction.

CDMS responded to these challenges by developing cryogenic ionization detectors ensuring sensitivity to energy depositions as low as a few keV. Through simultaneous measurement of phonon and ionization signals, these detectors achieve a strong discrimination ability against the problematic electron/photon background.

The CDMSII detectors are based on cylindrical substrates, 7.62 *cm* in diameter, 1 *cm* thick made from either Ge or Si. Ge is an excellent target material due to its great enhancement of spin-independent WIMP-nucleon scattering cross section. The experiment is designed to be sensitive to spin-independent WIMP-nucleon inter-

actions, but isotopes including  $^{29}\text{Si}$  and  $^{73}\text{Ge}$ , with odd nucleons numbers, provide sensitivity to spin-dependent interaction as well.

The phonon and ionization signals are measured independently on the opposite side of the detector. The phonons are measured through a tungsten transition-edge sensors (TESs) which are grouped into four quadrants and also act as the ground reference for the charge collection; the charge side is made up of two concentric electrodes: a large inner electrode covers  $\sim 85\%$  of surface area, with a full charge collection capability; the outer electrode occupies the rest of the surface, measuring events happening close to the edge that suffer from a reduced charge collection (Figure 3.1).

With these advancement, CDMS is currently one of the leading WIMP search experiments.

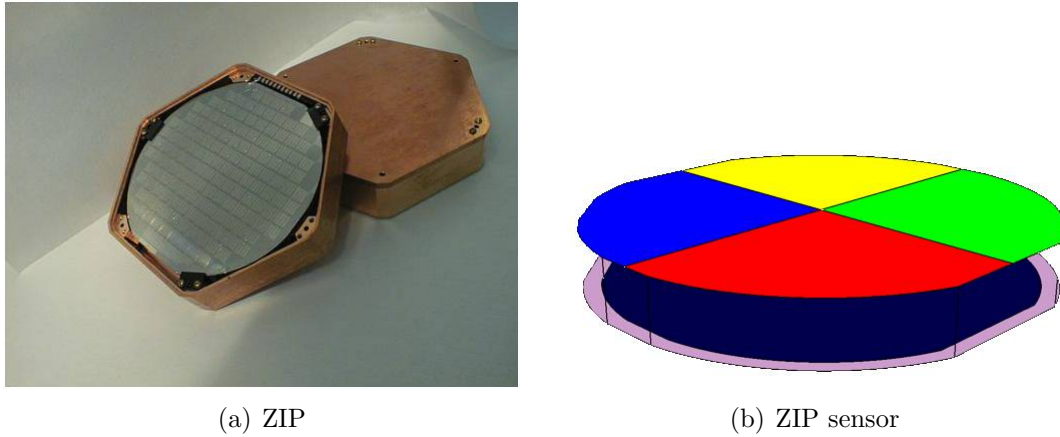


Figure 3.1: (a) CDMS detector. (b) Phonon and charge channels on the CDMS detector. On one side, the phonon sensors are grouped into four quadrants, shown in different colors; although not particularly clear, the two concentric electrodes are located on the reverse side.

### 3.1 Charge Signal

When a particle hits the detector, some of the deposited energy would be imparted to lattice vibration, or phonons. The rest would be consumed by liberating electron-hole pairs. If a sufficiently large electric field is applied across the detector, the generated charge carriers would drift apart instead of disappearing through electron-hole recombination. Charge carriers created in the semiconductors can produce image charges on either surface. The amount of image charges equals that of the charge carriers, while the fraction on each surface is affected by its distance from the moving charges. Thus the drifting charge carriers provide a current on the readout circuit, the time integral of which is an exact measurement of the charge generated from the initial interaction.

The charge signal in CDMS is expressed in units of “electron equivalent energy”, which is the energy of an electron recoil that would excite the same number of charge carriers. We call this the “ionization energy”. For electron recoils this is given by  $E_Q = N_Q \epsilon$ , where  $\epsilon$  is the energy required to excite one electron-hole pair on average. This energy is larger than the band gap energy ( $\sim 1\text{ eV}$ ), because some of the energy goes into phonons upon liberation of each electron. The value of  $\epsilon$  is  $3.0\text{ eV}$  for Ge and  $3.8\text{ eV}$  for Si. These values are roughly three times smaller than those for nuclear recoils, for a significant amount of energy is converted into lattice vibration in that condition.

The charge signals are collected by a readout circuit, the schematic drawing of which is shown in Figure 3.2.

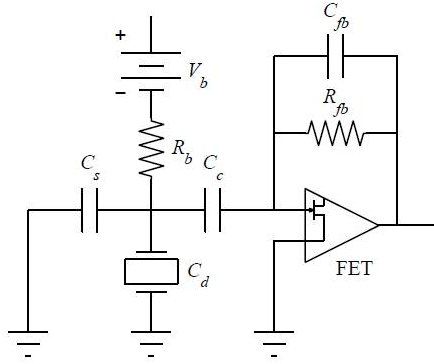


Figure 3.2: A schematic charge readout circuit. The detector is biased by  $V_b$  through a resistor  $R_b = 40 M\Omega$ . Values for other capacitors/resistors are: stray capacitances  $C_s \sim 100 pF$ , detector equivalent capacitance  $C_d \sim 50 pF$ , coupling capacitor  $C_c = 300 pF$ , amplifier feed back capacitor  $C_{fb} \sim 1 pF$ , amplifier feed back resistor  $R_{fb} = 40 M\Omega$ .

## 3.2 Phonon Signal

In addition to ionization signals, phonon signals are also measured in the detector in response to a particle interaction. Along with the liberation of charge carriers, the *primary phonons* are released in the vicinity of the interaction site, which is also the reason why it requires energy higher than the band-gap to create the charge carriers.

The drifting charge carriers can emit *Luke phonons* which are comparable to the Cerenkov emission as a charged particle moves with a velocity larger than the speed of light in the medium. As charges eventually end up near the detector surface, their energy is shed to the *recombination phonons*, the value of which equals to the sum of band-gap energies as slowed electrons de-excite.

$$E_{recombination} = N_Q \times E_g \quad (3.1)$$

Where  $E_g$  is the band-gap energy. Thus a combination of the *primary phonons* and the *recombination phonons* gives a full measurement of recoil energy. However, the

phonons are measured as one signal, a superposition of all different types, including the *Luke phonons*. The *Luke phonons* are therefore needed to be separated from the total contribution.

The *Luke phonons* take all the work the electric field does on the drifting charge carrier, thus having a characteristic energy of  $E_{Luke} = Q \times U = N_Q eU$ .  $N_Q$  is the number of charge carriers which can be re-written by use of the ionization energy  $E_Q$ :  $N_Q = E_Q/\epsilon$ , resulting in a correlation between the *Luke phonon* energy and the ionization energy:

$$E_{Luke} = \frac{E_Q eU}{\epsilon} \quad (3.2)$$

The choice of the operating voltage is a compromise between good charge separation which requires higher voltage and small *Luke phonons* which requires smaller voltage. Experimentally, we found that 3 V for Ge or 4, /V for Si is close to optimal.

### 3.2.1 TESs and SQUID

The tungsten transition-edge phonon sensors (TESs)[37] are implemented in CDMS to capture and measure phonons. They are thermometers operated in the transition from superconducting to normal state. Since the transition curve is very steep, a small fluctuation in temperature results in a relatively large change in the resistance. Thus the weak phonon signals created by the hypothetical WIMP interactions are capable of being detected by this sensitive equipment.

The TESs are in contact with an thin superconducting Al layer. Phonons with energy larger than the energy gap ( $\Delta Al$ ) can break the Cooper pairs in the superconducting Al and create the Bogoliubov quasiparticles. These quasiparticles either

recombine to Cooper pairs and re-emit phonons back to the crystal or diffuse into the nearby region, where the overlapping of the Al with tungsten creates a smaller energy gap. Quasiparticles arrive at this stage would lose some energy by emitting phonons or exciting new quasiparticles, which makes it not energetic enough to go back to the former stage and can only drift to the tungsten film, where the band gap vanishes, eventually contributing to the observed signal (Figure 3.3).

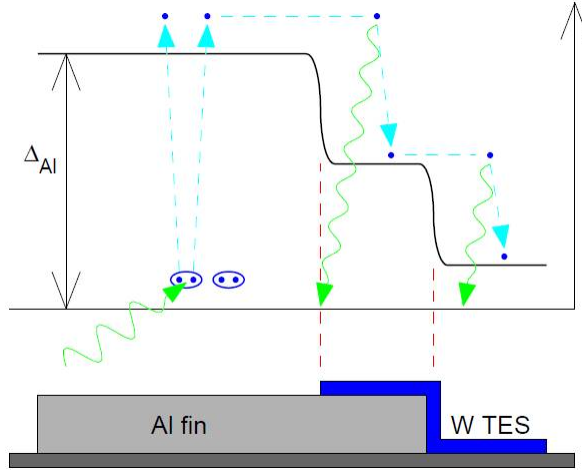


Figure 3.3: Quasiparticles are released from breaking up of Cooper pairs. They can only go to regions with lower energy gap. Since tungsten has the smallest gap, quasiparticles are eventually absorbed by the TES, contributing to the signals.

The Output from the TESs is too small to be digitized. So a SQUID amplifier is connected to each of them, the schematic drawing of which is shown in Figure 3.4.

### 3.3 Cold Hardware

The cryogenic environment is achieved and maintained by a dilution refrigerator. In order to avoid radioactivity embedded, detectors are placed in an "icebox" spatially

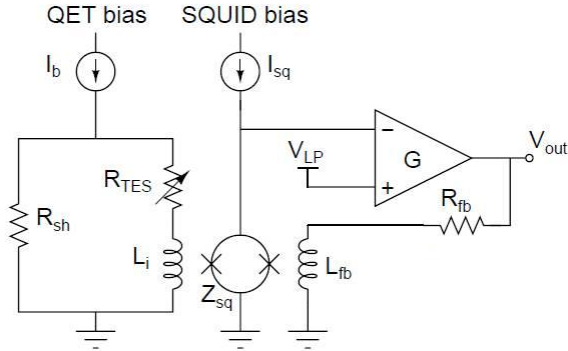


Figure 3.4: A schematic drawing of SQUID amplifier.

separated from the refrigerator and by a cold finger. The icebox is made up of six nested cans, attached to the room temperature,  $77\text{ K}$ ,  $4\text{ K}$ ,  $600\text{ mK}$ ,  $50\text{ mK}$ , and  $10\text{ mK}$  stages of the refrigerator.

Detectors are mounted inside the innermost can as groups of six in a stack. To allow multiple interaction between adjacent detectors, lids are only placed above the top detector and below the bottom detector.

Detector signals are read out via many stages. The first stage is through six side coaxes attached to the six detectors in each stack. Each coax contains part of the ionization readout circuit and is adjusted in position to reach the corresponding detector. These coaxes bring signals to the next stage, the “Tower”, which is a hexagonal copper stack supported by a carbon tube, housing wires and bridging from the  $10\text{ mK}$  to the  $4\text{ K}$  temperature stage. Through the Tower, the signals are sent to either the SQUID amplifier board or the FET board. The SQUID board receives phonon signals and is connected to the  $600\text{ mK}$  stage, while the FET board includes the rest low temperature part of the ionization readout circuit which is attached to the  $4\text{ K}$  stage. They are connected by a superconducting cable (“flyover cable”) and named as SQUET as a whole (Figure 3.5). After this stage, the signals are brought to room temperature by striplines (multilayered copper-kapton sandwiches with 50

individual traces each).

### Tower Assembly Cross Section

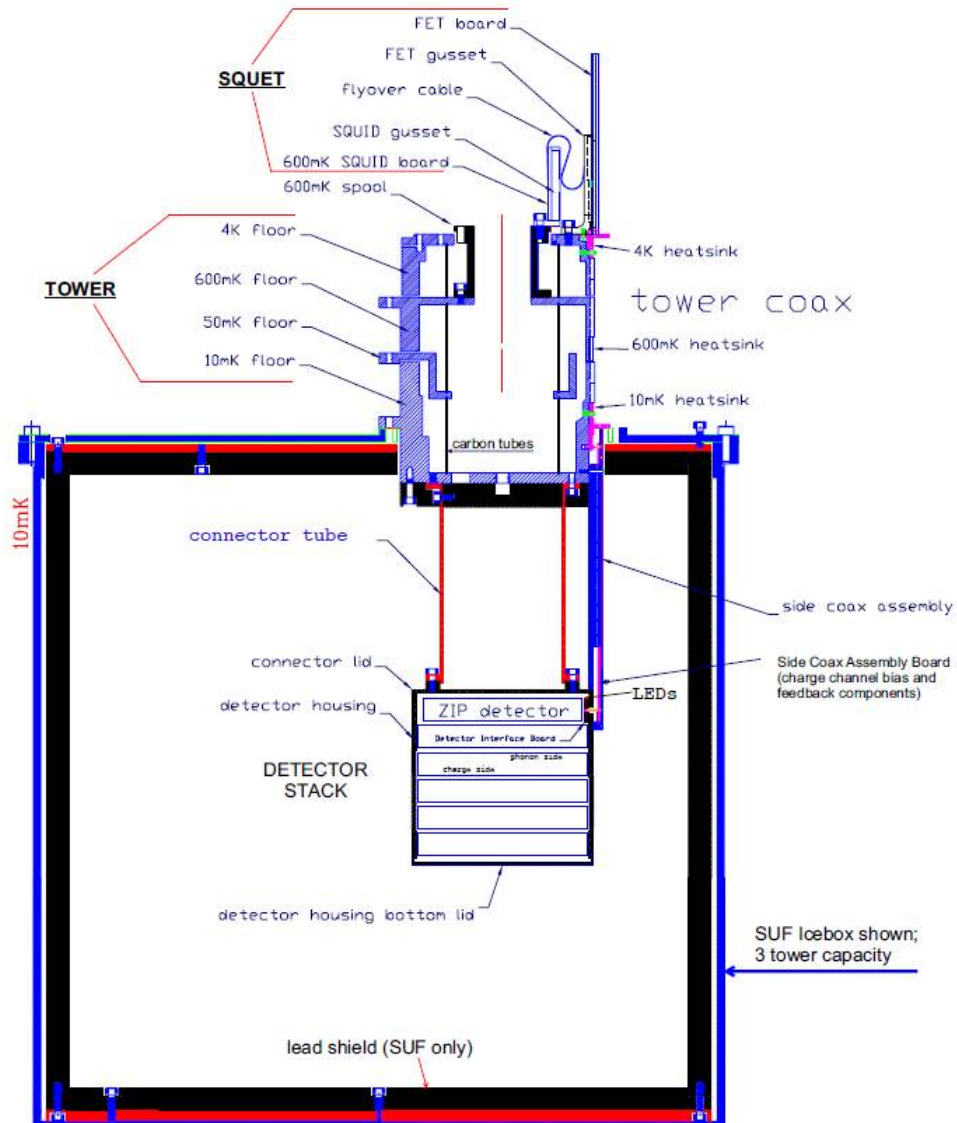


Figure 3.5: Cutaway view of icebox innermost can. Detectors, side coaxes, tower and SQUET are included. Picture is for previous Stanford Underground Facility (SUF), Soudan configuration only changed slightly.

## 3.4 Ionization yield

The charged particles and photons interact mainly with the electron system in the crystal, while the WIMPs and neutrons interact with nuclei, resulting in a significant reduction of the ionization energy. Therefore by defining the ionization yield as the ratio between the ionization energy and the primary phonon energy, the influence of problematic electron recoils can be eliminated.

$$y \equiv \frac{E_Q}{E_r} = \frac{E_Q}{E_p - \frac{eU}{\epsilon} E_Q} \quad (3.3)$$

The total Luke phonon contribution is subtracted from the total phonon energy to get true recoil energy  $E_r$ . This is explained in the previous section:  $E_Q$  is equal to the Luke phonon energy, which should be subtracted; otherwise the apparent energy would be larger than the actual energy deposition (section 3.2).

According to the definition of ionization energy (which is the energy of electron recoils that could produce the same amount of ionization), the ionization yield for electron recoil events should be unity. Nuclear recoil events have a smaller  $y$  value of approximately 1/3 (Figure 3.6).

## 3.5 Surface events

The surface events problem currently brings the most significant background to CDMS. It appears when an electron recoil occurs close to the electrode, which leads to a reduction in the measurement of the ionization energy, making it resemble a nuclear recoil. Its mechanism can be explained by two processes. The first one is that the produced charges are not fully separated and driven by the electric field, but rather diffuse backward and absorbed by the electrode. Since less charges drift, the

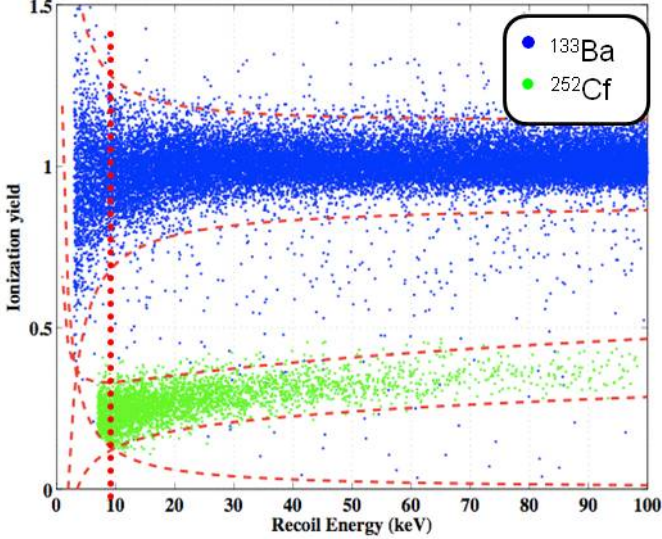


Figure 3.6: Ionization yield vs recoil energy. Data are from calibration runs, with dashed lines representing the  $2\sigma$  region for each type of events. Electron recoil events (blue dots) are from a  $^{133}\text{Ba}$  source, while nuclear recoil events (green dots) are from a  $^{252}\text{Cf}$  neutron source.

recorded ionization signal is consequently reduced. The second process is caused by the mirror charges created near the electrode. The electric force exerted by the mirror charges can cancel the nearby electric field if the charge is produced sufficiently close to the electrode, which makes the charge not drift and thus not contribute to the measurement of the ionization energy.

### 3.6 Current limit

Although no WIMP events have been observed, exclusion curves have been drawn to show upper limit for interaction cross sections. Many experiments have pushed the upper limit more and more down, leading to more parameter space above the curves being excluded. Recent data from the final exposure of CDMSII has shown the best result for spin-independent scattering of high mass WIMPs, with two events

found in the WIMP acceptance region [38]. Because the probability to find two or more background events in that region is 23% in that exposure, it can be concluded that we have not found a significant evidence for the WIMP interaction, but we can't reject these two events as signals either. The curve shown in Figure 3.7 is calculated based on standard halo assumptions: local dark halo density is  $0.3 \text{ GeV/cm}^3$  and halo velocity in the vicinity of Earth is around  $220 - 240 \text{ km/s}$  [39].

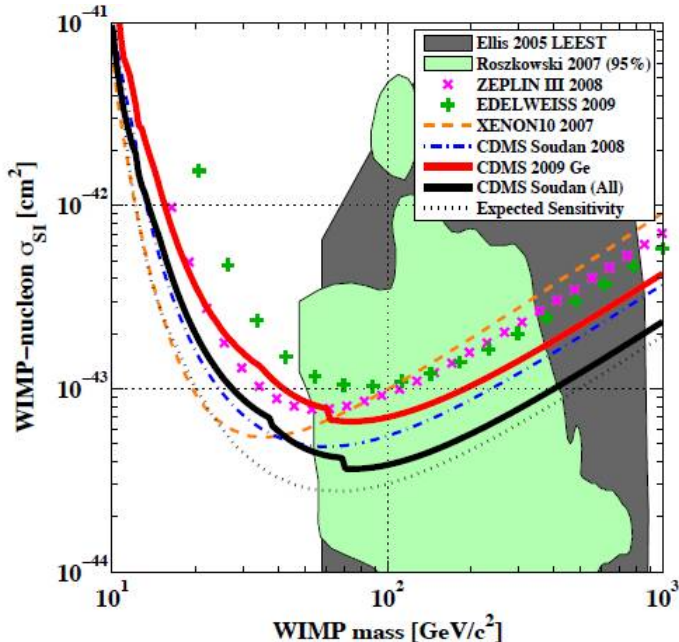


Figure 3.7: Exclusion curves from the final exposure of the CDMSII. The red solid line shows the upper limit set by the final exposure, with a minimum cross section of  $7.0 \times 10^{-44} \text{ cm}^2$  at a WIMP mass of  $70 \text{ GeV}/c^2$ . The black solid line combines all data taken at Soudan, showing a slightly better limit of  $3.8 \times 10^{-44} \text{ cm}^2$  at  $70 \text{ GeV}/c^2$ . The abrupt features in the curves are due to the observation of two events in the WIMP acceptance region. Parameter space above the curve is excluded at the 90% CL. Result from other experiments: ZEPLIN III, EDELWEISS, XENON10 are also shown on the plot. The shaded region is allowed parameter space calculated by certain supersymmetry models. Picture taken from [38]

## 3.7 SuperCDMS

SuperCDMS is the next generation of the CDMS experiment. It advances the current design as follows:

- Increase individual detector mass by increasing the thickness from  $1\text{ cm}$  to  $2.54\text{ cm}$ .
- Increase total target mass, going from  $\sim 5\text{ kg}$  in CDMSII to  $\sim 10\text{ kg}$  for SuperCDMS at Soudan and eventually  $100 - 200\text{ kg}$  proposed for SuperCDMS at SNOLAB.
- Reduce cosmic ray induced background by moving the experiment from Soudan to SNOLAB.
- Improve background discrimination by a new detector design, aimed at better exclusion of problematic electron/photon background radiation and specifically the surface events.

The first step towards this new experiment is by testing the new detector design in detector testing facilities. Due to high rate of background radiations, testing facilities on the Earth surface are not suitable to fully demonstrate discrimination power of these new detectors. Therefore a testing facility is to be built at SNOLAB to overcome this problem. To meet the strict requirement, this testing facility needs to be well shielded against natural radioactivity. The effectiveness of its shielding strategy is the main topic of this thesis.

# **Chapter 4**

## **Monte Carlo Method and GEANT4**

A thorough and detailed understanding of backgrounds is of utmost importance for a rare event search experiment. Without such a knowledge, no convincing explanations can be made upon observed data since the rare target signal is awash in some unknown backgrounds. As to this work, this prerequisite calls for answers from two successive questions: how are background particles generated and how do they interact with detectors? Subject to the complexity of the experimental setup and the wide variety of interactions involved, the Monte Carlo method is the best choice in responding to the above questions. In this chapter, I will firstly give a brief introduction to the Monte Carlo method and the specific toolkit that derives from this salient method. Next, the goal of implementing the Monte Carlo technique in this work will be discussed as well.

## 4.1 Monte Carlo Method

The Monte Carlo method dates back several hundred years when attempts of solving deterministic problems with statistical method initially came up. A famous example of this type is Buffon's needle experiment, in which he tried to determine the value of  $\pi$  via a random experiment [40]. The modern Monte Carlo method was initially formed in the middle of the last century when scientists at Los Alamos sought to solve the neutron diffusion problem with the newly invented digital computers. From the great efficiency and acceptable accuracy shown in that work, Monte Carlo was formally accepted as a feasible mathematical technique as a complement to the traditional deterministic methods.

The Monte Carlo method is a statistical technique, solving for problems by means of essentially random number generators. Its advantage over analytical or numerical methods is always illustrated through its use in calculating integrals. The basic argument goes as follows: Numerical methods are used to calculate an integral by sampling the integrated function. This method is only efficient when the mathematical dimension is low. As the dimension increases, the sample size grows exponentially, resulting in a rapid loss of efficiency. On the contrary, the Monte Carlo method treats this problem statistically, leading to a computing time independent of mathematical dimensions (more detailed explanations can be found in any standard Monte Carlo text books [40][41]). Therefore the Monte Carlo method is excellent for particle physics experiments for there are always numerous parameters involved.

## 4.2 The GEANT4 Particle Transport Code

GEANT4 (GEometry ANd Tracking) [42] is the Monte Carlo toolkit we used in this work. It is a particle transport code simulating propagation of elementary particles

in a user-defined experimental setup.

Before initiating a GEANT4 simulation, the user needs to define the geometry of the experimental setup using standard geometrical shapes predefined within the GEANT4 frame, where parameters such as materials and dimensions are to be specified. Next, elementary particles as well as associated physics processes that will show up in the simulation need to be selected. In the optimal situation, one wants to use a physics list that is fixed to the best available description of the real world. But this would cost unnecessary and usually significant amount of computing resources if some of the physics processes are not that important in the particular application. Therefore GEANT4 gives users the freedom to choose the relevant physics processes which are readily available from an extensive library in GEANT4.

The simulation is initiated by the generation of incident particles, the position and 3-momenta of which are determined at this point. During propagation, GEANT4 determines the upcoming physics process by sampling the total cross section, while deciding the final state after the interaction by sampling the differential cross section. The cross sections are either calculated based on certain theoretical models or directly picked up from look-up tables created from measured values. The wide availability and accuracy of this knowledge base make GEANT4 a powerful particle transport code.

Along processing the simulation, the user can collect information. The standard format used in this work to record information of events of interest is ASCII.

### 4.2.1 Terminology

Prior to further discussion, some terms need to be defined:

- Throw. The generation of an incident particle is known as a “throw”.

- Event. An “event” is the collection of all processes between two successive throws, including production and interactions of secondary particles.
- Hit. A “hit” is a single interaction; a “detector hit” is a hit in a sensitive volume (detector).
- Primary particle. It is the particle initially generated in one throw.

### 4.2.2 Validation

#### Accuracy of low energy neutron simulations

Since GEANT is initially designed for high energy physics, early versions of GEANT are not very accurate at low energy, especially in the regime of neutron transport. To tackle this problem, early GEANT simulation works [43][44] carried out by CDMS required an extra package of MICAP [45] to process neutrons when the energy is below  $20\text{ MeV}$ .

Simulations covered in this work were using GEANT4 9.3. Up to this version, GEANT4 has fixed the inaccuracy problem of low energy neutron transport even without the aid from MICAP. This is achieved by introducing the High Precision Neutron model, which is essentially a look-up table containing cross sections drawn from experiments. This is of great importance to this work, because neutron backgrounds simulated in this work are all below  $15\text{ MeV}$ .

To further validate this new model, a simulation experiment was performed several years ago, in which  $20\text{ MeV}$  neutrons were emitted onto a Gd target (Figure 4.1). An excellent agreement was found between the simulation result and the measured data (taken from ENDF)[46], giving a strong support to the underlying model.

### Gd154 ( $n,2n$ ) channel

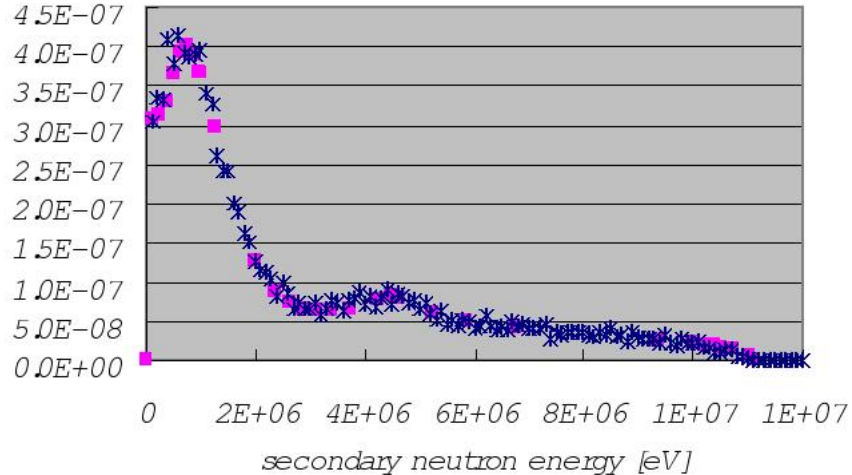


Figure 4.1: 20 MeV neutrons on Gd: High Precision Neutron model. Squares represent ENDF data; stars represent simulation result. The GEANT4 version is 8.1. The High Precision Neutron model is used in this simulation. An excellent agreement is found between the simulation results and measured data. Picture taken from [46]

## Physics models for gammas, electrons and neutrons

Table 4.1 contains the physics processes and the corresponding GEANT4 models adopted for gammas, electrons and neutrons in our simulations. To control the accuracy of the simulation, the “Range cuts” parameter needs to be specified. This parameter sets the lower limit for the free path between two sequential interactions. Empirically, we found  $200 \mu m$  was a good value for our application, which can give the satisfactory accuracy and not slow down the simulation by too much.

To validate the various physics models used in the simulation, we did several simple simulations to calculate certain parameters (attenuation length for gammas and mean free path for neutrons) which can be compared with measured values. To calculate the attenuation length for gammas, the geometry is chosen as a flat wall with appropriate thickness (usually three times of the attenuation length). Gammas

Table 4.1: Physics processes and models adopted for gammas, electrons and neutrons in the simulation. For neutrons, only the high precision models which are relevant to our applications ( $< 20 \text{ MeV}$ ) are shown.

Particle	Processes	Models
Gamma	Photoelectric effect	G4PhotoElectricEffect
	Compton scattering	G4ComptonScattering
	Gamma conversion	G4GammaConversion
Electron	Electromagnetic scattering	G4MultipleScattering
	Ionization	G4eIonisation
	Bremsstrahlung	G4eBremsstrahlung
Neutron	Elastic scattering	NeutronHPElastic
	Inelastic scattering	NeutronHPInelastic
	Neutron capture	NeutronHPCapture
	Nuclear fission	NeutronHPFission

are started from a point source off one side of the wall with direction perpendicular to the wall surface (Figure 4.2). By counting the number of undisturbed gammas that escape from the other side of the wall, one could calculate the attenuation length based on the simulation results:

$$I = I_0 2^{\frac{d}{d_{\frac{1}{2}}}} \quad (4.1)$$

where  $I$  and  $I_0$  are the number of gammas before and after passing through the flat wall (with direction undisturbed);  $d$  is the thickness of the wall;  $d_{\frac{1}{2}}$  is the attenuation length. Table 4.2 shows the calculated attenuation length of  $1 \text{ MeV}$  gamma in different materials, which are compared with the measured values. An excellent agreement was found from the comparison.

For neutrons, the mean free path was calculated. The geometry is a sphere with radius much longer than the mean free path. Neutrons are generated from the center with isotropic directions. The neutron is killed while its track length is recorded after its first interaction. By taking the average of all the track lengths, we could get the

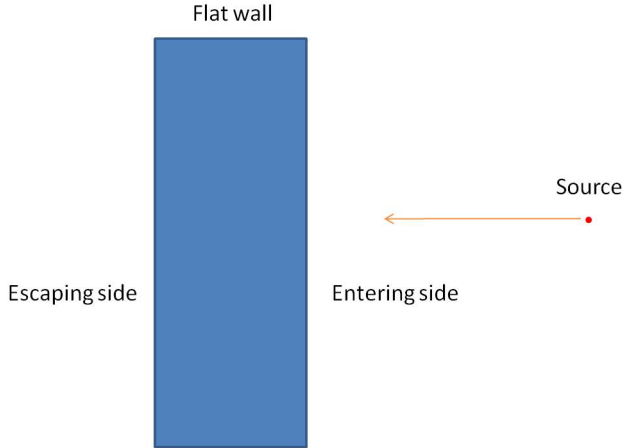


Figure 4.2: The geometry of the simulation to calculate the attenuation length for gammas.

Table 4.2: Attenuation length of 1 *MeV* gammas in different materials. Both simulation results and measured values [47] are shown.

Material	From Simulation	From Measurement
H <sub>2</sub> O	9.72 cm	10 cm
Pb	0.89 cm	0.88 cm
Al	4.16 cm	4.07 cm

mean free path between sequential interactions. Theoretically, the mean free path of neutrons can be calculated by [48]:

$$\lambda = 1 / \left( \sum_{i=1}^k \sigma_i \times \frac{\rho \times N_a \times n_i}{M} \right) \quad (4.2)$$

where  $\sigma_i$  is the interaction cross section of neutrons with the  $i$ th element in the material;  $\rho$  is the density;  $M$  is the atomic mass;  $n_i$  is the number of atoms for the  $i$ th element;  $N_a$  is the Avogadro constant;  $\lambda$  is the mean free path. Table 4.3 shows the theoretical mean free path calculated from this equation, together with the associate parameters and mean free path gained from the simulation. A good agreement was found between the theoretical and simulated results.

Table 4.3: Mean free path of  $1\text{ MeV}$  neutrons in different materials. Both theoretical and simulated results are shown. Neutron cross sections are taken from [49].

Material	Density	Cross section	Theoretical	Simulated
H <sub>2</sub> O	1g/cm <sup>3</sup>	4.24 b (H) 8.15 b (O)	1.79 cm	1.78 cm
Ge	5.32 g/cm <sup>3</sup>	4.4 b	5.15 cm	5.30 cm
CH <sub>2</sub> (Polyethylene)	0.92g/cm <sup>3</sup>	4.24 b (H) 2.57 b (C)	2.29 cm	2.20 cm

### 4.3 The Need for Monte Carlo Simulations

The need of Monte Carlo Simulations in this work can be characterized as follows:

- Preliminary simulation. A short and simplified simulation is run before the purchasing of shielding materials, to examine if the proposed amount is enough to achieve the target background level.
- Detailed simulation. A thorough simulation is carried out after the preliminary one, the result from which await comparison with experimental data to be collected in the future.
- Identifying dominant backgrounds. Various background mechanisms are tested in the simulation. After the exclusion of unimportant processes or background sources, dominant backgrounds can be revealed.

# Chapter 5

## Radioactive Backgrounds at SNOLAB

A new detector testing facility is to be built at SNOLAB, so is the future SuperCDMS. SuperCDMS is currently running at the Soudan underground lab ( $\sim 2000\text{ }mw.e.$ ), but the remaining cosmic muons at this depth will limit the sensitivity of the experiment. The much deeper SNOLAB ( $\sim 6000\text{ }mw.e.$ ) is a solution to the muon problem. This chapter will discuss to which extent the background can be reduced by this re-location, and what will be the major background contributors in SNOLAB as would be experienced by the new detector testing facility.

### 5.1 From Soudan to SNOLAB

SuperCDMS at Soudan uses a similar shield as CDMSII (Figure 5.1), aimed at reducing the external background radiations. The innermost layer of this shield is the copper material that makes up the detector tower and housing themselves as well as the thermal shields (icebox). This layer is a few cm thick on average, thin but enough

to mitigate the beta and alpha radiation. Outside this layer, lead and polyethylene layers are presented to stop the gamma and neutron backgrounds respectively. To distinguish the cosmogenic neutrons produced by the cosmic muons inside the experimental setup, an active muon veto is built as the outermost layer. This veto is made up of 40 scintillating plastic panels. If a nuclear recoil is found being coincident with a muon signal, it is identified as a muon induced neutron background signal.

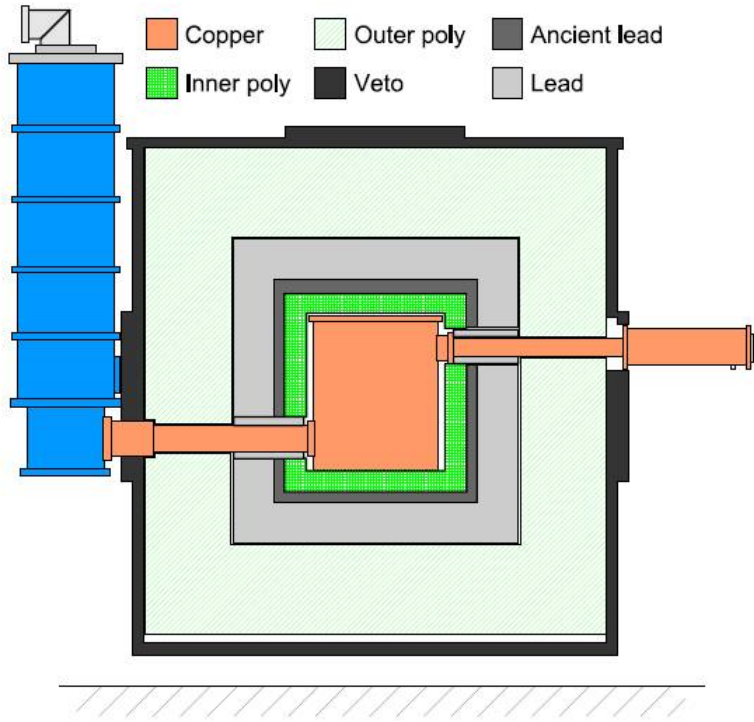


Figure 5.1: SuperCDMS/CDMSII shield. Inner polyethylene, ancient lead, outer lead, outer polyethylene and muon veto are built outside the copper made inner cans and stems. The left stem is a cold finger connecting to the different thermal stages of the refrigerator; the right stem is serving for the detector readout wirings (Figure from [50]).

In the surrounding rock, natural radioactivity is the dominant background neutron producer in the Soudan underground lab, while the muon induced neutron flux is

largely suppressed due to the depth of this site (Figure 5.2 and Table 5.1). Neutrons from natural radioactivity have energies below  $10\text{ MeV}$ . They can be satisfactorily shielded with sufficient amount of hydrogenous shielding material, such as polyethylene in our experiment.

Muons presented at Soudan depth can produce neutrons with a wide range of energy, expanding from thermal to the GeV scale. The very high energy neutrons behave differently from the low energy neutrons ( $< 10\text{ MeV}$ ) and can go through the polyethylene shield without much interaction. These neutrons may create secondary neutrons in material inside the shield, which may deposit energies within the range of interest ( $10\text{ keV} - 100\text{ keV}$ ) in the detectors, resulting in nuclear recoils undistinguishable from WIMP signals. Therefore although muon induced neutrons are outweighed by neutrons originated from natural radioactivity by more than two orders of magnitude, they are still one of the two major neutron background contributors as observed in the detector. The other contributor at Soudan SuperCDMS is natural radioactivity embedded in materials inside the polyethylene shield.

Table 5.1: Neutron rates coming from rock due to natural radioactivity and cosmic ray muons in the Soudan underground lab (in the units of  $10^{-8}\text{ g}^{-1}\text{s}^{-1}$ ). Table taken from [51].

Origin	Neutron rate
Natural Radioactivity	$2.4 \pm 0.2$
Cosmic Muon	$7.29 \times 10^{-3}$

At SNOLAB, the muon induced neutron flux is reduced by more than two orders of magnitude compared to Soudan (Figure 5.3 and Table 5.2). As a result, it is losing domination as a main background neutron source to the radionuclides hidden in materials inside the polyethylene shield, if assuming the contamination level of ma-

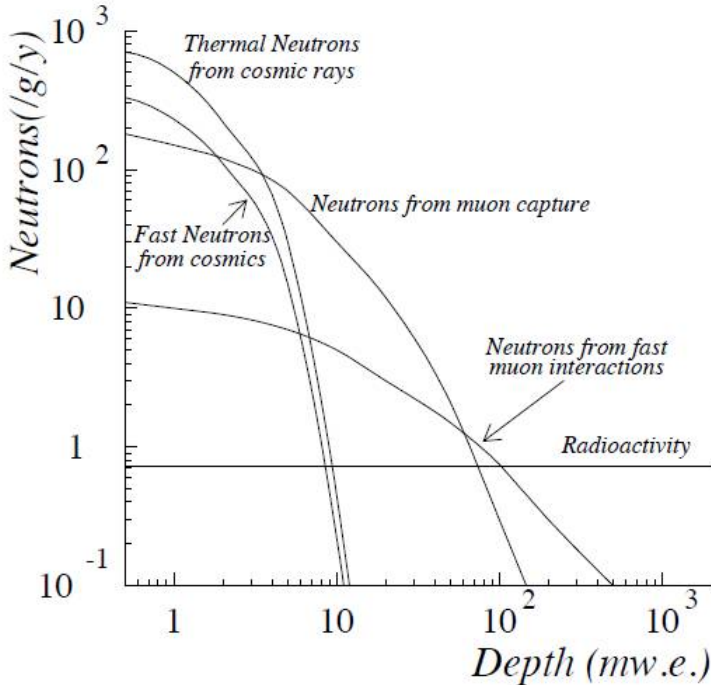


Figure 5.2: Underground neutron production rate as function of depth (in meters of water equivalent). As seen from the plot, the hadronic component from cosmic rays is suppressed below 10 m.w.e.; muon induced neutrons begin to be outnumbered by neutrons from natural radioactivity at  $\sim 100$  m.w.e. (plot from [52]).

terials used to build up the experiment remains relatively unchanged, which is highly possible. This change can be seen from Table 5.3.

Table 5.2: The muon-induced neutron flux for Soudan and SNOLAB (in units of  $10^{-9} \text{ cm}^{-2} \text{s}^{-1}$ ); the comparison is done with three threshold energies (from [54]).

Site	$> 1.0 \text{ MeV}$	$> 10 \text{ MeV}$	$> 100 \text{ MeV}$
Soudan	5.84	4.73	1.073
SNOLAB	0.020	0.018	0.005

As to the shield proposed for the SuperCDMS testing facility at SNOLAB, the muon induced neutrons are therefore not important and will not be discussed in the rest of this thesis.

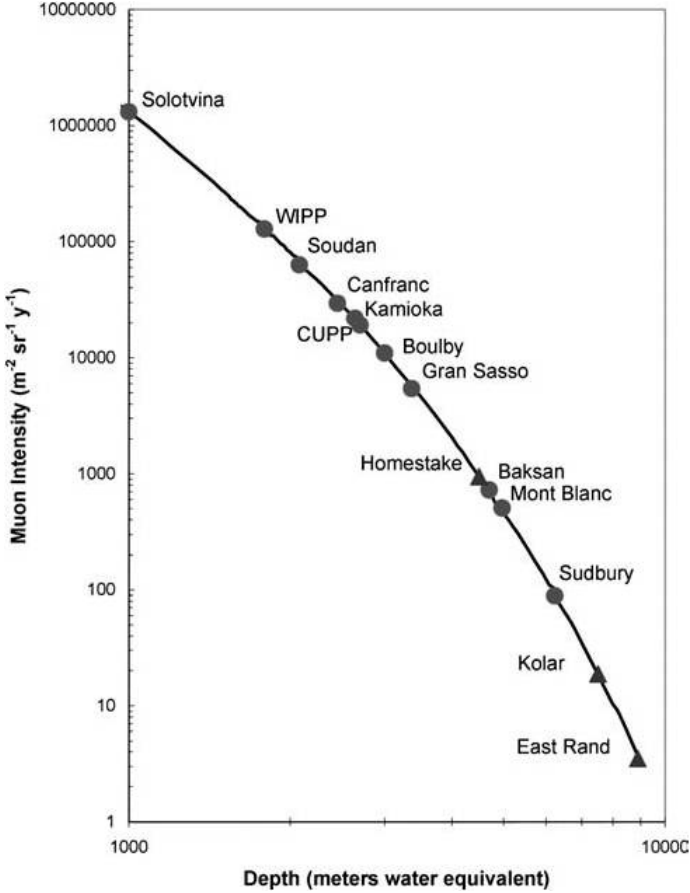


Figure 5.3: Muon flux diminishes as depth increases. Depth is measured in meter water equivalent (mwe). Circles represent currently operating laboratories, while triangles show closed ones (Homestake is scheduled to reopen for experiments in 2011). The current and future sites of SuperCDMS, Soudan and SNOLAB (Sudbury) are both shown in the plot. Picture taken from [53]

## 5.2 Backgrounds at SNOLAB

SNOLAB is located two kilometers underground inside the Vale Ltd. Creighton Mine near Sudbury Ontario Canada. It is an operational nickel mine actively mining at depth below the SNOLAB region. SNOLAB is excavated from norite rock. Its elemental composition is shown in Table 5.4. Primordial radionuclides including  $1.11 \text{ ppm } ^{238}\text{U} \& ^{235}\text{U}$ ,  $5.56 \text{ ppm } ^{232}\text{Th}$  and  $1.35 \text{ ppm } ^{40}\text{K}$ , are present in the laboratory walls. They are extremely long living isotopes (half life  $\gtrsim 10^9 \text{ years}$ ), acting as the

Table 5.3: Expected neutron background events that cannot be distinguished from WIMPs in the nuclear recoil energy range of  $10\text{ keV}$  to  $40\text{ keV}$  from CDMSII at Soudan, SuperCDMS at Soudan, and future SuperCDMS at SNOLAB. The event rate is given in units of events/kg-day, and number of events ( $\{\text{No.}\}$ ). Table taken from [55] (The expected target masses for SuperCDMS have changed since these data were published, but the rates are still representative.)

Background events	Not rejected events	
	Rate	$\{\text{No.}\}$
<i>CDMS II at Soudan <math>4.5\text{ kg} \times 485\text{ days}</math></i>		
Neutrons:		
radio-nuclides	2.0E-5	{0.01}
muon-induced	1.5E-4	{0.09}
<i>SuperCDMS at Soudan <math>7.5\text{ kg} \times 550\text{ days}</math></i>		
Neutrons:		
radio-nuclides	2.0E-5	{0.03}
muon-induced	1.5E-4	{0.20}
<i>SuperCDMS at SNOLAB <math>25\text{ kg} \times 1100\text{ days}</math></i>		
Neutrons:		
radio-nuclides	1.5E-5	{0.13}
muon-induced	4.5E-7	{0.004}

main source of background radioactivity at SNOLAB.

Uranium and thorium decay into sequences of daughter nuclides, which are radioactive themselves and will decay into their own daughter nuclide. The same process occurs to each daughter nuclide until a stable lead isotope is reached. The whole process is known as thorium or uranium decay chain, corresponding to the series of decay processes initiated by thorium or uranium decays respectively (Figure 5.4 and Figure 5.5).

Gammas, betas, alphas and neutrons are emitted in the above processes. Only gamma and neutron particles are considered in this work, for betas and alphas from external sources get easily stopped in the shield.

Table 5.4: Norite rock composition

Composition	
Element	% (weight)
H	0.15
C	0.04
O	45.82
Na	2.22
Mg	3.28
Al	8.92
Si	26.1
P	0.12
S	0.2
K	1.15
Ca	5.2
Mn	0.13
Fe	6.19
Ti	0.5

Assuming when the primordial isotope just begins to decay there are no daughter nuclides, as a result of the accumulation of the daughter nuclides, their decay rates will increase. This will conversely slow down and eventually stop the accumulation. If this happens to every nuclide in the decay chain, the entire decay chain enters a balanced state, which is known as the secular equilibrium.

It is safe to assume equilibrium is reached in the norite rock bulk volume, which then gives rise to a nearly constant radioactive source. But in case of rock surface or near surface situation, Radon, the daughter product of radium in both decay chains, can migrate from the rock surface to the air by diffusion or via recoil from emitting  $\alpha$  particle, breaking the equilibrium.

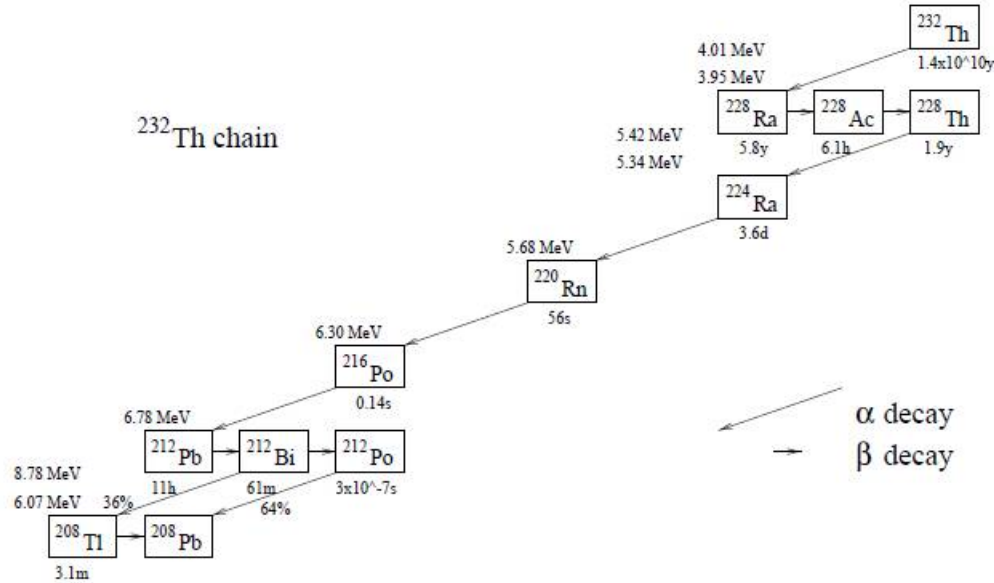


Figure 5.4:  $^{232}\text{Th}$  chain (Figure from [56]).

### 5.2.1 Gamma Backgrounds

Gamma flux from natural radioactivity in the rock is very intense in SNOLAB due to the large amount of rock present. The main sources are the U and Th decay chains and  $^{40}\text{K}$ .

#### Uranium and Thorium

Gammas are a byproduct of  $\alpha$  or  $\beta$  decays occurring in the decay chains. The induced gamma rays have a wide range of energies. The high energy ones including 2.615 MeV gammas emitted after the  $\alpha$  decay of  $^{212}\text{Bi}$  into  $^{208}\text{Tl}$  and the 2.204 MeV and 2.447 MeV gammas emitted after the  $\beta$  decay of  $^{214}\text{Pb}$  into  $^{214}\text{Bi}$  are of particular importance, because they can travel significantly longer distance than the low energy gammas in various materials. Therefore the shield must be properly designed to reduce the chance they can hit the detectors.

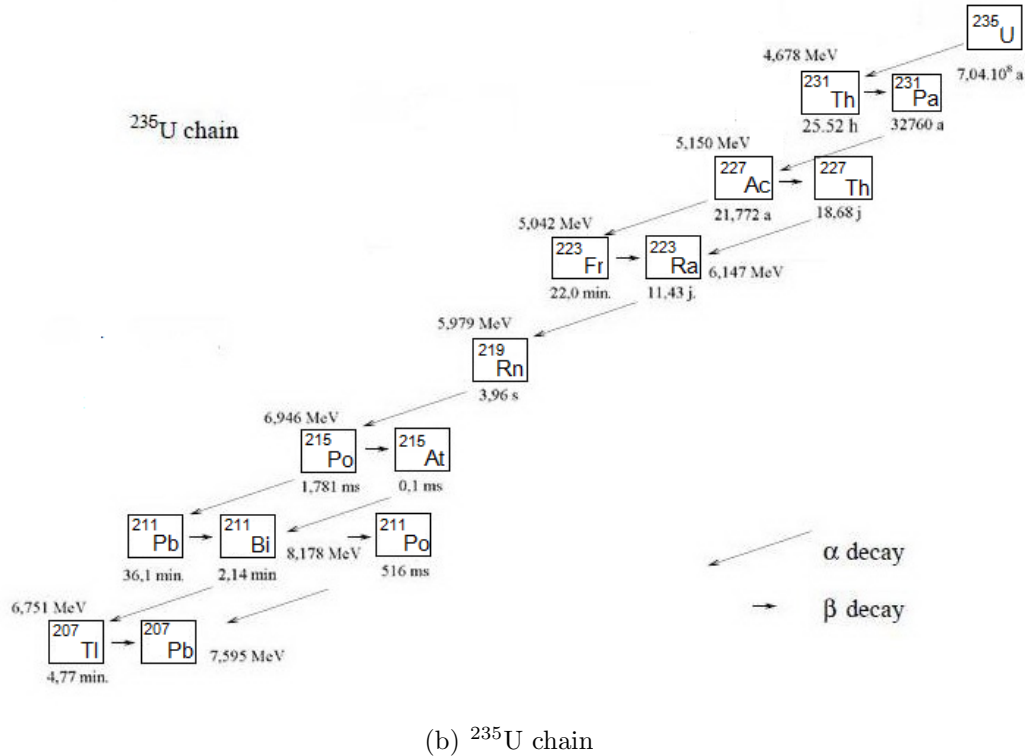
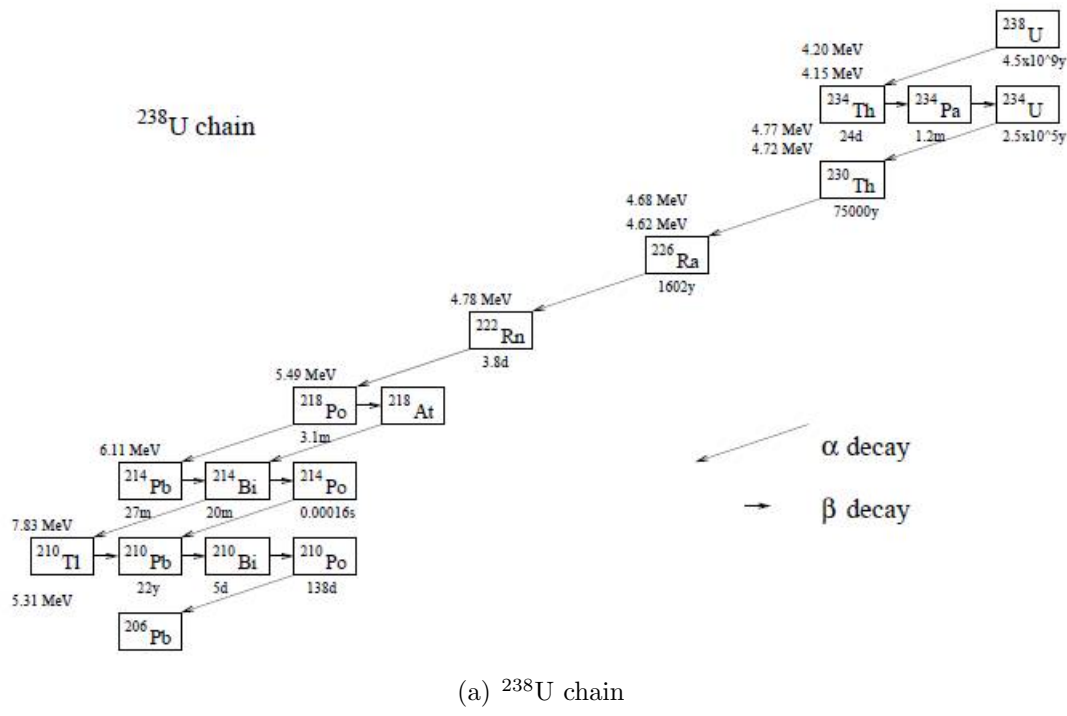


Figure 5.5: (a) $^{238}\text{U}$  decay chain (Figure from [56]). (b) $^{235}\text{U}$  decay chain.

## Potassium

$^{40}\text{K}$  is another main background gamma emitter in SNOLAB. It has a much less complicated decay process compared to the uranium or thorium decay chains: With 89.3% probability, it beta-decays into  $^{40}\text{Ca}$ ; in the remaining 10.7% of the cases, it decays to  $^{40}\text{Ar}$  via electron-capture, with the emission of a  $1460.8\text{ keV}$  gamma.

## Radon and Others

Background gamma radiation can be emitted from places other than the lab wall rock. Since the shield proposed for the SuperCDMS SNOLAB testing facility is water, the purity of the water is of great concern. Thorium, uranium and potassium levels may be reduced via proper purification techniques, but radon absorbed from the atmosphere during filling and operation poses a potential danger. Since radon is the intermediate decay product in the uranium decay chain (also occurs in the thorium decay chain, but the half life of radon from this chain is only a few seconds and it has only short lived daughter products and is therefore not important), it also goes through a series of decay processes as part of the uranium decay chain. Among its daughter products  $^{214}\text{Bi}$  and  $^{214}\text{Pb}$  are the most important gamma emitters. Others are either only producing low energy gammas or have a low branching ratio of gamma emission.

### 5.2.2 Neutron Backgrounds

Neutrons from natural radioactivity in the SNOLAB lab wall rock are mostly coming from  $(\alpha, n)$  interaction ( $\sim 90\%$ ). The remaining 10% are from spontaneous fission of  $^{238}\text{U}$ . The spontaneous fission spectrum is described by an empirical formula, while knowledge of  $(\alpha, n)$  interactions demands more complicated computer aided calcula-

tion.

### Spontaneous Fission

Spontaneous fission only occurs to very heavy isotopes. Due to its very small probability, in the context of uranium and thorium decay chains only fissions from  $^{235}\text{U}$ ,  $^{238}\text{U}$  and  $^{232}\text{Th}$  are worthy considering. From Table 5.5 [53], the branching ratio of spontaneous fission has the highest value in  $^{238}\text{U}$ , with four orders of magnitude higher than other isotopes. But even for  $^{238}\text{U}$  spontaneous fission is less probable to occur compared with the main  $(\alpha, n)$  interaction channels available from the uranium and thorium decay chains in the SNOLAB norite rock [57]. The neutron spectrum of spontaneous fission from  $^{238}\text{U}$  can be described by:

$$\frac{dN}{dE_n} = E_n^{\frac{1}{2}} e^{\frac{-E_n}{1.29}} \quad (5.1)$$

where  $E_n$  is the neutron energy in units of MeV [58].

Table 5.5: Branching ratios (BR) for spontaneous fission of  $^{235}\text{U}$ ,  $^{238}\text{U}$  and  $^{232}\text{Th}$ .

Isotope	BR
$^{238}\text{U}$	$5.45 \times 10^{-7}$
$^{235}\text{U}$	$7.0 \times 10^{-11}$
$^{232}\text{Th}$	$< 1.8 \times 10^{-11}$

### $(\alpha, n)$ interaction

$\alpha$  particles produced by  $\alpha$  emitters in the thorium or uranium decay chains may be absorbed by certain constituent elements in the norite rock. The induced compound nucleus may then decay into either an excited or a stable daughter nucleus through the emission of a neutron (Figure 5.6). Important  $\alpha$  emitters involved in this process

include  $^{212}\text{Bi}$  ( $6.05\text{ MeV}$  and  $6.09\text{ MeV } \alpha$ ),  $^{220}\text{Rn}$  ( $6.288\text{ MeV } \alpha$ ),  $^{224}\text{Ra}$  ( $5.685\text{ MeV}$  and  $5.449\text{ MeV } \alpha$ ),  $^{216}\text{Po}$  ( $6.8\text{ MeV } \alpha$ ),  $^{212}\text{Po}$  ( $8.8\text{ MeV } \alpha$ ) from the thorium decay chain, and  $^{218}\text{Po}$  ( $6.0\text{ MeV } \alpha$ ),  $^{214}\text{Po}$  ( $7.7\text{ MeV } \alpha$ ),  $^{210}\text{Po}$  ( $5.3\text{ MeV } \alpha$ ) from the uranium decay chain.  $\alpha$ s with an energy below  $5\text{ MeV}$  generally have much lower ( $\alpha,n$ ) interaction cross sections and are less often considered.

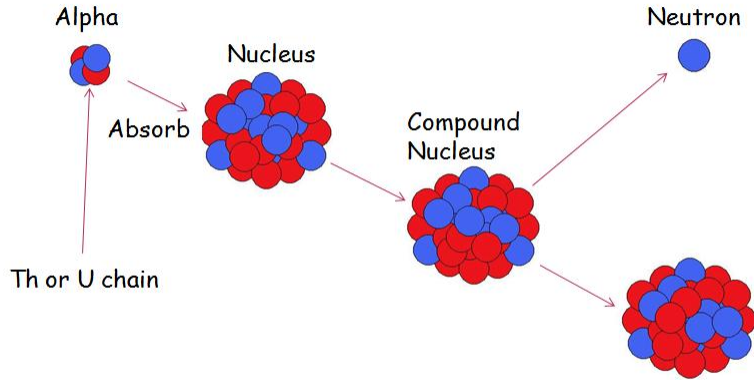


Figure 5.6: Scheme of  $\alpha$ -n interaction

Nuclides with low abundance ( $^{27}\text{Al}$ ,  $^{23}\text{Na}$ ,  $^{18}\text{O}$ ,  $^{25}\text{Mg}$ ,  $^{26}\text{Mg}$ ,  $^{29}\text{Si}$  and  $^{30}\text{Si}$ ) contribute most to the ( $\alpha,n$ ) production, since the  $\alpha$  particles from the two decay chains are not energetic enough to kick out neutrons from the more abundant isotopes in the norite rock:  $^{16}\text{O}$ ,  $^{28}\text{Si}$  and  $^{40}\text{Ca}$ .

There are two computer codes have been used in this study to calculate the  $\alpha$ -n interaction. One is a simplified code by P. Skensved, and the revised version by B. Cai; the other is SOURCES [59], a commercial code designed by Los Alamos National Laboratory to calculate the ( $\alpha,n$ ) interaction. The simplified code has been used for the preliminary work, while the much more precise SOURCES result was used in the consequential detailed study. Details about implication of these codes will be covered

in next chapter.

**Simplified code (Original)** The simplified code written by P. Skensved is based on work done by Heaton et al. [57][60][61] on  $(\alpha,n)$  yields from light isotopes. Two simplifying assumptions are made in this calculation:

- All alphas in the U and Th decay chains are assumed to have an energy of  $8.8 \text{ MeV}$ , the highest energy of any  $\alpha$  from both decay chains.
- Daughter nuclei after the  $(\alpha,n)$  reaction are all in ground state.

These two assumptions result in a much harder neutron spectrum. But the total neutron rate is only biased by a little bit (because except for the low energy  $\alpha$ s ( $< 5 \text{ MeV}$ ) which have significantly small  $(\alpha,n)$  interaction cross sections, all the other  $\alpha$ s with an energy below  $8.8 \text{ MeV}$  have similar cross sections. And also because the low energy  $\alpha$ s are less often produced from both decay chains, they have relatively small influence upon the final neutron yield.) The neutron rate calculated from this code is  $4.79 n/y/g$ , which is compatible with the measurement. Figure 5.7 shows the neutron spectrum from this calculation (spontaneous fission is also added in this spectrum; the spectra shown in the rest of this chapter are all combined spectra from both  $(\alpha,n)$  interactions and spontaneous fission by default unless specifically noted).

**Simplified code (Revised)** The simplified code was later modified by B. Cai, and P. Skensved. This new version takes the entire collection of  $\alpha$  particles from the decay chains into account, which makes the produced neutron spectrum softer. But it additionally assumes the  $\alpha$  absorption cross section is a constant independent of the  $\alpha$  energy. This is a good approximation for high energy  $\alpha$ s ( $> 5 \text{ MeV}$ ), but not for

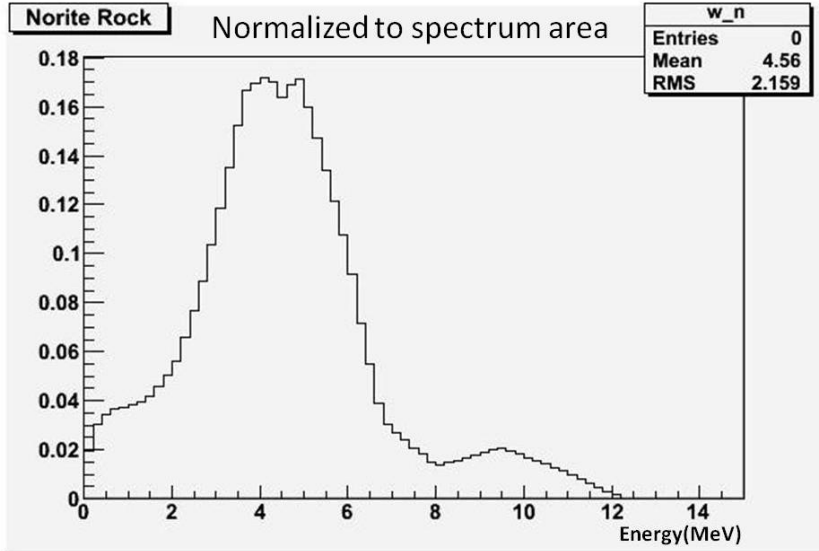


Figure 5.7: Primary neutron spectrum calculated from the simplified code by P. Skensved. Spontaneous fission is included in this spectrum.

low energy ones. However, because low energy  $\alpha$  particles are rare, this assumption doesn't have a big effect. It also keeps the assumption that daughter nuclei are all in the ground state, which results in a neutron spectrum still harder than the real one. The neutron rate from this revised code is  $4.75 n/y/g$ , which is almost the same as the previous version. But the energy spectrum (Figure 5.8) is much softer than before.

**SOURCES (first result)** SOURCES is a more precise approach in characterizing the  $(\alpha,n)$  interactions, for it avoids the entire assumptions made by the simplified code in the calculation. This code was implemented for us by M. Tarka (University of Zurich). However, in the first result, the reported neutron rate was twice as higher as that from the previous two methods, which was suspicious. After some investigation, we found and identified a problem with the SOURCES code. Table 5.6 shows a detailed comparison of neutron yields between SOURCES and the simplified code for

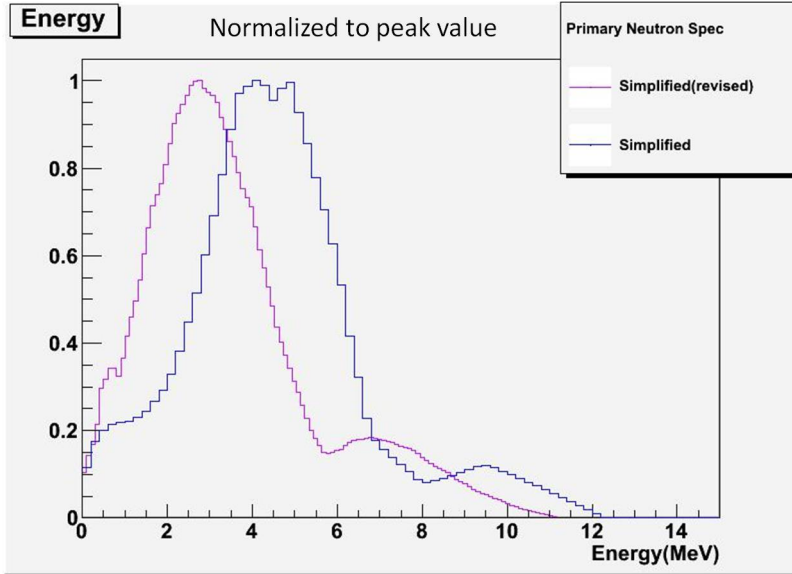


Figure 5.8: Primary neutron spectrum calculated from the revised simplified code (violet; Skensved and Cai). The spectrum calculated from original code is superimposed (blue).

all the  $\alpha$ s from the Th chain.

The first column in Table 5.6 shows the  $\alpha$  emitters in the thorium decay chain. The second contains the  $\alpha$  energies. As targets, only Al and Na, which contribute the most to the total neutron flux, are shown. The odd finding from this comparison is that the neutron rate of  $^{220}\text{Rn}$  from SOURCES is about 10 times higher than that from the simplified code, while for the other emitters, the rates are of the same order of magnitude (highlighted in the table). This is not expected because all the  $\alpha$ s have similar energy and also similar ( $\alpha, n$ ) interaction cross sections (except for the last row because the simplified code cannot treat the low energy  $\alpha$ s properly). A very strange spike was observed in the SOURCES neutron spectrum (Figure 5.9) which also implies a potential problem there.

**SOURCES (corrected result)** After a thorough investigation that revealed a malfunction of the SOURCES code for very specific  $\alpha$  energies, minimal changes in

Table 5.6: Comparison of neutron yields between SOURCES and the simplified code. All main  $\alpha$  emitters in the thorium decay chain are considered. Under each element, the first column contains neutron yields ( $10^{-7} n/\alpha$ ) for the  $\alpha$  emitters on this target element from SOURCES; the second column contains the same thing but from the simplified code; the last column contains the ratio between these two yields (SOURCES over Simplified).

Isotope	E	$^{27}\text{Al}$			$^{23}\text{Na}$		
		SOURCES	Simplified	Ratio	SOURCES	Simplified	Ratio
$^{212}\text{Bi}$	$6.05\text{ MeV}$	0.562	0.452	1.24	0.371	0.345	1.07
	$6.09\text{ MeV}$						
$^{212}\text{Po}$	$8.784\text{ MeV}$	15.69	8.865	1.77	8.068	5.503	1.47
$^{216}\text{Po}$	$6.778\text{ MeV}$	3.426	3.206	1.07	2.167	2.126	1.02
$^{220}\text{Rn}$	$6.2883\text{ MeV}$	21.29	1.801	11.8	13.57	1.275	10.6
$^{220}\text{Rn}^*$	$6.2880\text{ MeV}$	2.129	1.801	1.18	1.357	1.275	1.06
$^{224}\text{Ra}$	$5.685\text{ MeV}$	0.86	0.781	1.1	0.639	0.61	1.05
	$5.449\text{ MeV}$						
$^{228}\text{Th}$	$5.34\text{ MeV}$	0.519	0.488	1.06	0.442	0.412	1.07
	$5.423\text{ MeV}$						
$^{232}\text{Th}$	$3.947\text{ MeV}$	0.012	0.045	0.27	0.007	0.014	0.53
	$4.012\text{ MeV}$						

the initial  $\alpha$  energy (on the order of  $10^{-4}$ ) have been conducted to remove these problems. Due to this adjustment, the  $(\alpha, n)$  yield for the  $^{220}\text{Rn}$   $\alpha$  drops by a factor of 10 (which is shown in Table 5.6 as  $^{220}\text{Rn}^*$  to differentiate this change from the original one) and the overall rate is reduced by roughly a factor of two, which makes it compatible with result from the simplified code. The original SOURCES code doesn't exhibit this problem. There might be something wrong with its implementation in our application.

After this revision, the strange spike disappears (Figure 5.10). Comparing this modified spectrum with the above two spectra from the simplified code, the one from SOURCES is much softer (Figure 5.11). The neutron rate from SOURCES

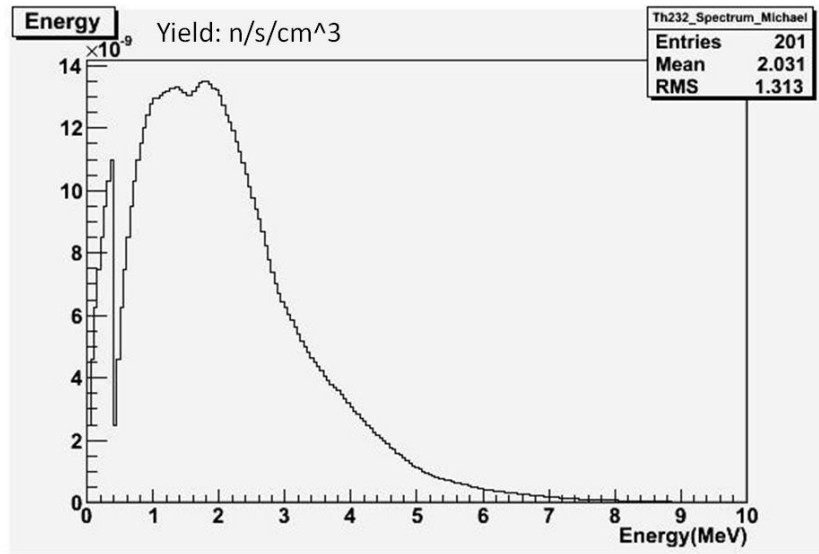


Figure 5.9: Thorium  $\alpha$  induced neutron spectrum. A strange spike is observed in the low energy end.

is  $5.76 /y/g$ , about 30% higher than that from other two approaches ( $4.79 /y/g$ ,  $4.75 /y/g$ ).

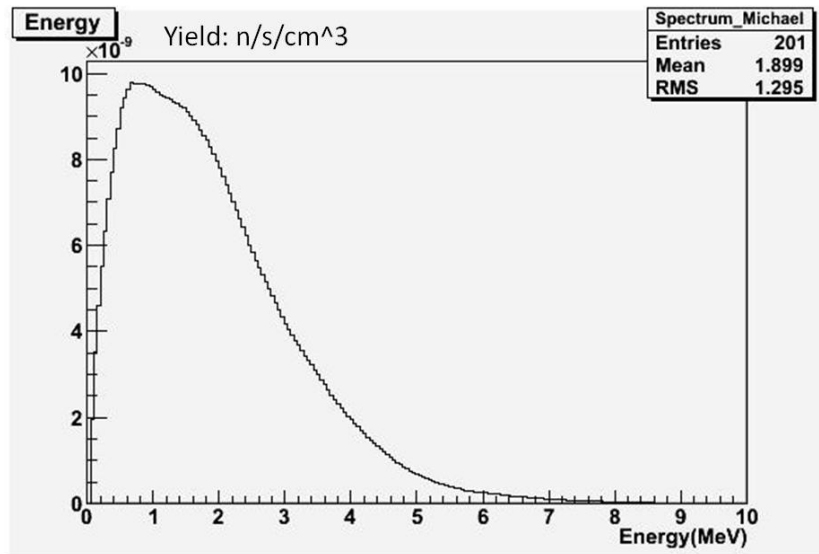


Figure 5.10: Neutron spectrum (including spontaneous fission). The strange spike is removed after the correction.

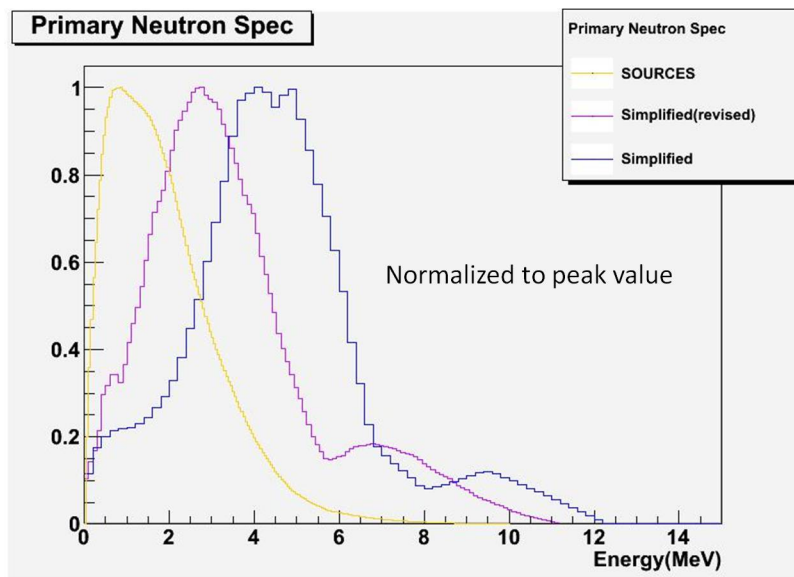


Figure 5.11: Comparison of three neutron spectra. Orange is from SOURCES; violet is from the revised simplified code; blue is from the original simplified code. The spectrum from SOURCES is much softer.

# Chapter 6

## GEANT4 Simulation for the SuperCDMS Testing Facility at SNOLAB

As mentioned in the previous chapters, the SuperCDMS detector testing facility or STF is to be built at SNOLAB. The motivation is to evaluate the new detector design in an environment less affected by background. This facility will be located in the ladder laboratory next to the place reserved for the future SuperCDMS experimental setup (Figure 6.1). In order to test detector performance with certain accuracy, background radiation needs to be mitigated to an acceptable level. Since the neutron background of most concern present at this depth is dominated by low energy neutrons ( $< 10\text{ MeV}$ ), a water tank surrounding the testing facility is believed to be capable of reducing backgrounds satisfactorily. The water tank is initially proposed to be 12 *feet* high and 12 *feet* in diameter. A preliminary GEANT4 simulation is carried out to test this proposal. The cryostat is hanging inside the water tank without appropriate shield from the top. Therefore lids made from either polyethylene or lead may be

needed (Figure 6.2). However, due to the presence of the dilution refrigerator above the detectors, which may block a certain fraction of the environmental radiations, the thickness or even the necessity of those lids is unknown till a through study is done. A much more detailed GEANT4 simulation is then done to seek answer to this question.

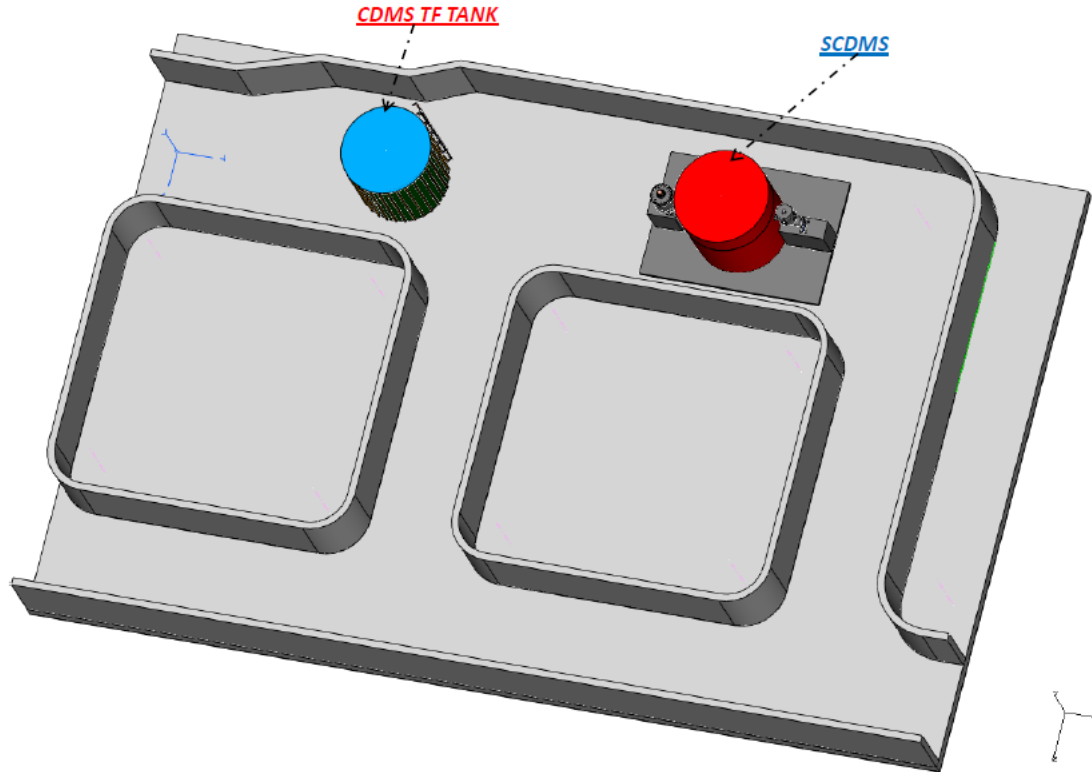


Figure 6.1: A simple layout of the space allocated for CDMS in the ladder laboratory at SNOLAB. Both STF and the future SuperCDMS setup are shown. The plot is drawn by E. Chi [62].

## 6.1 Preliminary Simulation

In the preliminary work, the effectiveness of the proposed water shield is checked for both gamma and neutron radiation. Natural radioactivity in the rock and radioactive

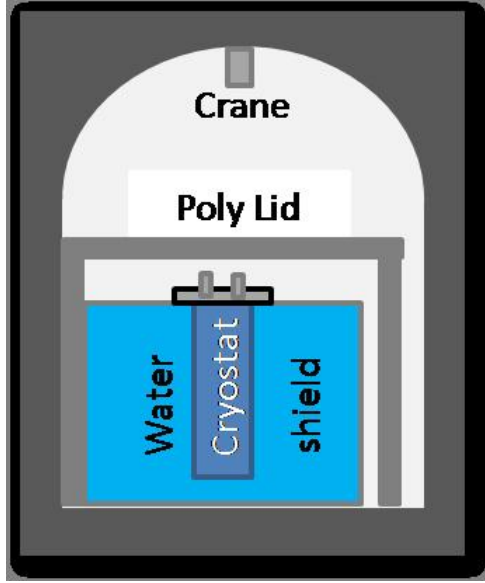


Figure 6.2: A sketch of cutaway view of STF. The dilution refrigerator or cryostat which contains the detectors is hanging inside the water shield. The PE and Pb lids are installed on the top to compensate for the absence of the water shield on that direction.

contamination (radon,  $^{60}\text{Co}$ ) in the water tank are considered in the simulation. The goal rate is of the order of 1Hz for gammas and 1/day for neutrons.

In any simulations, a proper geometry is the first step towards a truthful reflection of the real experiment. However, in our preliminary study due to the need for a quick answer, the accuracy of the geometry is largely compromised. Each constituent of the setup is simplified to be either a cylinder or certain combination of several cylinders. The whole geometry is concentric about the z axis. The PE and Pb lids are not included in the simulation, which should put the final result to the conservative side.

Four sets of simulations with different radioactive sources and configurations were run in the preliminary study.

### 6.1.1 Gamma from the laboratory wall

**Geometry** Figure 6.3 shows the geometry when the gamma source is located in the laboratory wall. The gamma is  $2.615\text{ MeV}$  in energy, which is the highest energy gamma from both uranium and thorium decay chains (see section 5.2.1 for detail discussion). Higher energy gammas are also presented at SNOLAB mainly produced by neutron capture process, but the intensity is extremely low and thus will not cause a problem in our application [56]. The gamma source is a cylindrical surface source attached to the laboratory wall cylinder, which is shown as green region in Figure 6.3. The simplified geometry neglects all material above the detector. Further, the thickness of the water shield would not influence the rate of those gammas from the ceiling, therefore those gammas are omitted in this preliminary study.

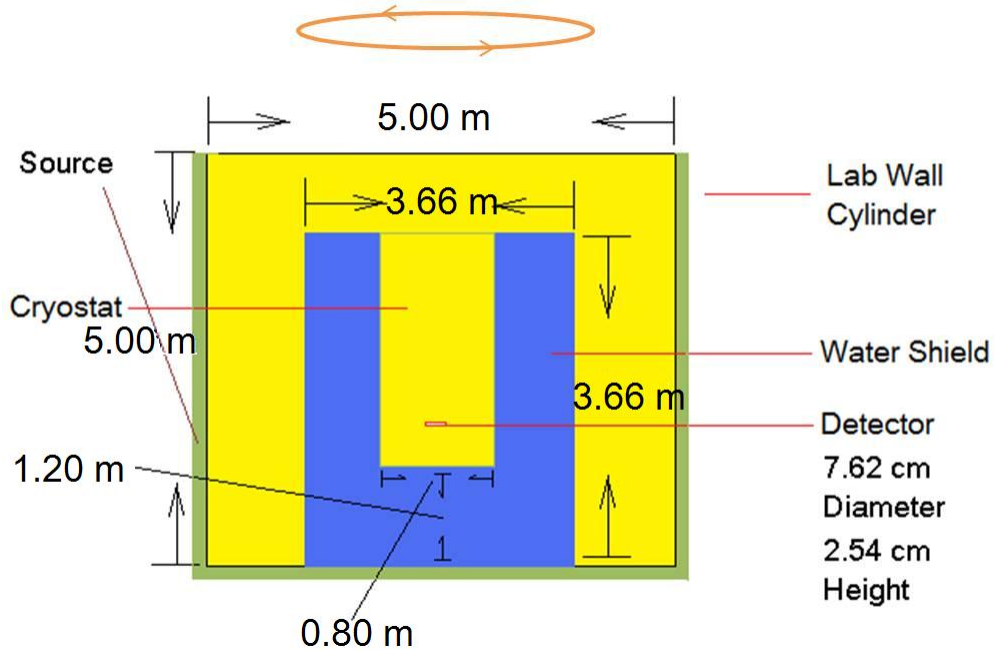


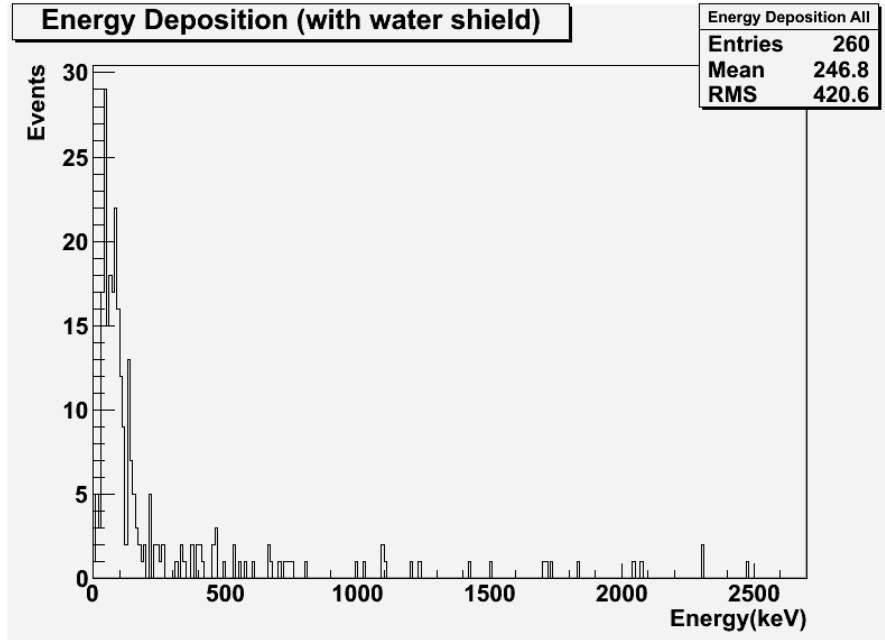
Figure 6.3: Geometry for the preliminary simulation of gammas from the laboratory wall. The yellow volume is air, the blue is the water shield. Any details inside the cryostat are omitted. The green represents the starting place of the incidental gammas.

**Simulation with water** To compare the simulation results with the real measurement, an estimate of gamma yield from current geometry is needed. Given the thorium concentration in the laboratory wall being  $5.56 \text{ ppm}$ , and  $2.87 \text{ g/cm}^3$  as the density of the rock, the production rate is found to be roughly  $\sim 10^{11} / \text{year}/\text{m}^3$ . Then taking an estimated skin depth of  $10 \text{ cm}$  for  $2.615 \text{ MeV}$  gammas in the norite rock (a simulation to calculate the skin depth was done later in the detailed study, which gave a similar result.) and  $\sim 100 \text{ m}^2$  as the surface area in the current geometry, we found the gamma yield from the current geometry is  $\sim 10^{12} / \text{year}$ . Therefore, the 600 million gammas thrown initially in the simulation are equivalent to *320 minutes* of measurement time, and the 260 depositions convert to a detector rate of  $\sim 0.8 / \text{minute}$  (Figure 6.4).

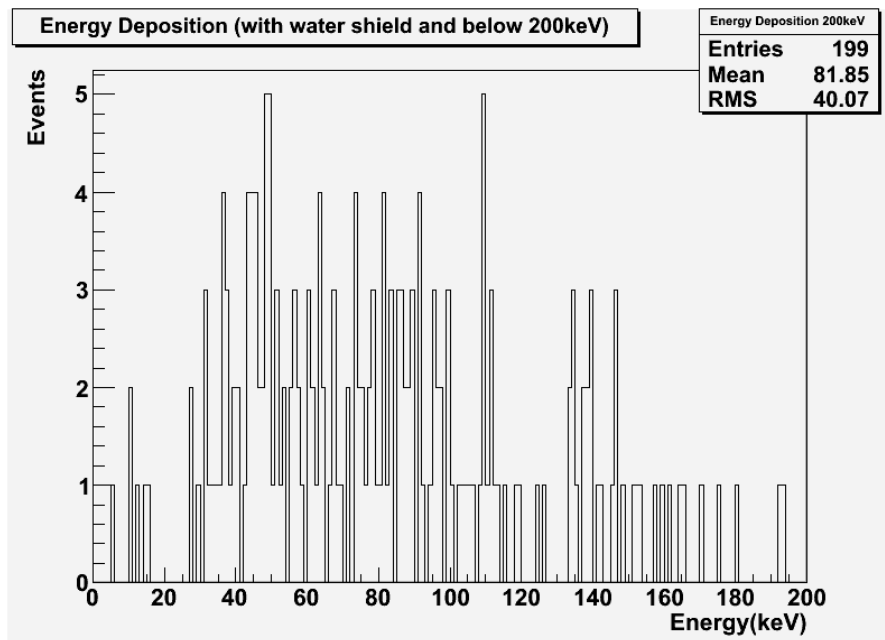
**Simulation without water** To examine to which extent the shield can reduce the gamma background, another simulation was done without the water shield, which also served as a validation. Figure 6.5 shows the 619 depositions in the detector, which leads to an equivalent detector rate of about 1 per 3 seconds, roughly 24 times larger than the one with the water shield. With the evident presence of the full energy peak, the code is proved functioning in good condition.

### 6.1.2 Neutrons from the laboratory wall

**Geometry** The geometry is slightly changed in case of neutrons. Figure 6.6 is the configuration for the preliminary neutron simulation. Due to the diffusive behavior of neutrons, a  $0.5 \text{ m}$  thick wall is included in the geometry. The neutrons are generated homogeneously within the wall. The energy spectrum is taken from the work by our colleague P. Skensved (Figure 5.7), which has been explained in section 5.2.2. The  $0.5 \text{ m}$  thick laboratory wall may not properly approximate the real situation where



(a) Total deposition



(b) Cut off at 200keV

Figure 6.4: Energy deposition from  $2.6 \text{ MeV}$  gammas from the laboratory wall (preliminary simulation). (a) 260 events deposited energy in the detector. (b) The zoomed plot. 199 events were found below  $200 \text{ keV}$ .

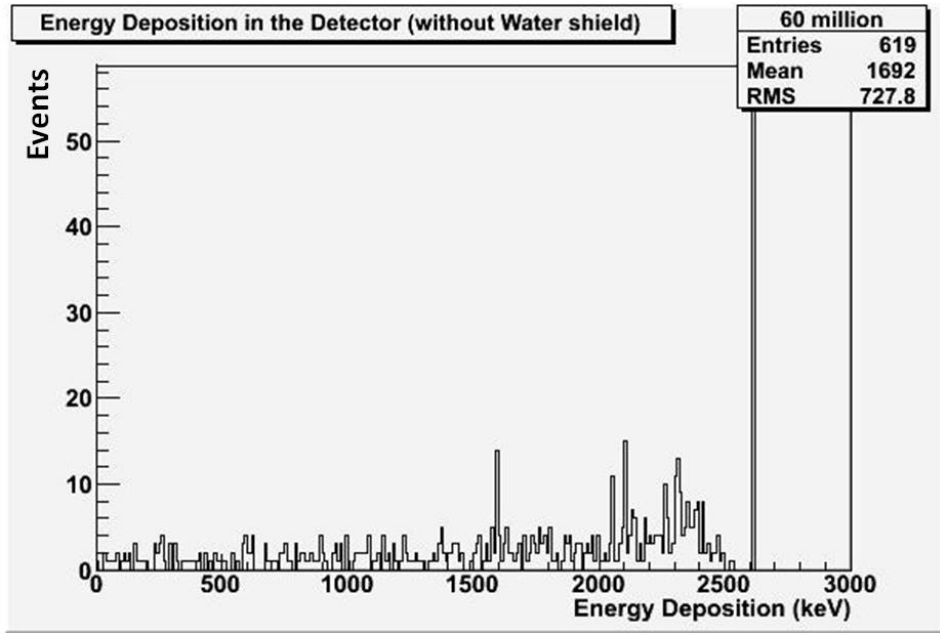


Figure 6.5: Energy deposition from the laboratory wall gammas (preliminary simulation with the water shield removed). 619 events out of 60 million initial throws deposited energy in the detector.

much more rock is presented, therefore a reflection method is used to compensate for the amount of rock not present in the geometry: Upon the arrival of a neutron on the outer boundary of the rock volume, it is immediately reversed in direction. In this manner the reflected neutrons can effectively represent neutrons coming from outside the current rock volume, from which the current volume is equivalently expanded. However, this method costs extra computing time, which may be an unnecessary expense if the method is not that useful. Therefore a validation check was done prior to the main simulation, providing an insight into the effectiveness of this method.

**Effectiveness of the reflection method** From analyzing the simulation data, we found that if a neutron transported towards the boundary and got reflected there, it had a probability to return to the boundary through random scatters and be reflected

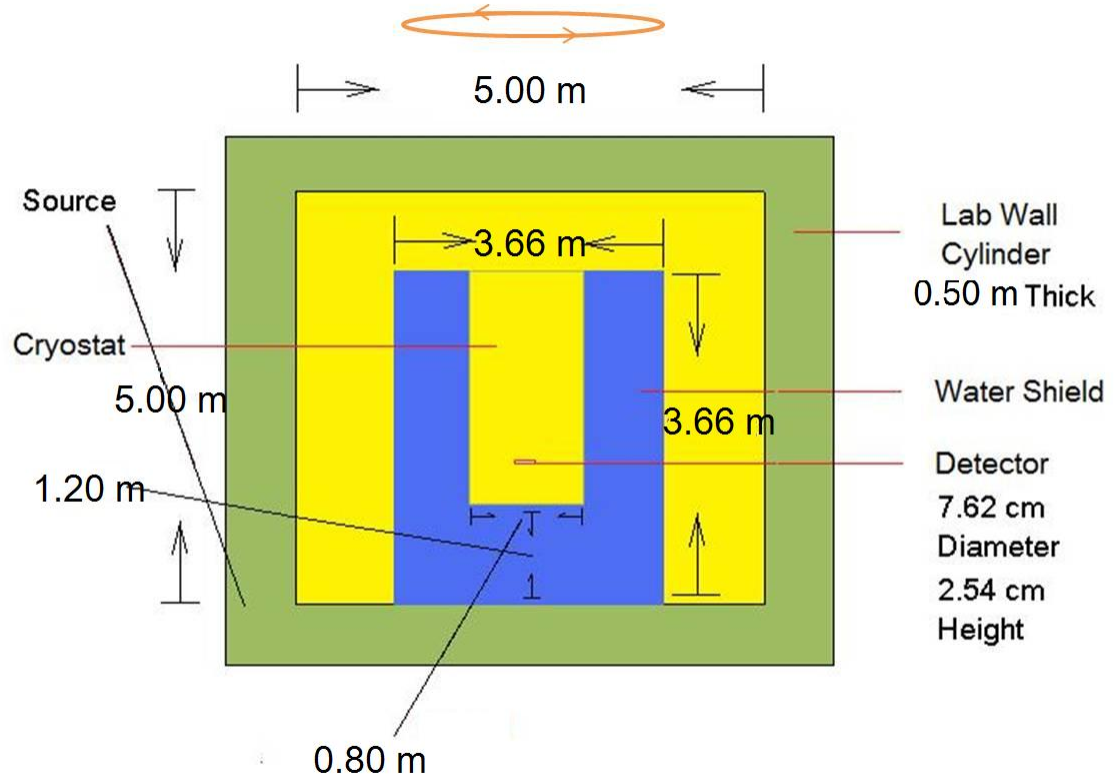


Figure 6.6: Geometry for the laboratory wall neutron in the preliminary simulation. Due to the diffusive nature of neutron, a  $0.5\text{ m}$  thick laboratory wall is included in the geometry.

again. This process can be repeated several times before the neutron can fully leave from the boundary, which made it effectively “trapped” near the boundary in the “come and go” period. If a considerable amount of energy is lost during the process, the chance for the neutron to get into the experimental area may be greatly reduced, which renders the implementation of this reflection method less useful.

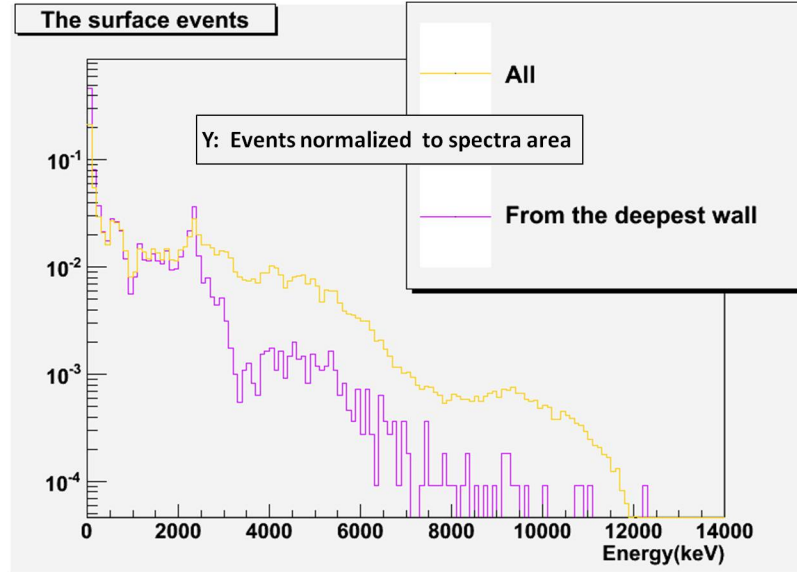
A small sample size simulation has been used to test the above reasoning: 2.75 million neutrons are thrown inside the bulk. Out of the  $\sim 5 \times 10^5$  events that enter the cavern,  $\sim 10^4$  of them are contributed by the reflection method, which gives a fraction of roughly 2%. Figure 6.7 shows the energy spectrum of these 2% neutrons

and its comparison with the total spectrum. From the comparison it is found that the two spectra behave similarly between  $\sim 0.1 \text{ MeV}$  and  $\sim 2 \text{ MeV}$ . But there is a  $\sim 25\%$  excess in the first  $100 \text{ keV}$  range in the reflection spectrum. However, since only 2% of the surface neutrons are contributed by the reflection method, this excess only affects  $\sim 0.5\%$  neutrons. Additionally, compared with the MeV neutrons, the keV neutrons are much less likely to penetrate the thick water shield, which makes the  $\sim 0.5\%$  difference even less important. Therefore it is safe to conclude that the reflection method is unnecessary. We can increase the neutron flux by 2% to easily compensate for the huge amount of rock that is not presented in the simulation.

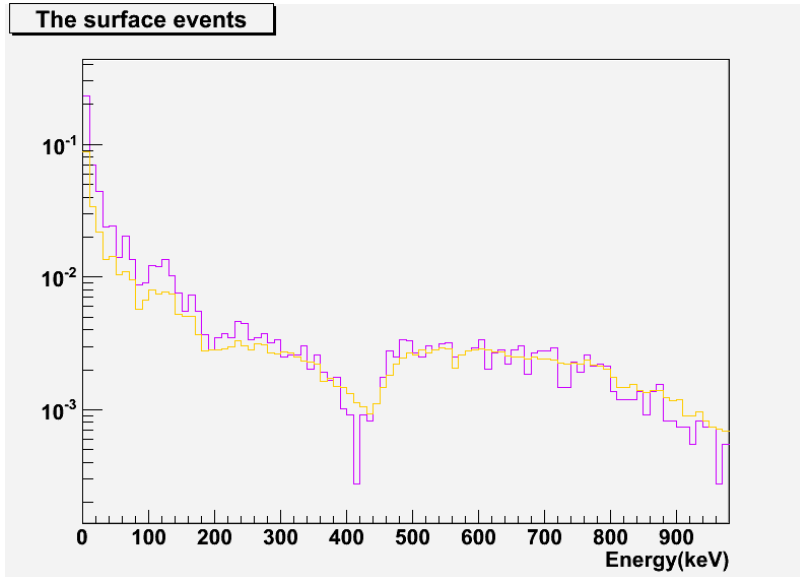
**Results from the main simulation** Given the neutron production rate of  $4.79 \text{ /year/gram}$  of rock according to our previous calculation (see section 5.2.2), the  $50 \text{ cm}$  thick norite rock layer (which is  $71 \text{ m}^3$  in terms of the total volume) then gives a neutron yield of  $32 \text{ /s}$ , or  $2.71 \text{ million/day}$ . Therefore the 127 million events simulated in this study are equivalent to  $47 \text{ days}$  of measurement time. The detector deposition is shown in Figure 6.8, where 70 events deposit energy in the detector, with 21 events being electron recoils and 49 events being nuclear recoils.

Most of the nuclear recoils have very low energy. Even for an expanded region of interest from 5 to  $100 \text{ keV}$  (typical WIMP search region is above  $10 \text{ keV}$ ), there are only 21 events ( $0.45 \text{ /day}$  in terms of detector rate). Table 6.1 shows the distribution of events in four different energy regions.

Radioactivity in the water tank is also studied in the preliminary simulation. Since the radioactivity is from the water tank, all outside volumes are discarded. Two radioactive sources are simulated in this context.



(a) Coarse binning:  $100 \text{ keV/bin}$



(b) Fine binning:  $10 \text{ keV/bin}$

Figure 6.7: Energy spectra of surface neutrons contributed by the whole volume and just by the reflection. (a) Comparison of two spectra with coarse binning. The two spectra are very similar between  $\sim 0.1 \text{ MeV}$  and  $\sim 2 \text{ MeV}$ . Beyond this range, it is calculated that in the “All” spectrum  $\sim 20\%$  neutrons are within the first bin ( $100 \text{ keV}$ ) and  $\sim 45\%$  are from beyond  $2 \text{ MeV}$ , while for the “Wall” spectrum  $\sim 45\%$  neutrons are from the first bin and  $\sim 20\%$  are from beyond  $2 \text{ MeV}$ . (b) Comparison with fine binning, cut off at  $1 \text{ MeV}$  to show excess at low energies.

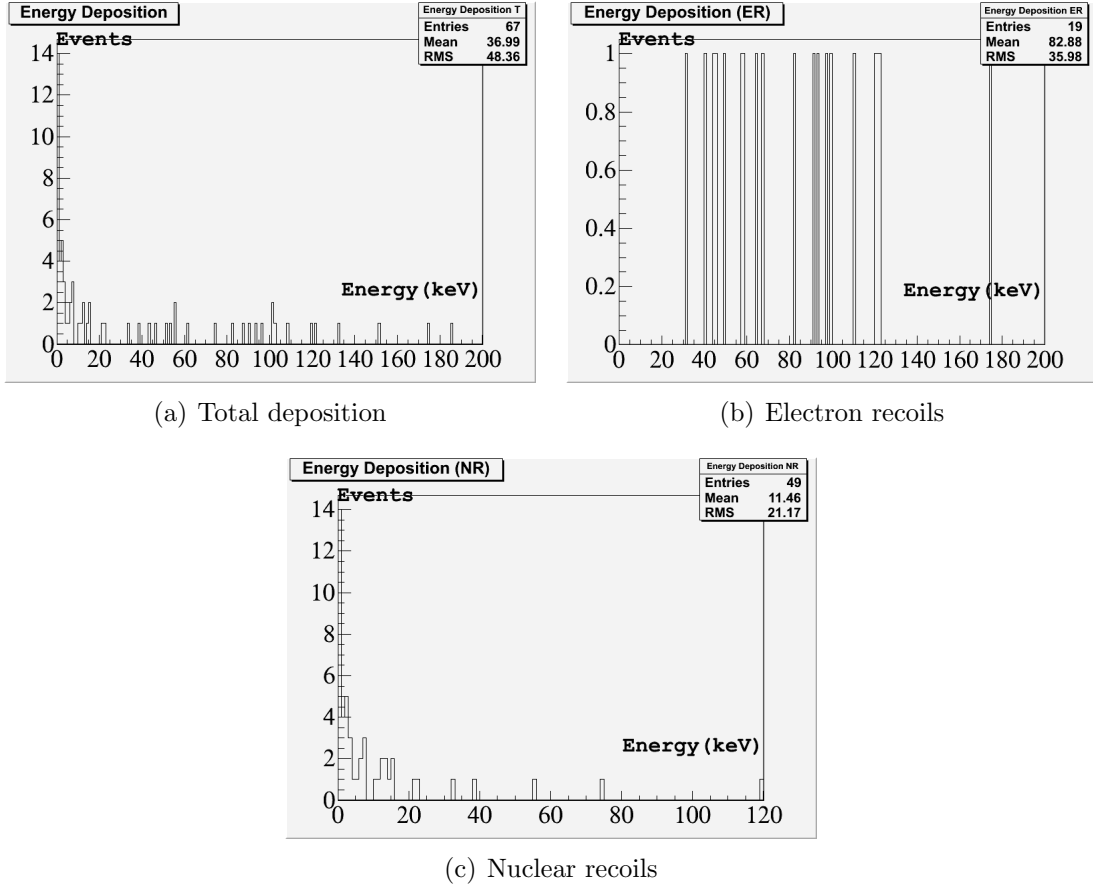


Figure 6.8: (a) 70 depositions are found in the detector, with 67 below 200 keV. (b) 21 electron recoils, with 2 above 200 keV. (c) 49 nuclear recoils, all below 200 keV.

Table 6.1: Nuclear recoils caused by laboratory wall neutrons. Events are grouped into four categories defined by different energy thresholds.

Nuclear Recoil				
Energy	< 5 keV	5 – 10 keV	10 – 100 keV	> 100 keV
No.	27	6	15	1

### 6.1.3 Radon in the water shield

**Geometry** Radon is one of the main background gamma emitters inside the water tank (see section 5.2.1). It can produce gammas with a wide range of energy. The most intense ones are shown in Table 6.2 [63]. However, to avoid complexity in the

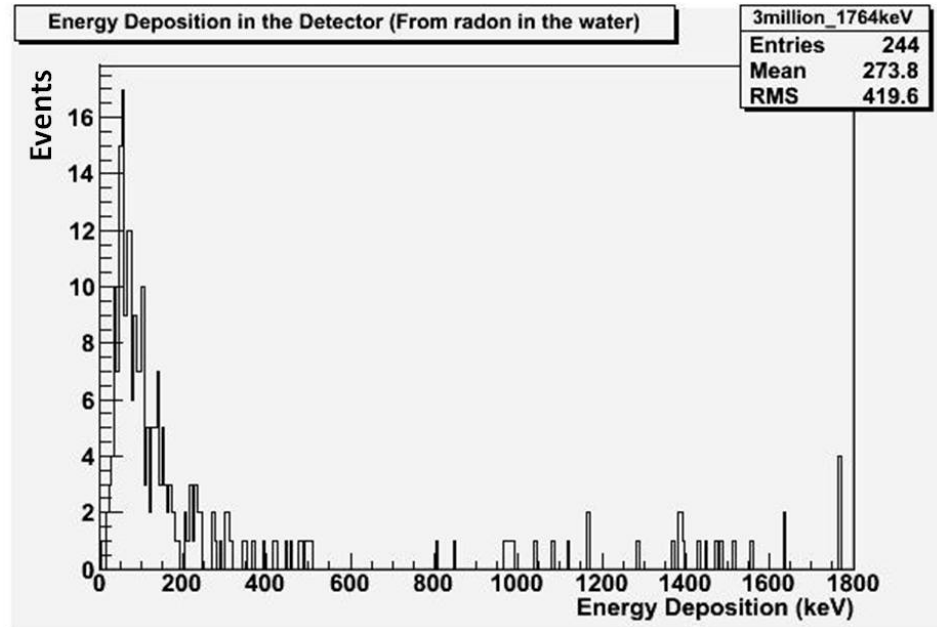
preliminary study, not all the gammas listed in the table are considered. Instead, the  $609\text{ keV}$  gamma is chosen to represent all listed gammas below  $1\text{ MeV}$  with a cumulative branching ratio of  $\sim 110\%$ , while the rest is represented by the  $1.764\text{ MeV}$  gamma with a cumulative branching ratio of  $\sim 50\%$ .

Table 6.2: Most intense gamma from radon and radon progenies' decays (BR stands for branching ratio).

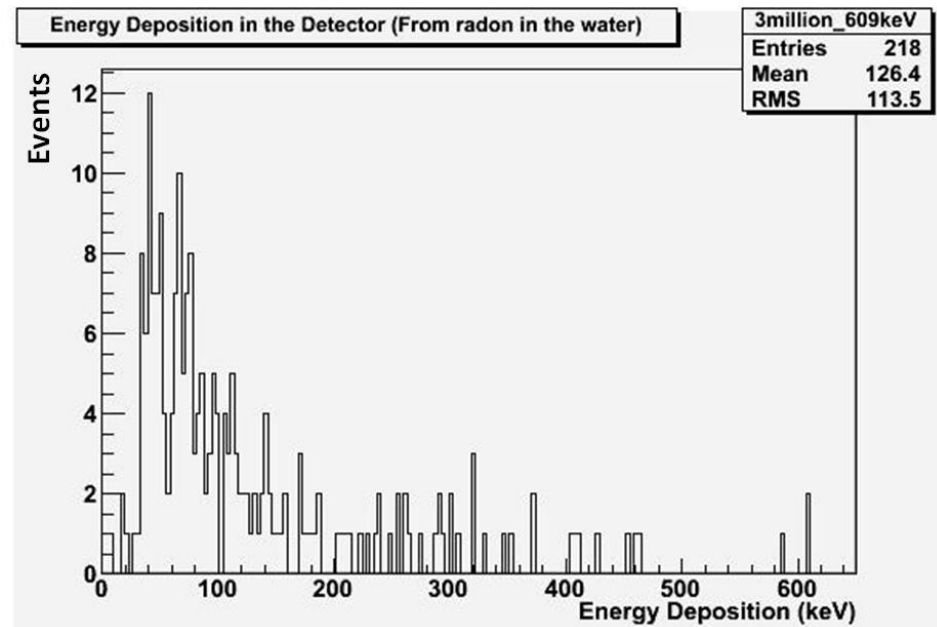
E(keV)	Origin	BR
242.0	$\beta$ $^{214}\text{Pb}$	7.43%
295.2		19.3%
351.9		37.6%
609.3		46.1%
total		110.43%
1120.3	$\beta$ $^{214}\text{Bi}$	15.1%
1238.1		5.79%
1377.7		4.00%
1729.6		2.92%
1764.5		15.4%
1847.4		2.11%
2204.2		5.08%
total		50.4%

Two independent simulations are run for the  $1764\text{ keV}$  and the  $609\text{ keV}$  gamma respectively. Figure 6.9 shows the result.

Assuming the activity of radon in the water is  $10\text{ Bq}/m^3$  (the radon level in SNO-LAB air is about  $100\text{ Bq}/m^3$  [56]; if the water is fully saturated with radon, the activity is 10 times less than in the air [64], but it is an unlikely case that the water is fully saturated, so the actual activity is probably less than this value) and the water tank is roughly  $40\text{ m}^3$ , the 110% branching ratio of the  $609\text{ keV}$  gamma makes its 3 million events equivalent to  $1.89\text{ hours}$ , while the 50% branching ratio of the  $1764\text{ keV}$  gamma makes the value  $4.16\text{ hours}$ . The detector rate is therefore  $0.98/\text{minute}$  for



(a) 1764keV



(b) 609keV

Figure 6.9: Energy deposition from gamma produced by radon in the water shield. (a) 3 million events are run for the  $1764\text{ keV}$  gammas. 244 depositions are found in the detector. (b) The same sample size is run for the  $609\text{ keV}$  gammas, with slightly less depositions recorded.

$1764\text{ keV}$  gamma and  $1.92/\text{minute}$  for  $609\text{ keV}$  gammas.

### 6.1.4 $^{60}\text{Co}$ in the water shield

**Geometry**  $^{60}\text{Co}$  is the other radioactive source coming along with the water shield, with a characteristic emission of  $1.17\text{ MeV}$  and  $1.33\text{ MeV}$  gammas. It is located inside the steel can that holds the water. To accurately locate the gamma source, two additional layers are added on top of the geometry for the radon simulation. The steel can is placed in the outmost of the water tank, with a PVC layer mounted between the water and the steel (Figure 6.10).

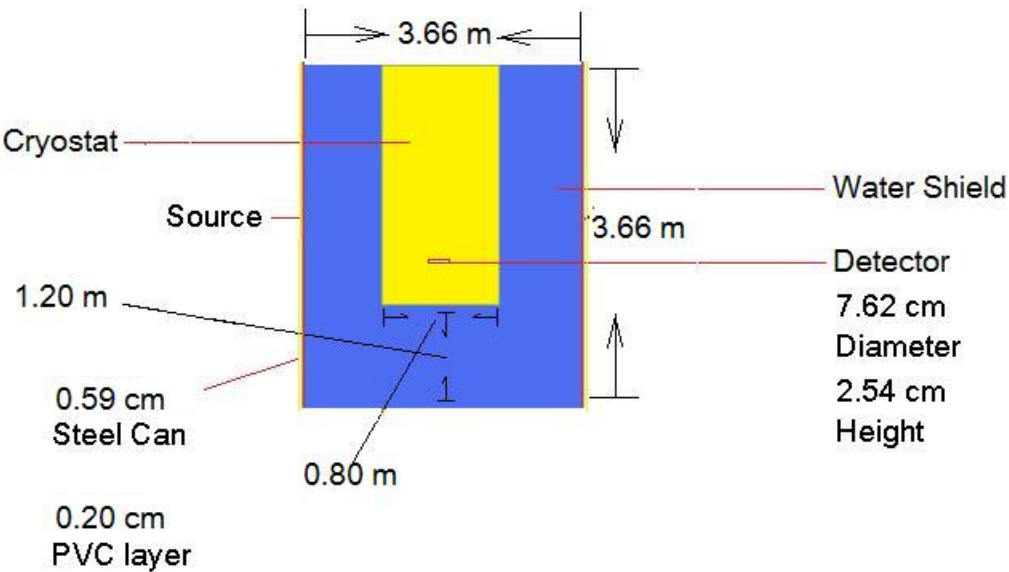


Figure 6.10: Geometry for the preliminary simulation of  $^{60}\text{Co}$  gammas from the steel tank. The very thin layers are the steel tank and PVC layer for the water shield: outer yellow is the steel tank ( $0.59\text{ cm}$  thick,  $\sim 2.06\text{ tons}$ ,  $8.00\text{ g/cm}^3$ ), inner red is the PVC layer ( $0.20\text{ cm}$  thick,  $1.54\text{ g/cm}^3$ ).

$^{60}\text{Co}$  is a common additive in the standard stainless steel production procedure. In our application, we assume the  $^{60}\text{Co}$  contamination level in the steel tank to be the largest one reported by ILIAS [65], which is 230 mBq/kg, 10 times larger than all the other reported values. Since the weight of the steel can is  $\sim 2000\text{ kg}$ , this activity means that the 500 million decays simulate here are equivalent to 12.26 *days* of measurement time.

Unlike the way to treat the radon gammas, the two gammas from  $^{60}\text{Co}$  are considered simultaneously in one combined simulation. Figure 6.11 shows the result. The 139 detector depositions then give a detector rate of  $\sim 10\text{ /day}$ .

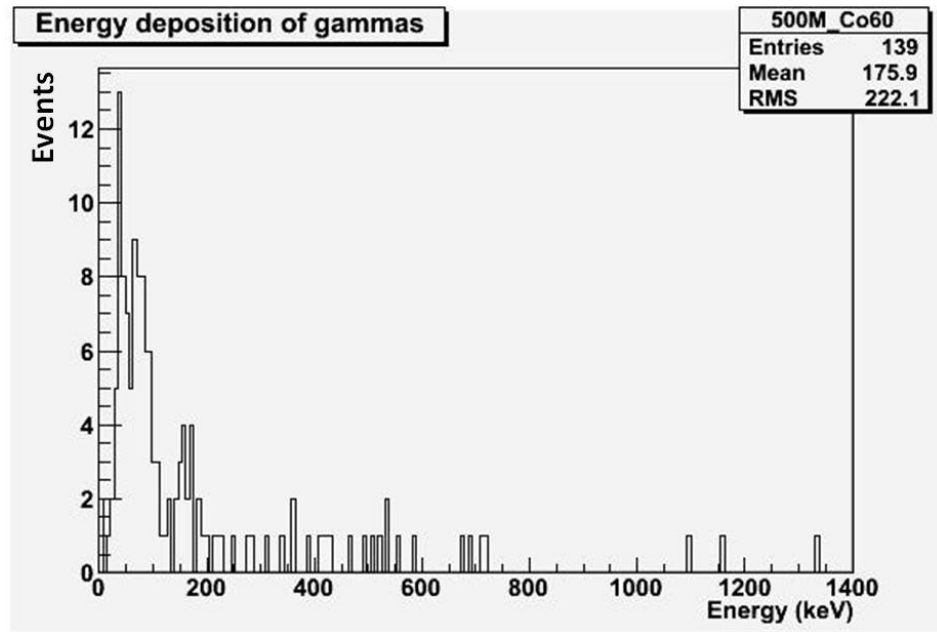


Figure 6.11: Energy deposition from the  $^{60}\text{Co}$  radiation in the steel tank. 500 million events are run in the simulation.

### 6.1.5 Conclusion

Table 6.3 shows a summary of all the preliminary simulations. The cumulative gamma rate as well as the neutron rate is listed. Either rate is lower than the target

rate, indicating the proposed 12 *feet* by 12 *feet* water tank is effective in reducing the background radiation to an acceptable level.

Table 6.3: Summary on preliminary simulations

Particle Type	Location	Source	Detector Rate	Target Rate
Gamma	Laboratory wall	2.615 <i>MeV</i> from thorium decay chain	0.013 / <i>s</i>	
	Water shield	1764 <i>keV</i> and 609 <i>keV</i> from radon decays	0.048 / <i>s</i>	
	Water shield	$^{60}\text{Co}$	0.0001 / <i>s</i>	
Total			0.0611 / <i>s</i>	1 / <i>s</i>
Neutron	Laboratory wall	Spontaneous Fission & $\alpha$ -n	0.32 / <i>day</i> (10-100 <i>keV</i> )	1 / <i>day</i>

### 6.1.6 Study of influence of cavity size and shape

This study begins with the background neutrons in the simplified setup from the preliminary simulation. The result from this work is never used to benefit any actual simulations, but rather indicating a way to carry out the later study for the more detailed and truthful geometry methodologically.

The preliminary experimental hall is a cylinder, 5 *meters* in both height and diameter. Background neutrons sampled from the simplified spectrum (Figure 5.7) are thrown from inside the laboratory wall volume. Once crossing the boundary to enter the cavern, the neutrons are killed but their position and energy are recorded.

Several regions are selected on the laboratory wall surface, from which the neutron fluence can be sampled under different geometrical conditions (Figure 6.12): a 10 *cm* wide belt on top and bottom plane (Base C Ring; green); a 10 *cm* wide belt on top and bottom side wall (Wall C Belt; red, the bottom one is not shown here); a 2 *m* in diameter circle in the center of top and bottom plane (Base Circle; blue); and a 2 *m*

wide belt on the side (Wall Belt; violet). The green and red regions represent corners, while the other two represent flat surface. The width of the green and red belts are selected to be  $10\text{ cm}$ , because the mean free path of  $1\text{ MeV}$  neutrons in the norite rock is approximately  $1.7\text{ cm}$ , while five scattering lengths is probably large enough to define the boundary between corner and non-corner regions.

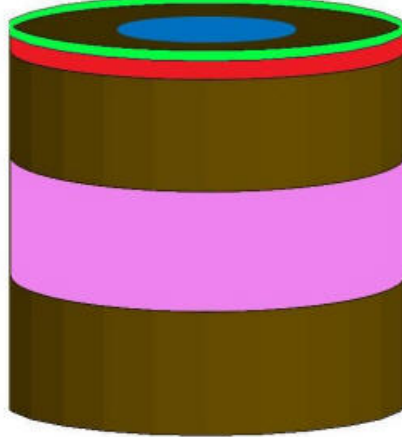


Figure 6.12: Different regions defined from the preliminary experimental hall.

It is expected that neutron fluence from the corners is different from that from the flat surface. This can be seen from Figure 6.13, where Figure 6.13(a) is comparing the absolute fluence, while 6.13(b) is showing the relative difference D:

$$D = \frac{F_s - F_a}{F_a} \quad (6.1)$$

where  $F_s$  is the fluence sampled from a specific region;  $F_a$  is the fluence sampled over the entire surface. From 6.13(b), it is clear that the fluence of low energy neutrons from the corners (green and red) is higher than that from other two regions (blue and pink), while the difference seems to disappear at  $\sim 5\text{ MeV}$ . There is no evidence for a deviation at high energy, but statistical uncertainties are fairly large.

The low energy behavior is reasonable. Firstly, the amount of material behind the

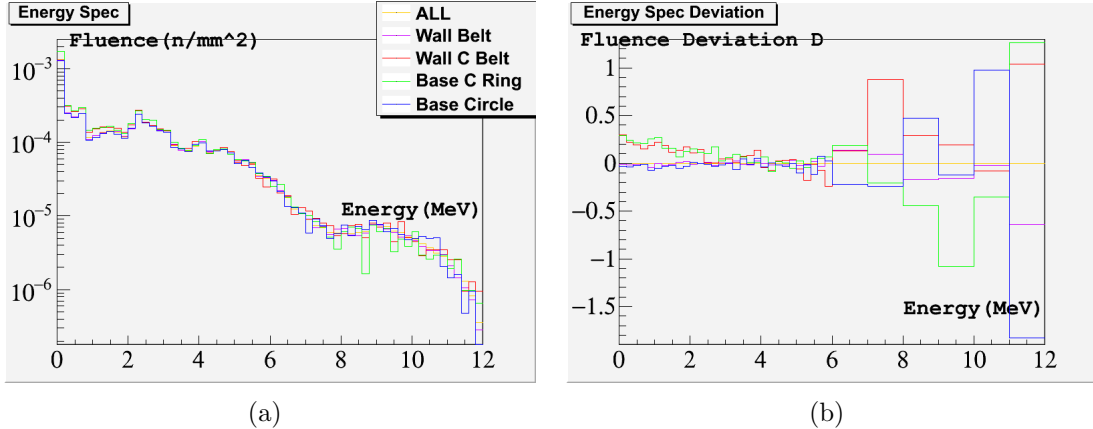


Figure 6.13: Comparison of neutron fluence from different regions. (a) Comparing the absolute fluence ( $200\text{ keV/bin}$ ). (b) Comparing the deviation. Below  $6\text{ MeV}$ , the bin width is  $200\text{ keV}$ . Above  $6\text{ MeV}$ ,  $1\text{ MeV/bin}$  is used to reduce the statistical fluctuation. Up to  $\sim 4\text{ MeV}$ , the corner flux (green and red) is clearly higher than flux from other regions ( $\sim 10\%$  on average). Beyond  $\sim 6\text{ MeV}$ , statistical uncertainties become too large to make any reasonable conclusion.

corner surface is greater than any other regions, therefore a higher neutron production rate is expected. Secondly, since neutrons generated from this “extra material” are on average subject to more interactions before reaching the surface than neutrons from the surface vicinity, they are shifted to lower energy, resulting in a low energy excess as reflected in the spectrum. The difference is as high as 20% up to around  $2\text{ MeV}$ . However, this difference may become much less important if weighted by ratio of area between corner and flat surface, which means in a larger geometry we will have a less important corner effect and in a smaller geometry the importance will be enhanced.

## 6.2 Detailed Simulation

After the preliminary simulations showed that the proposed shield is likely to be sufficient, a series of detailed simulations are done on top of the preliminary ones, aimed at getting a deeper insight into the background radiation faced by the STF.

The advancement of these new trials lies in the much more detailed geometry, the much more thorough consideration put into the initial spectra, and the more plausible way to extract information from the simulation. Certainly not the last version, this work is expected to provide results to compare with data taken from the future experiment, offering identification and classification of observed background events.

### 6.2.1 Geometry

In the preliminary simulation, the experimental area is taken as a hollow cylinder, which is completely different from the actual configuration. The space reserved for the STF at SNOLAB can be described as a long tunnel with different cross sections at different places along the tunnel, where branching tunnels can be occasionally found on the side wall (Figure 6.1). In the detailed simulation, this area is put into the geometry in a more truthful way. It is simplified as a  $10\text{ m}$  long tunnel with constant cross section, which is approximated by a best fit of the “F-F” section where the STF is expected to be placed (Figure 6.14). However, this may not be a proper simplification, for the actual tunnel is longer and is closed on both ends. To overcome this shortage, a translation method is used. In this method, particles that are about to leave the tunnel from one end are instantly translated to the other end, which makes them go back to the tunnel without changing momentum and energy. By doing this, particles that get translated can be thought coming from volumes outside the tunnel, in a way making the length effectively infinite.

Through a simple simulation, we determined that the skin depth for the  $2.615\text{ MeV}$  gamma in the norite rock was  $13\text{ cm}$ . Since three skin depths may prevent about 99% of the gammas from penetrating from one side to the other, in the detailed simulation we set the thickness of the wall to be  $40\text{ cm}$  for gammas. For neutrons, we stayed with the  $50\text{ cm}$  from the preliminary simulation.

Figure 6.15 shows the overall geometry in the detailed simulation.

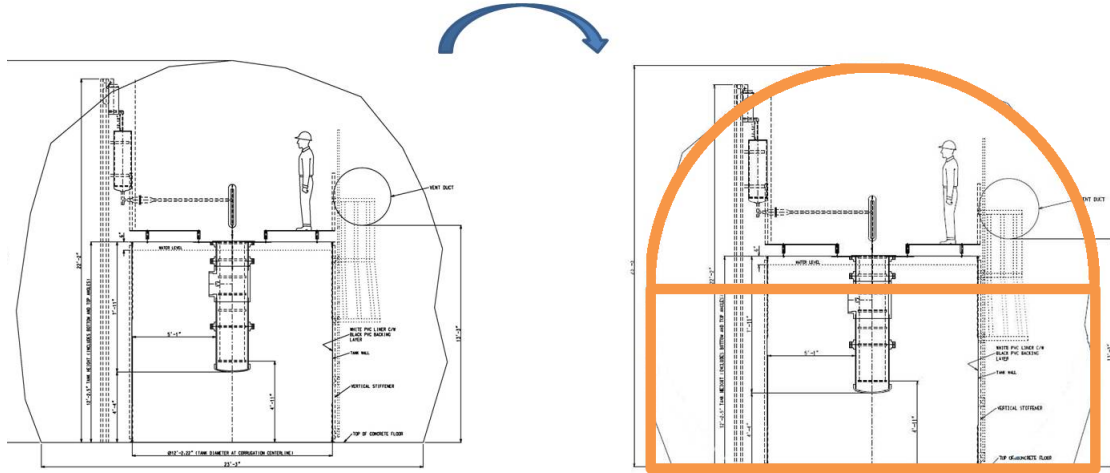


Figure 6.14: Best fit of the F-F section in the tunnel. A combination of a half circle and a rectangle can well approximate the actual shape of that cross section.

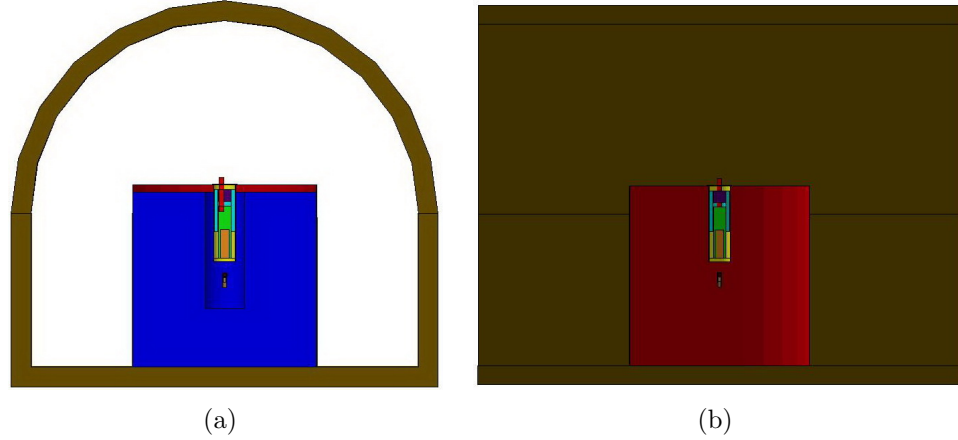


Figure 6.15: Geometry of the experimental area in the simulation. Geometry of the STF is also shown, which will be discussed below in more details. (a) The front cutaway view of the experimental setup. (b) The side cutaway view of the experimental setup.

The water shield stays the same as in the preliminary simulation, while the cryostat, which was earlier treated as an empty cylinder filled with air, should be included in the detailed study. Figure 6.16 shows the details of the simulated geometry and

how they are related to the actual cryostat. Its appearance in the simulation is also plotted.

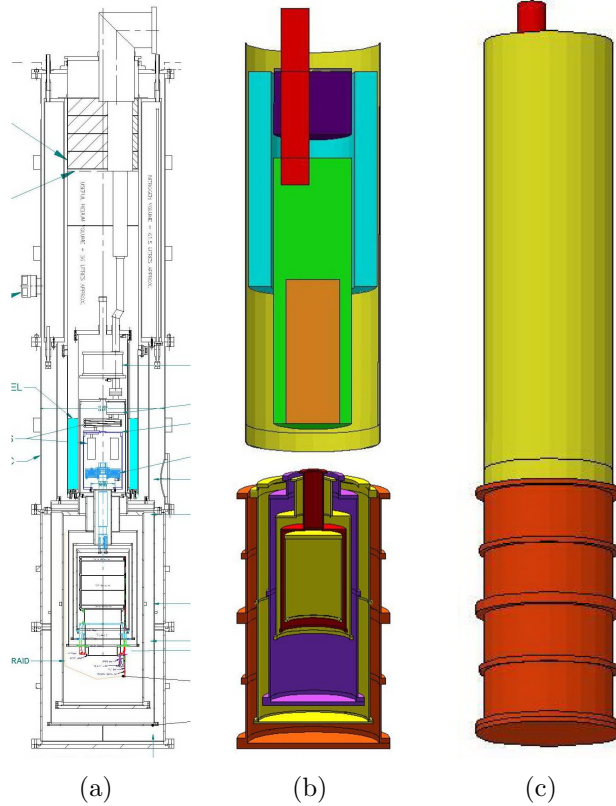


Figure 6.16: The cryostat and its geometry in the simulation. (a) The engineering drawing of the cryostat. (b) The cutaway view of its geometry in the simulation. The actual cryostat is simplified into several pieces which are then going to the simulation. The red is filled with air, representing the still pumping line; the purple is representing the space between the top of the cryostat and the helium volume, which may be filled with foam later but now with air in the simulation; the gray is a thin aluminum layer representing the top flange which is thought to be able to block radiation from the top; the blue is for the liquid nitrogen; the green is for the liquid helium, the height of which can vary during the actual run; the orange represents the dilution unit of the cryostat. It is treated as a low density copper in the simulation, with a total mass close to the estimated mass of the actual unit. (c) The closed view.

The bottom part of the original cryostat, the so called tails are too small for the detectors to be tested and will be replaced by new larger tails. They are made up

of six nested cans, housing the detectors and providing thermal connection with the upper cryostat. Since this part is relatively close to the detectors, details including flanges which are not considered in constructing the geometry of the upper part of the cryostat are taken into account. The appearance of the tails as part of the simulated geometry and its connection with the upper cryostat are as well shown in Figure 6.16.

Inside the cryostat tails, detectors are mounted within the detector housing. They are newly designed Ge detectors with *3 inches* in diameter and *1 inch* in height. The detector housing is simulated as accurately as possible, even including some structural parts of the readout electronics (“side coaxes”) (Figure 6.17).

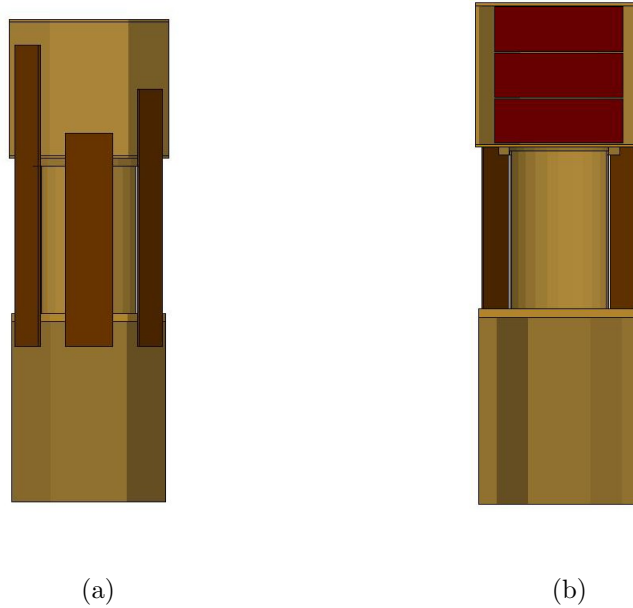


Figure 6.17: The detector housing and the interior detectors. (a) Front view of the detector housing. Side coaxes are shown in dark brown. (b) Cutaway view, where three detectors are shown in red.

### 6.2.2 Surface Spectrum Study

The simulations carried out in this work are all rather time consuming, partly due to the large dimension of the experimental area ( $\sim 10\text{ m} \times 10\text{ m} \times 10\text{ m}$ ) and the complicate chemical composition of the rock (14 different elements). Therefore some speedup methods are needed. We notice that the simulation in the rock takes a significant amount of time, and a large fraction of the particles never make it out of the rock at all. Therefore we first determine the spectrum at the rock surface and then use this to continue. By comparing particle fluence under different geometrical conditions, this work also examines if a carefully selected surface spectrum can satisfactorily represent particle fluxes sampled from all different regions on the laboratory wall surface, especially the corners where a higher particle flux is expected.

Based on the surface fluence study for the preliminary geometry (section 6.1.6), a similar study is done for the new tunnel geometry (section 6.2.1), as a preparation for the detailed simulation. A surface spectrum is created for each type of background radiation for the purpose of generating throws from the surface.

Gammas are also considered in this work, for the size of the current geometry requires significant amount of computing time to get reasonable statistics. A so called “line source” simulation with a very simple setup is adopted here as a new approach for obtaining the surface spectrum (Figure 6.18): a line source is located at the center of a cuboid, which is as thick as the laboratory wall considered in the simulation. In the other two dimensions, the cuboid is large enough to make the particles escape from only one direction. The escaped particles are then killed while their energy is recorded. This approach is mainly used to create the gamma surface spectrum, while it is also adopted for the neutrons as a reference. The advantage of this method is that it allows us to have good statistics in a relatively short computing

time. The spectrum obtained this way is named the “line source spectrum”. Its compatibility with the spectrum sampled from the particles escaping from the tunnel shaped geometry will be discussed in the rest of this subsection.

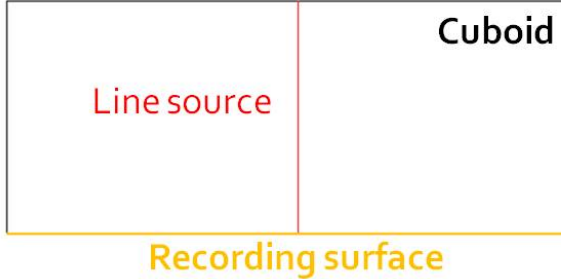


Figure 6.18: The line source approach. The red line shows how the line source is located, while the yellow line indicates the surface which is reserved for recording the escaping particles.

Similar to the preliminary study, six regions are selected at the surface of the tunnel (Figure 6.19): a  $60\text{ cm}$  wide region from the top of the arch (ARCT60); a  $60\text{ cm}$  wide region from the side wall (WCT60); a  $60\text{ cm}$  wide region from the bottom (BCT60); a  $15\text{ cm}$  wide region on the bottom, plus a  $15\text{ cm}$  wide region on the wall near the corner (CN30), and each of them separately(BCN15 and WCN15). Besides comparison between each other, they are also compared with the line source spectrum.

Within the selected regions, the corner is defined as the joint of two  $15\text{ cm}$  wide adjacent flat surfaces for two main reasons:

- The dimension can ensure the same surface area as the other regions.
- It is validated by examining the spread of the escaping particles from the line source test (Figure 6.20). It is found that the spread of any line source is not a uniform distribution. There are deviations in the region. For the background neutrons, the spread is close to a normal distribution (Figure 6.21(a)), with  $\sigma \approx 11.4\text{ cm}$ . For the thorium and uranium gammas (Figure 6.21(b) and Figure

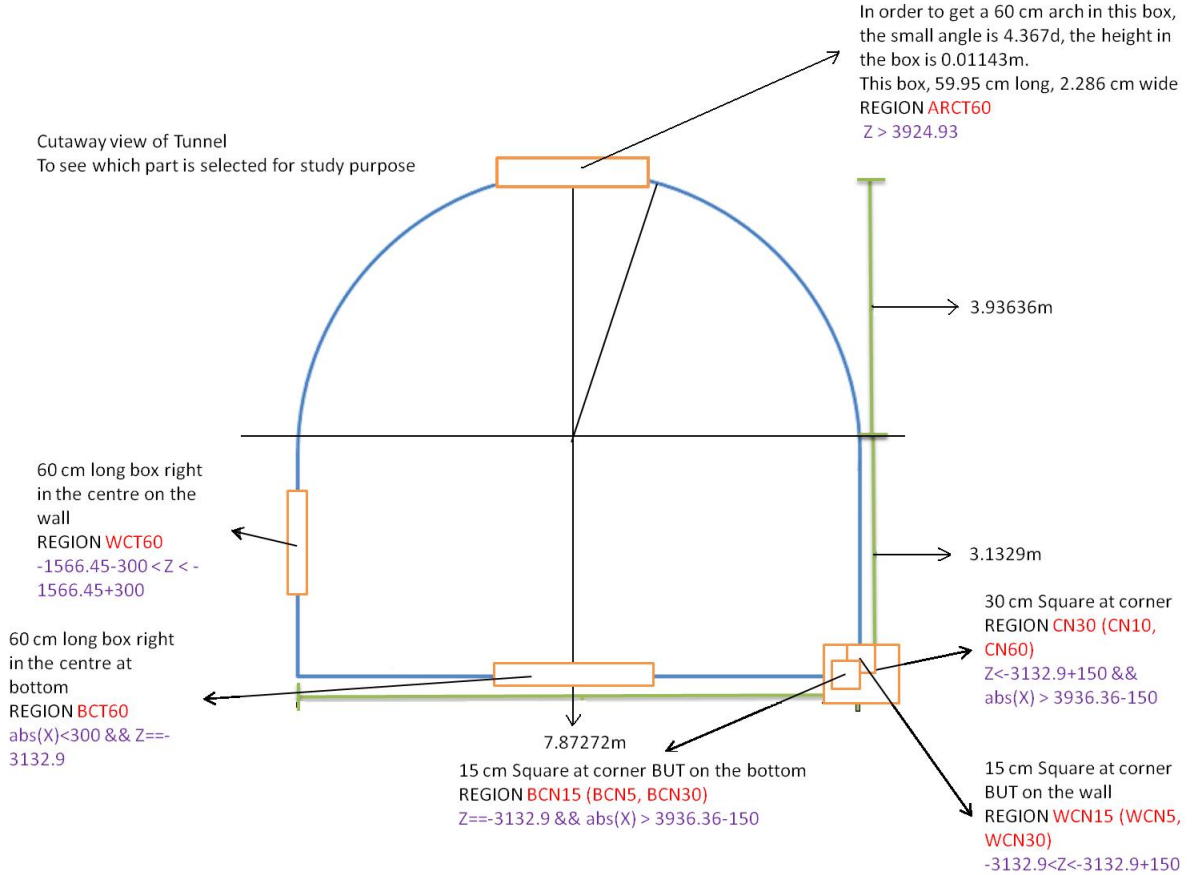


Figure 6.19: Different regions selected from the current geometry.

6.21(c)), the distributions are almost exponential, with the  $1/e$  fold point at  $\sim 6.2\text{ cm}$ . These values are all below  $15\text{ cm}$ , indicating the  $15\text{ cm}$  width we selected to represent the corner region is reasonable.

### Study for the background gamma

The thorium and uranium decay chain gammas are studied in this context. Within each decay chain, the 20 most intense gammas are considered (Table 6.4, Table 6.5) [66]. The  $^{40}\text{K}$  gamma is also mentioned, but only the surface spectrum is listed at the end of this section with no additional details discussed.

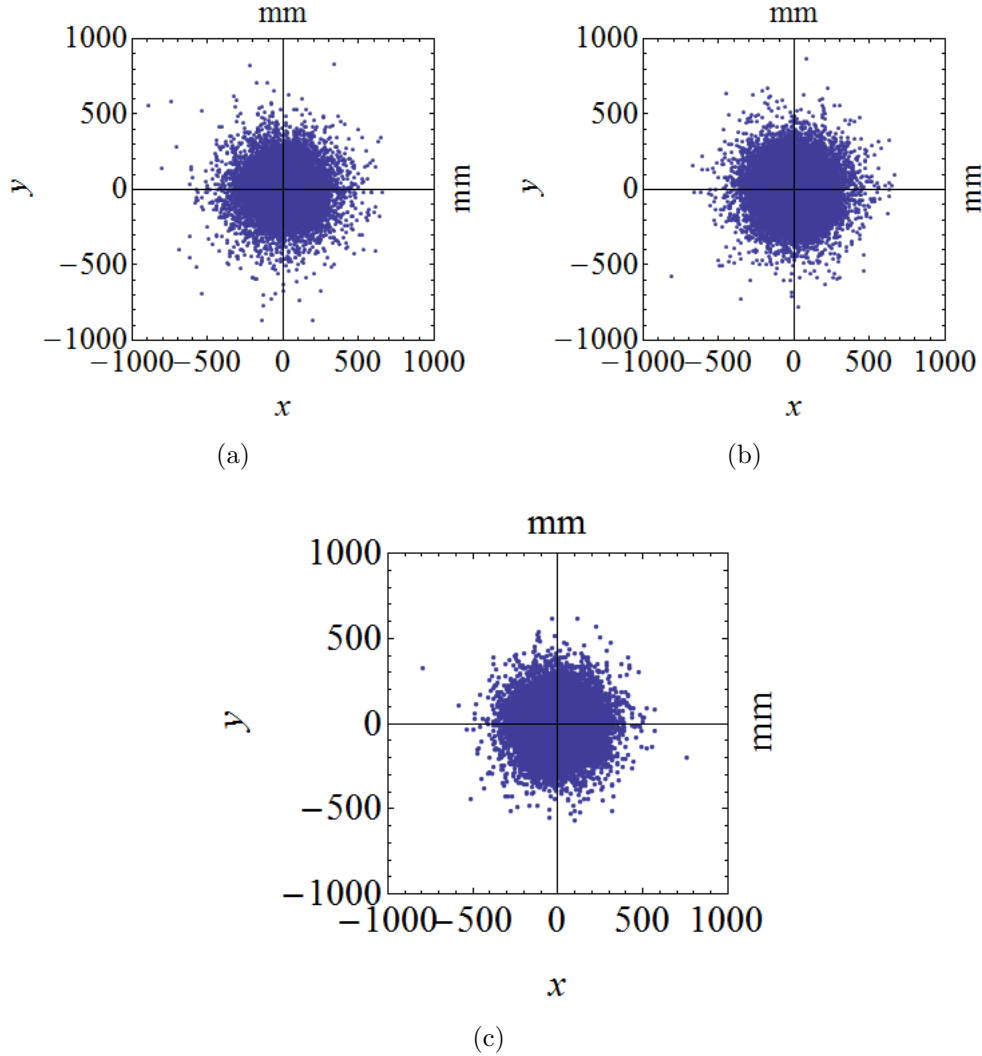


Figure 6.20: Distribution of different escaping particles as collected from the line source test. (a) Background neutrons(mm). (b) Gamma from the thorium decay chain.(c) Gamma from the uranium decay chain.

Both the absolute fluence and the deviation are compared among spectra sampled from different regions (Figure 6.22 and Figure 6.23). In order to include the line source spectrum into the comparison, we defined an “equivalent area” for the line source as the flat area (either WCT or BCT region) behind which the same number of events would be started. For either decay chain gammas, the corners (red, green, black) exhibit a larger fluence than any other regions up to  $500 \text{ keV}$ , but the difference

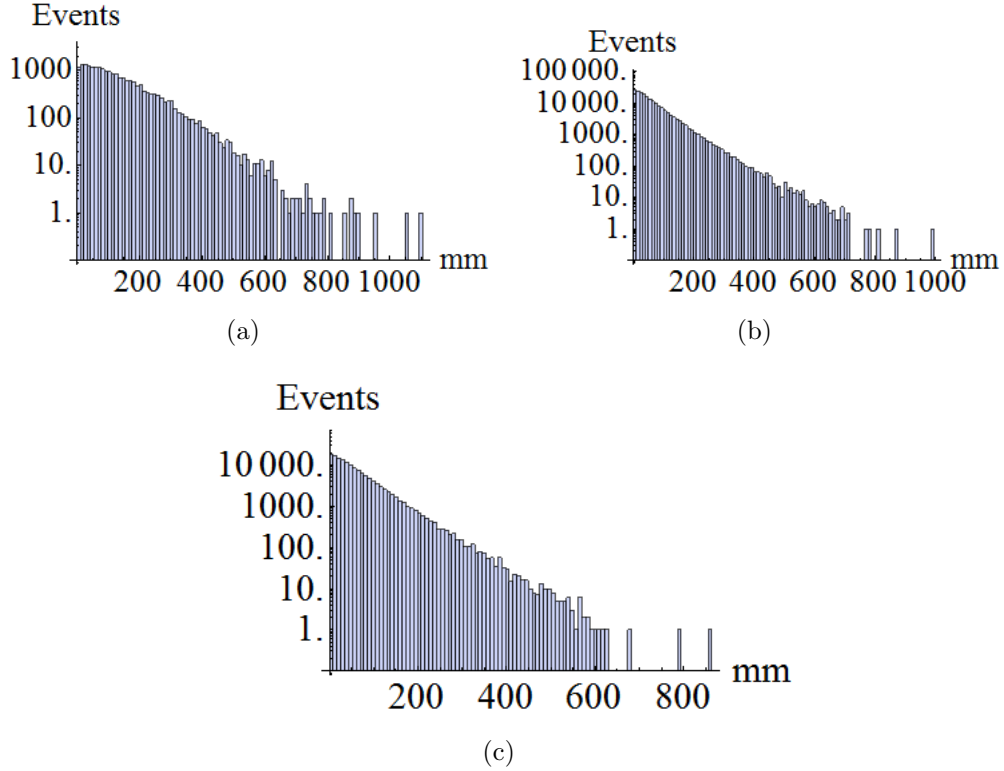


Figure 6.21: After calculating the distance  $r$  of every point on the spread to the center, a  $r$  histogram is plotted for each line source spread. (a) The distribution of the background neutrons is close to a normal distribution with  $\sigma \approx 11.4\text{ cm}$ . Either the distribution of the thorium gammas (b) or the distribution of the uranium gammas (c) is close to an exponential distribution, with  $1/e$  fold point at  $\sim 6.2\text{ cm}$ .

is less than 5% on average. This is expected and the reason is already explained in the preliminary study. The line source spectrum is found compatible with either the WCT or BCT spectrum within 5% (excluding places where statistical fluctuations dominate).

Based on the comparison already done, it is still difficult to decide if two histograms are compatible or not. So I introduce a hypothesis test method to check the compatibility. This test is carried out bin by bin. Because the number of events follow a normal distribution, if assuming the observed number being the mean value (this approximation works when the number is large) and its square root being the

Table 6.4: The 20 most intense gammas from the thorium decay chain, sorted by gamma energy.

E(keV)	Intensity per $^{232}\text{Th}$ decay	Parent isotope
129.0	0.025	$^{228}\text{Ac}$
209.0	0.039	$^{228}\text{Ac}$
239.0	0.436	$^{212}\text{Pb}$
241.0	0.040	$^{224}\text{Ra}$
270.0	0.034	$^{228}\text{Ac}$
277.0	0.023	$^{208}\text{Tl}$
300.0	0.033	$^{212}\text{Pb}$
328.0	0.030	$^{228}\text{Ac}$
338.0	0.113	$^{228}\text{Ac}$
463.0	0.044	$^{228}\text{Ac}$
511.0	0.081	$^{208}\text{Tl}$
583.0	0.304	$^{208}\text{Tl}$
727.0	0.067	$^{212}\text{Bi}$
795.0	0.043	$^{228}\text{Ac}$
861.0	0.045	$^{208}\text{Tl}$
911.0	0.266	$^{228}\text{Ac}$
965.0	0.051	$^{228}\text{Ac}$
969.0	0.162	$^{228}\text{Ac}$
1588	0.033	$^{228}\text{Ac}$
2615	0.356	$^{208}\text{Tl}$

standard deviation, the null hypothesis is given by:

Two histograms are compatible in a specific bin. If the bin content is defined as  $\mu_1$  and  $\mu_2$  respectively, this condition is mathematically expressed as  $\mu_1 - \mu_2 = 0$ .

Given the 95% confidence level, then the test is to see if the probability  $P(z > |\mu_1 - \mu_2|/\sqrt{\sigma_1 + \sigma_2})$  is greater or smaller than 5% (where  $z$  is the random variable of a standard normal distribution). If it is greater, then the null hypothesis is accepted and the two histograms are compatible in this bin; if smaller, then the null hypothesis is rejected, leaving the two histograms not compatible in that bin. A simple code is

Table 6.5: The 20 most intense gammas from the uranium decay chain, sorted by gamma energy. “Natural U” contains 95.6%  $^{238}\text{U}$  and 4.4%  $^{235}\text{U}$ .

E(keV)	Intensity per natural U decay	Parent isotope
46.5	0.039	$^{210}\text{Pb}$
63.3	0.043	$^{234}\text{Th}$
92.4	0.025	$^{234}\text{Th}$
92.8	0.024	$^{234}\text{Th}$
186.0	0.035	$^{226}\text{Ra}$
186.0	0.025	$^{235}\text{U}$
242.0	0.072	$^{214}\text{Pb}$
295.0	0.177	$^{214}\text{Pb}$
352.0	0.342	$^{214}\text{Pb}$
609.0	0.428	$^{214}\text{Bi}$
768.0	0.046	$^{214}\text{Bi}$
934.0	0.029	$^{214}\text{Bi}$
1120	0.141	$^{214}\text{Bi}$
1238	0.056	$^{214}\text{Bi}$
1378	0.037	$^{214}\text{Bi}$
1408	0.027	$^{214}\text{Bi}$
1509	0.020	$^{214}\text{Bi}$
1730	0.028	$^{214}\text{Bi}$
1765	0.147	$^{214}\text{Bi}$
2204	0.046	$^{214}\text{Bi}$

written to do this test automatically, which can produce a histogram to express the result. The produced histogram has the same range and bin width as the compared histograms, but the bin content is assigned to be 1 if the two histograms are found compatible in that bin, -1 if not, and 0 if no events exhibited. Because this test is done on the 5% significance level, the two histograms are regarded overall compatible if less than 5% of bins are not compatible.

Figure 6.24 and Figure 6.25 indicates for both thorium and uranium decay chain gammas there is an overall compatibility among all the compared configurations ex-

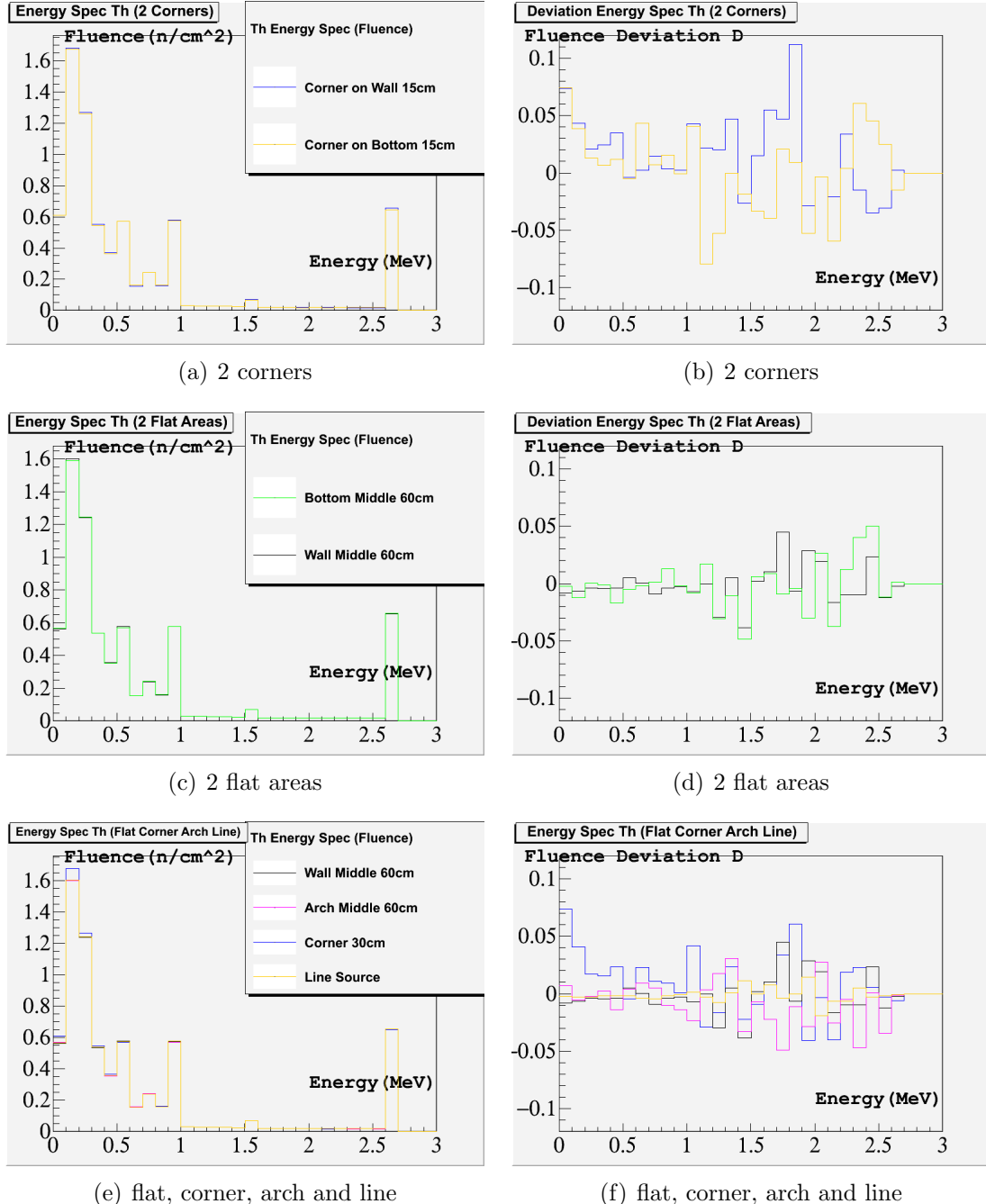


Figure 6.22: Comparison of the absolute fluence (a)(c)(e) and the deviations (b)(d)(f) of gammas from the thorium decay chain from different regions.

cept for the corners, where clear incompatibility steps in up to 500 keV. This result agrees with the observation from the early comparison before the hypothesis test is

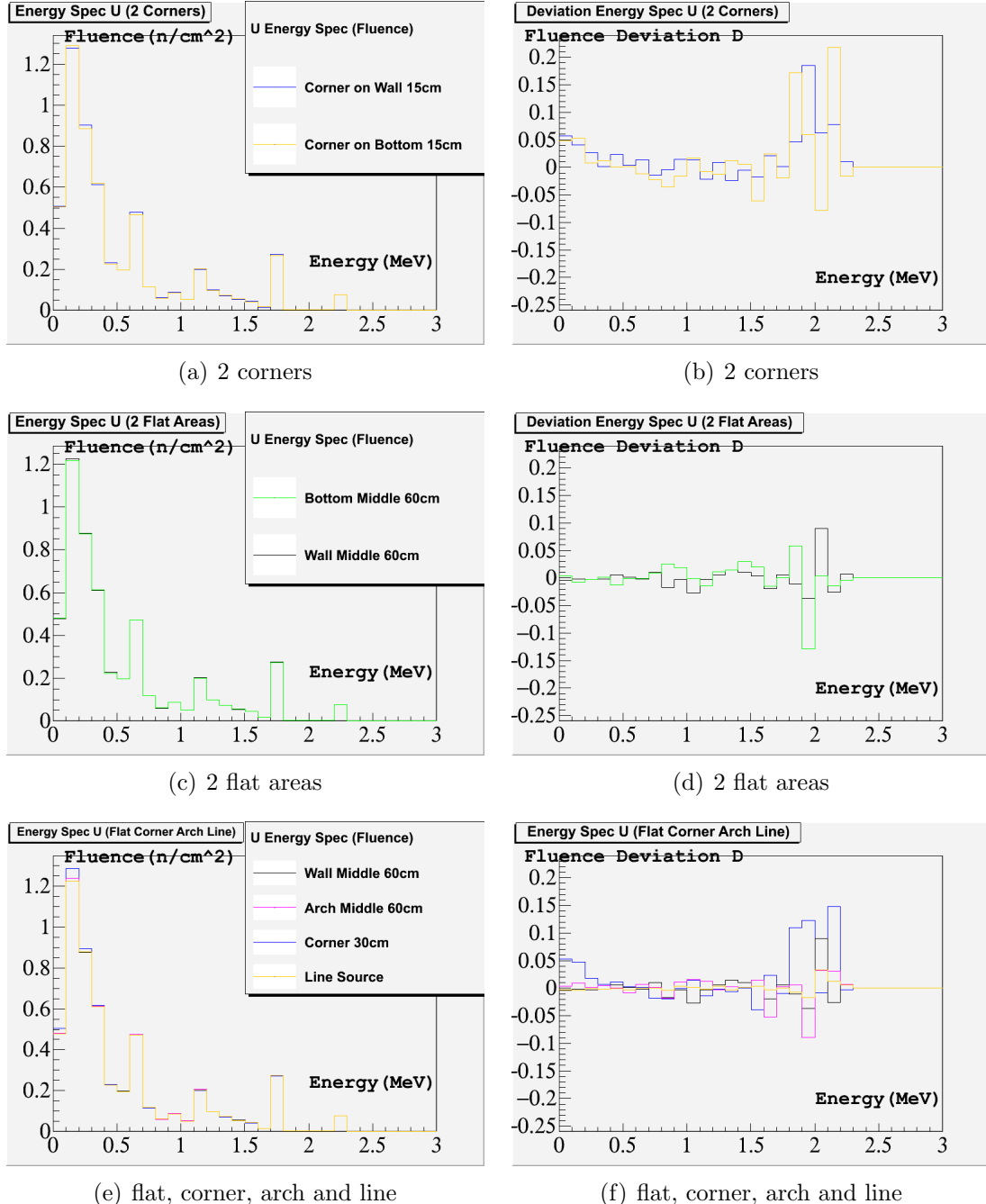


Figure 6.23: Comparison of the absolute fluence (a)(c)(e) and the deviations (b)(d)(f) of gammas from the uranium decay chain from different regions.

used. Therefore it is reasonable to implement the line source spectrum to represent the flux over the entire laboratory wall surface, while extra throws may be needed in

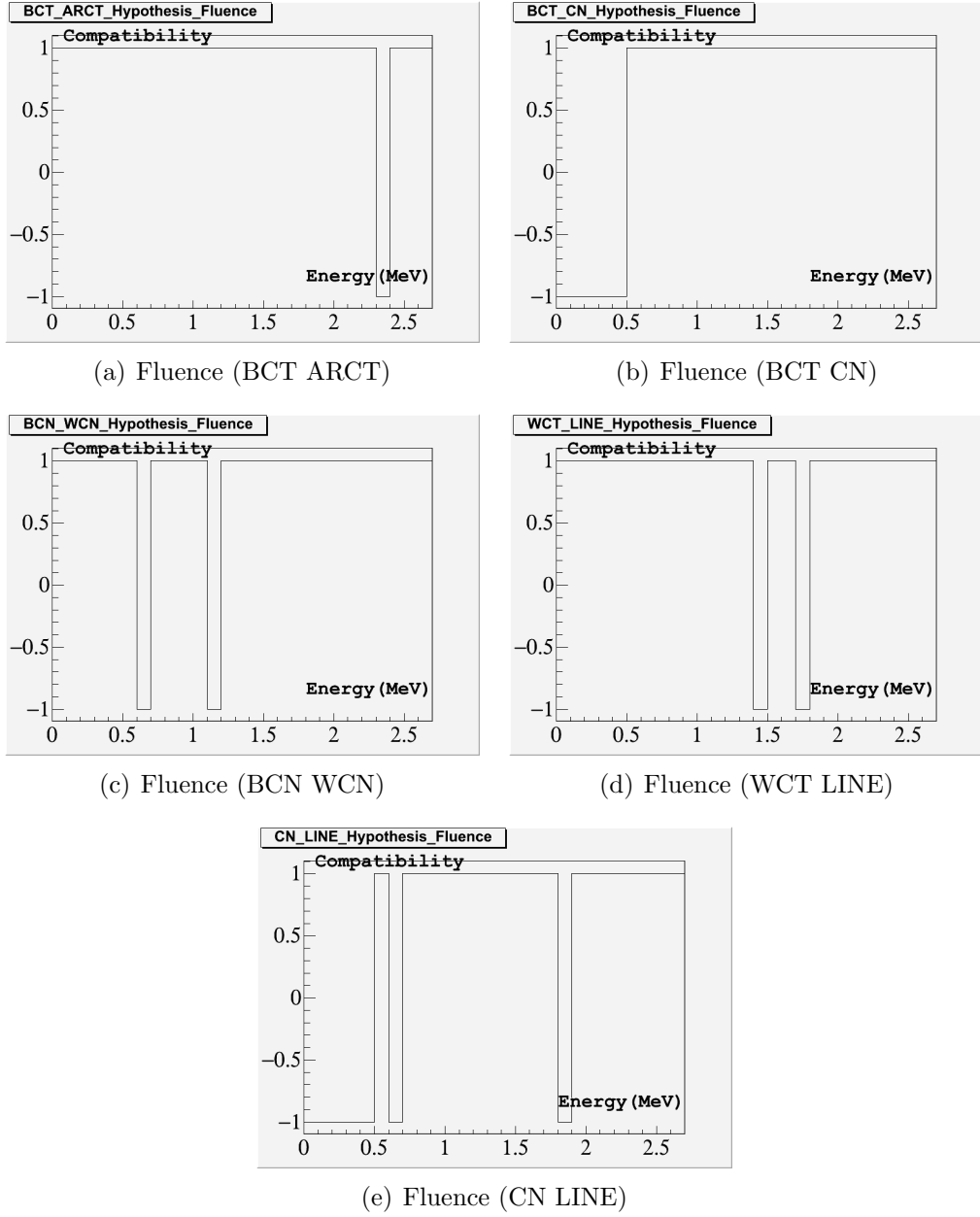


Figure 6.24: Hypothesis test for the thorium gamma fluence comparison. There are 27 bins in each plot. The flat wall (WCT) and bottom (BCT) agree in all bins, therefore their comparison plot is not included. (b) and (e) show overall non-compatibility, with incompatible region ranging from 0 to 500 keV (Although there are two incompatible bins above 500keV for (e): 700 keV and 1.8 MeV, their test statistics are all slightly below the significance level, so if changing the confidence level to 99%, both bins will show compatibility again).

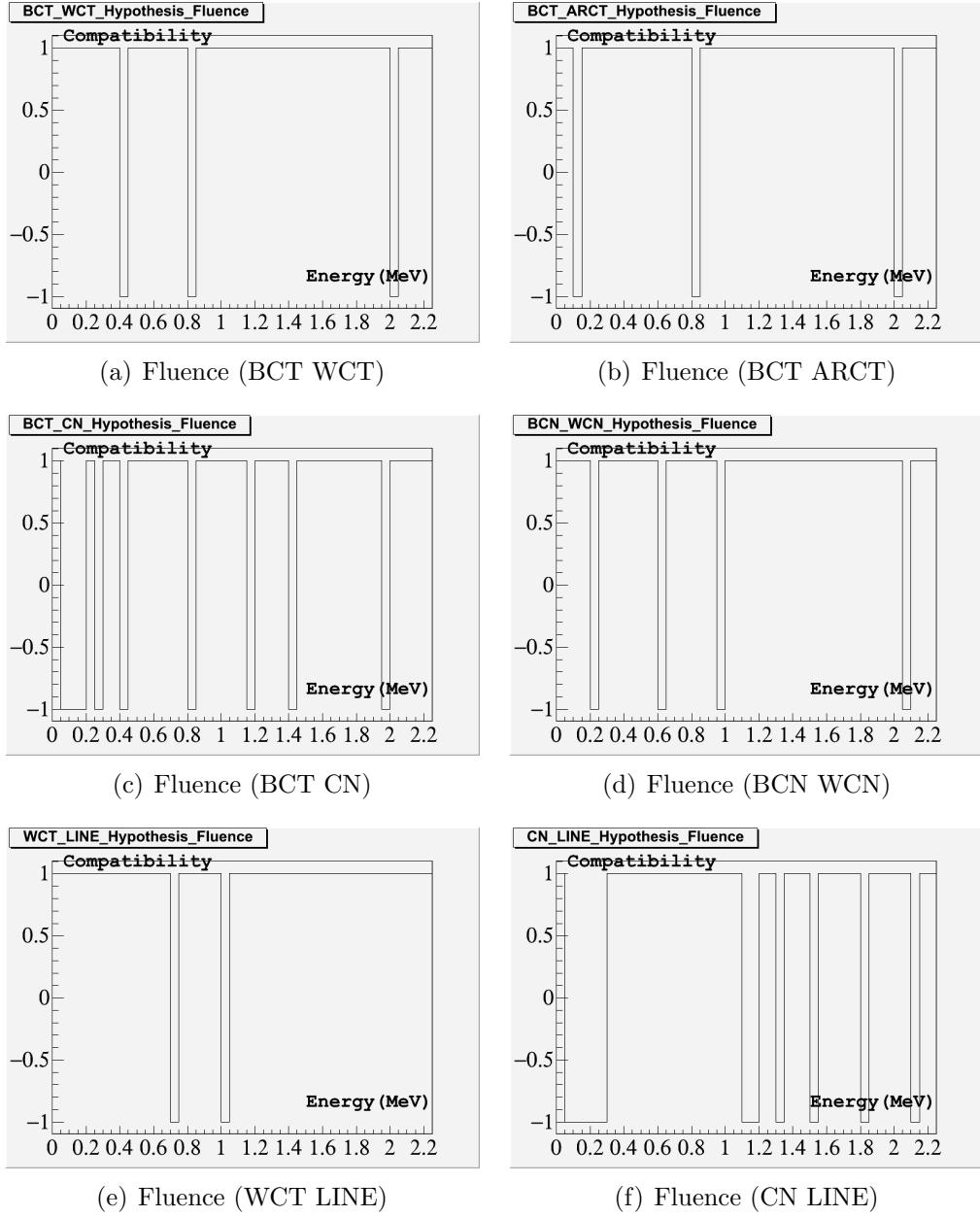


Figure 6.25: Hypothesis test for the uranium gamma fluence comparison. There are 23 bins in each plot. (c) and (f) show overall non-compatibility, with incompatible region ranging from 0 to 500 keV (Although there are two incompatible bins above 500 keV for (c): 2MeV, this is probably due to lack of statistics; 1.5MeV, its test statistic is slightly below the significance level, so if changing the confidence level to 99%, this bin will show compatibility again. The incompatible bin above 500 keV for (f) is also due to its test statistic just slightly below the significance level.)

the corners due to the higher flux in that region.

The excess of corner fluence below 500 keV is shown in Figure 6.26 for gammas from both decay chains. Based on the excess histogram, the corner excess can be calculated. The result for the thorium decay chain gammas is 586 events missed at the corner if 1 million events being started from the surface under the line source spectrum, while the number is 548 for the uranium decay chain gammas. Given a detector rate of 10 events out of every million throws for the current geometry with the water shield absent (this rate is obtained from actual simulations which is discussed below), a 500 million throws run will bring 5000 depositions and have about 300000 corner events underestimated. This underestimate will result in a loss of about 3 events as detector depositions. Since this number is way below the statistical fluctuation of 5000 detector depositions, an additional run for the corner excess is not needed.

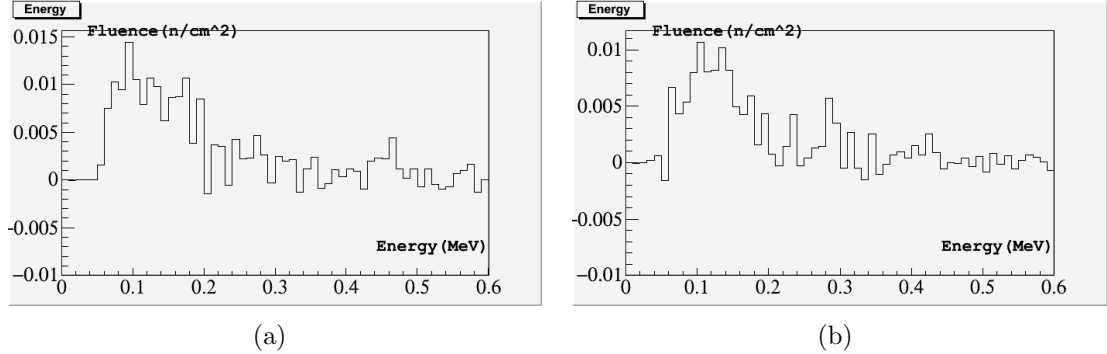


Figure 6.26: The excess of corner fluence below 500 keV for both decay chain gammas. (a) The excess for the thorium decay chain gammas. (b) The excess for the uranium decay chain gammas.

The line source spectra for both decay chains gammas as well as the  $^{40}\text{K}$  gamma which are later used as primary spectra to generate throws from the laboratory wall surface in their individual simulations are shown in Figure 6.27. The fractions of generated gammas that eventually enter the laboratory volume are 18.8%, 14.0% and

11.0% for the thorium chain, the uranium chain and the  $^{40}\text{K}$  gammas respectively. This leads to a speed up of the simulation by a factor of 5, 7 and 9 respectively if the line source spectrum is used.

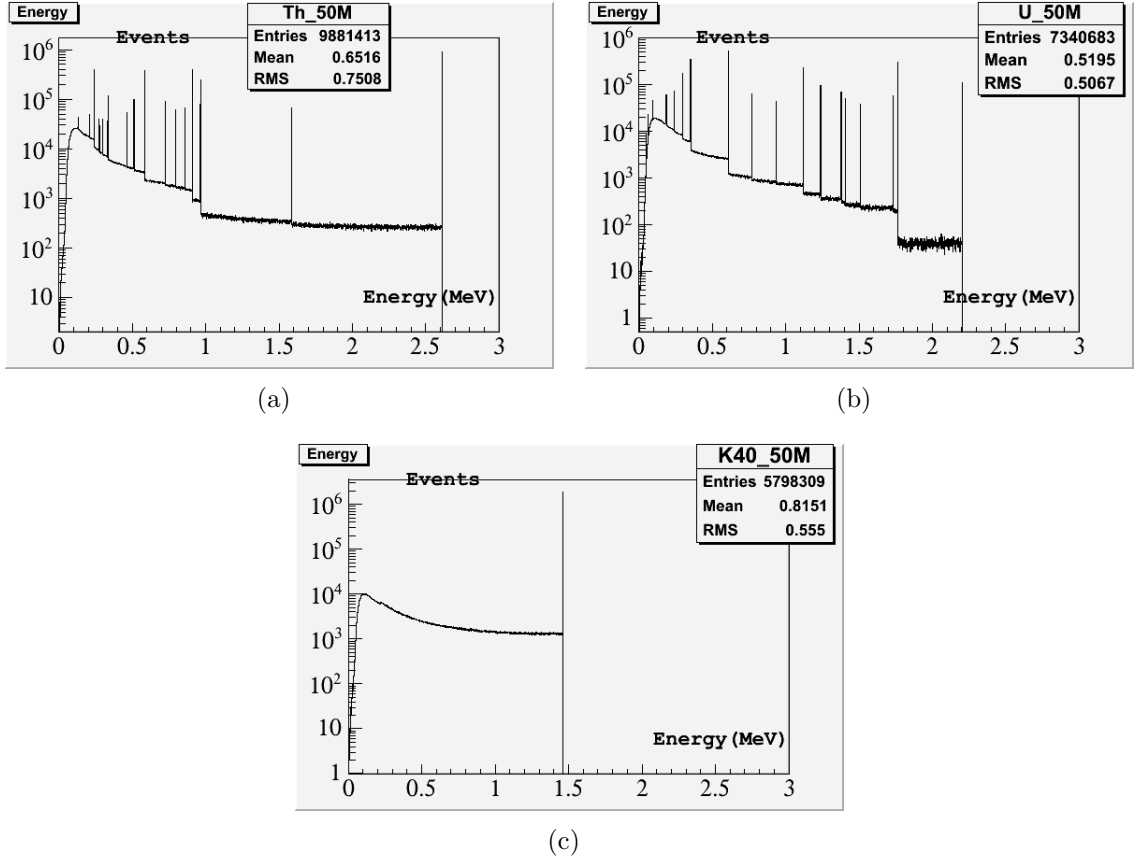


Figure 6.27: The line source gamma spectra for the thorium decay chain (a), the uranium decay chain (b), as well as  $^{40}\text{K}$  (c). The bin width is 1 keV for each plot, and 50 million events were started in each test.

**Study for the neutron background** Neutrons induced by natural radioactivity in the laboratory wall are considered in this context. The primary neutron energy spectrum is given by Figure 6.28, which is calculated by SOURCES(see section 5.2.2).

Unlike in the gamma situation, it is low energy neutrons that contribute the most to the surface spectra, where the count number is rapidly decreasing in high energy

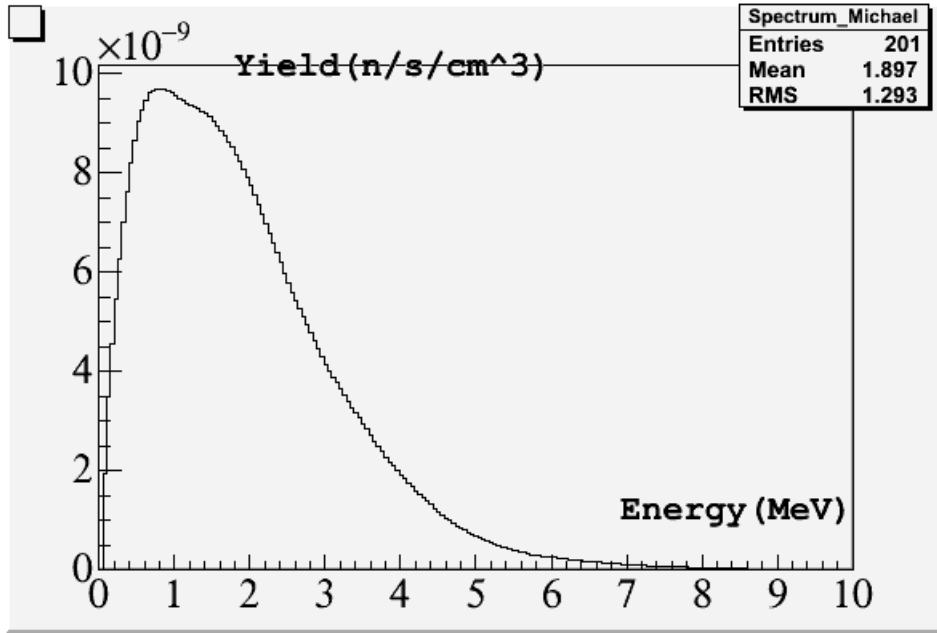


Figure 6.28: Neutron spectrum as calculated by SOURCES.

regions. The corner effect here is larger than in the gamma case, with 10% excess of corner flux on average (Figure 6.29). This relatively large difference is expected due to the diffusive nature of neutrons. Figure 6.29(f) shows a systematically higher yield of the line source spectrum over the spectrum for the flat area (WCT).

To quantify the difference in each comparison, the hypothesis test introduced in the previous section is implemented. Figure 6.30 shows the result, which exhibits an obvious corner effect and only comparison between non-corner regions shows a good compatibility. The result also indicates unlike in the gamma situation the line source spectrum is not an ideal replacement for the real neutron spectrum. Instead, the averaged surface spectrum sampled over the entire laboratory wall is used to generate the surface throws. By doing this, the corner effect is averaged out. The surface spectrum is shown in Figure 6.31. Since 20% of neutrons started inside the laboratory wall can escape from the surface, this method can speed up the simulation by a factor of 5.

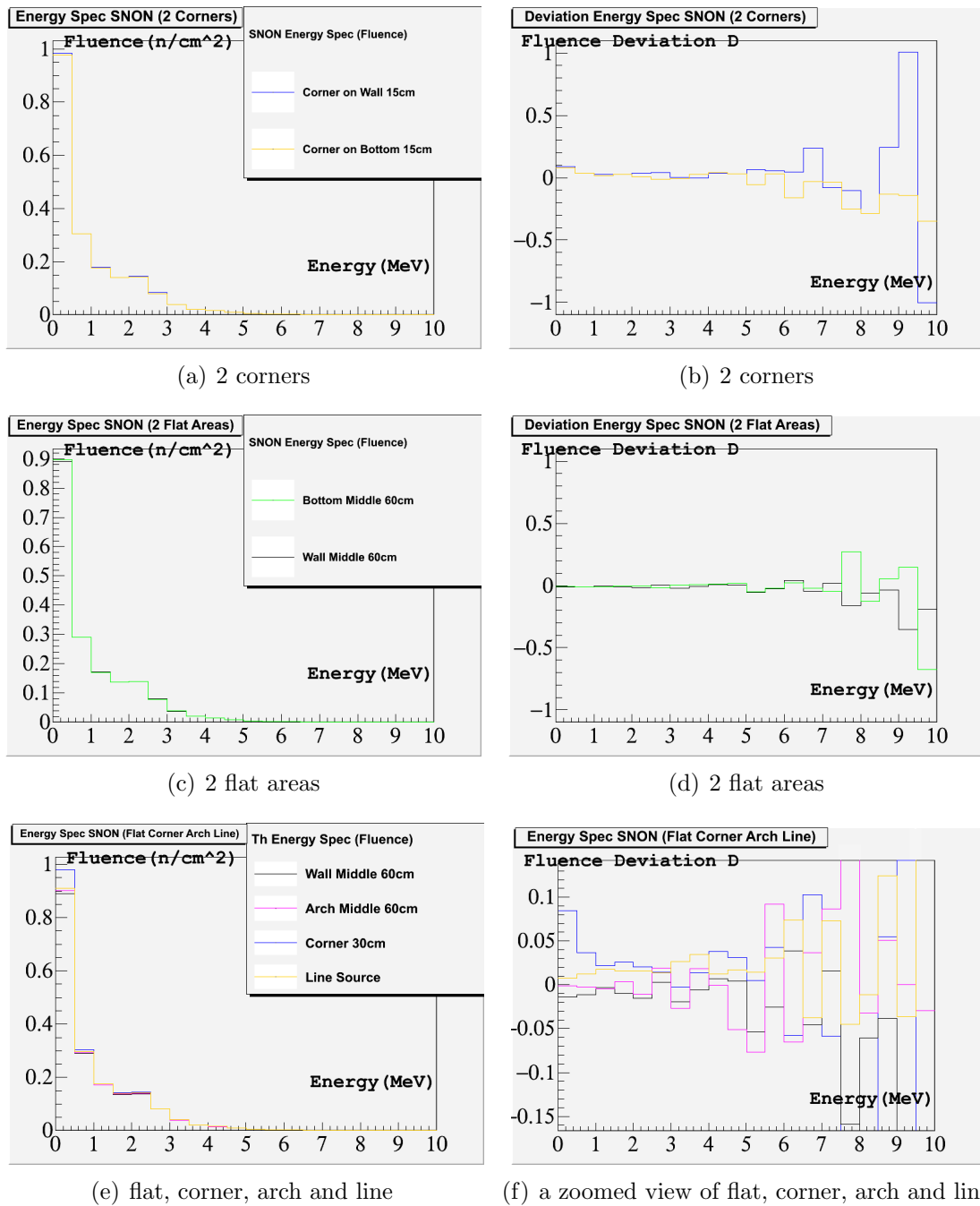


Figure 6.29: Comparison of the absolute fluence (a)(c)(e) and the deviations (b)(d)(f) of the background neutrons from different regions. (f) is a zoomed view of the comparison, which shows a systematically higher yield of the line source spectrum over the spectrum for the flat area (WCT).

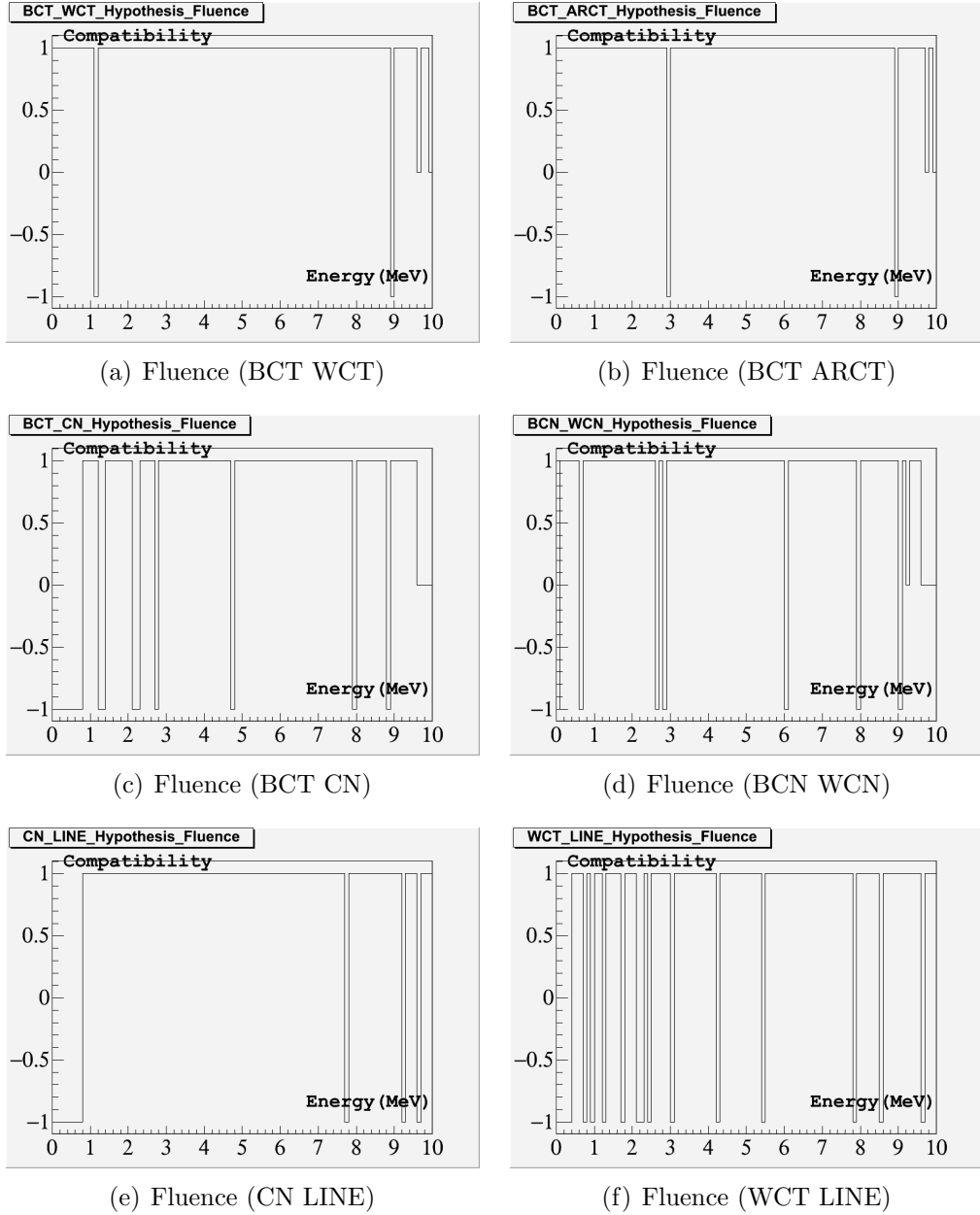
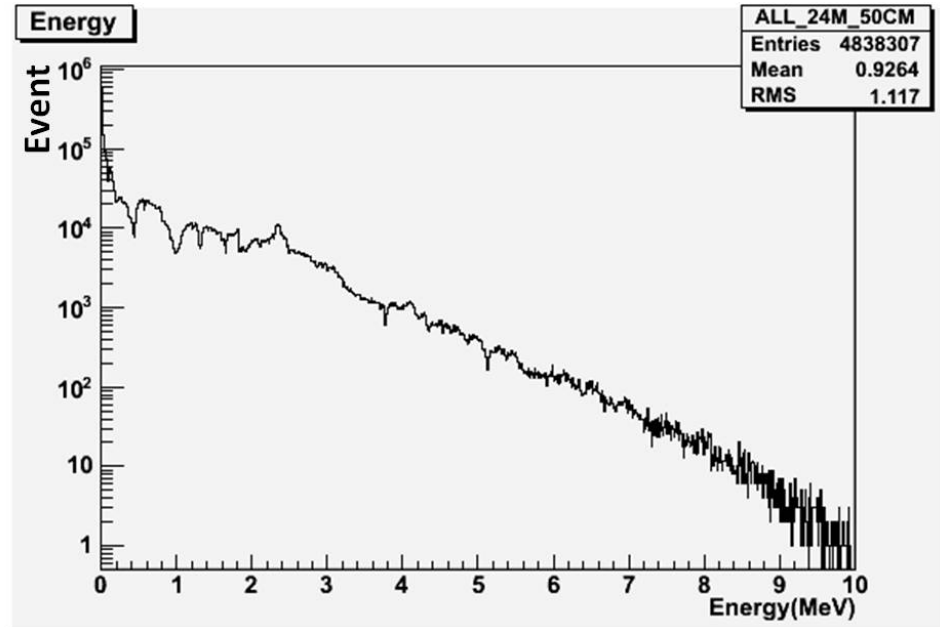


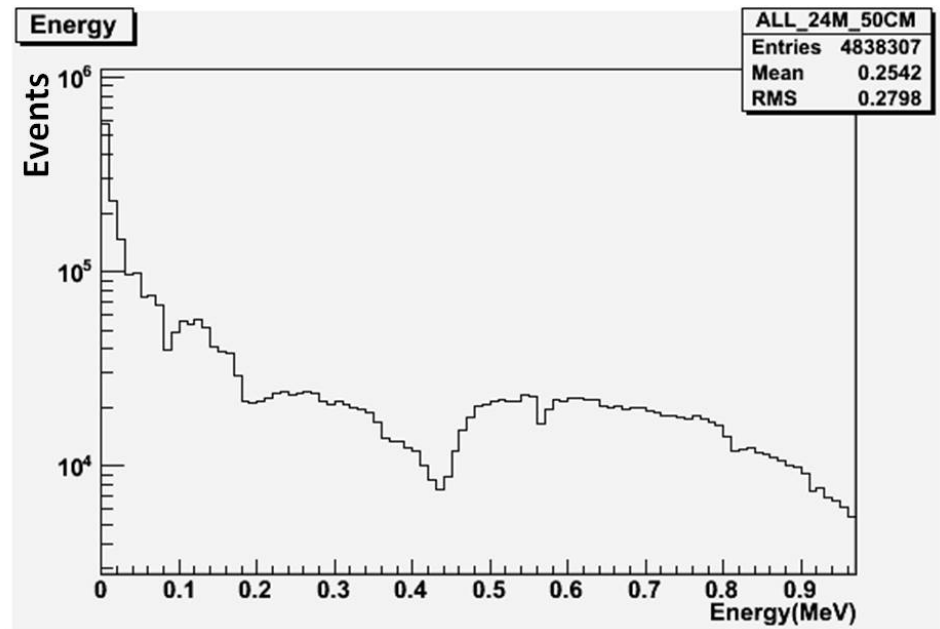
Figure 6.30: Hypothesis test for the neutron fluence comparison. There are 100 bins in each plot. Only comparison between non-corner regions shows good compatibility.

### 6.2.3 Results

Three detectors are placed inside the new geometry, which effectively increase the total exposure and also allow us to study of multiple scattering between nearby detec-



(a) Full range



(b) Below 1 MeV

Figure 6.31: The neutron surface spectrum.

tors which is especially important for the neutron background study. To speed up the process, we use the surface spectra discussed in the previous section to simulate the

background radiation originating in the laboratory wall. But the wall is kept as thick as it was when we generated the surface spectra (i.e. 40 cm for gammas and 50 cm for neutrons) in all the simulations. Since simulations for radiation from the water tank consume less computing time, they are done naturally with the straightforward volume source.

### Neutron from the laboratory wall

With the use of the surface spectrum (Figure 6.31), 199 million neutrons are initiated from the laboratory wall surface, which is equivalent to about 1 billion events started from inside the wall.

The detector depositions are shown in Figure 6.32, where we only plot the nuclear recoils below 100 keV. The full set of depositions are listed in Table 6.32. It is observed that deposition is most concentrated in DT01 or the top detector, while the middle detector (DT02) records the least number of depositions, which is probably due to the weak shielding from upward and the middle detector is partially shielded by the other two detectors. However, due the relative long mean free path of MeV neutrons in Ge, the difference is not very strong.

Table 6.6: Energy depositions from the neutron background simulation. The whole data set is divided into four energy bins, and classified into three categories: ER → electron recoil; NR → nuclear recoil; Mixed → ER and NR observed concurrently in one event in one detector. Det. means an individual detector (DT01, DT02 or DT03).  $\Sigma$  means the sum of all three detectors.

Energy	< 1 keV			1-10 keV			10-100 keV			> 100 keV			total			
	1	2	3	1	2	3	1	2	3	1	2	3	1	2	3	$\Sigma$
Det.	1	2	3	1	2	3	1	2	3	1	2	3	1	2	3	$\Sigma$
Mixed	0	0	0	0	0	0	1	1	0	2	0	0	3	1	0	4
ER	0	0	0	0	0	0	1	0	0	3	1	4	4	1	4	9
NR	20	14	17	15	19	14	12	6	10	1	0	0	48	39	41	128

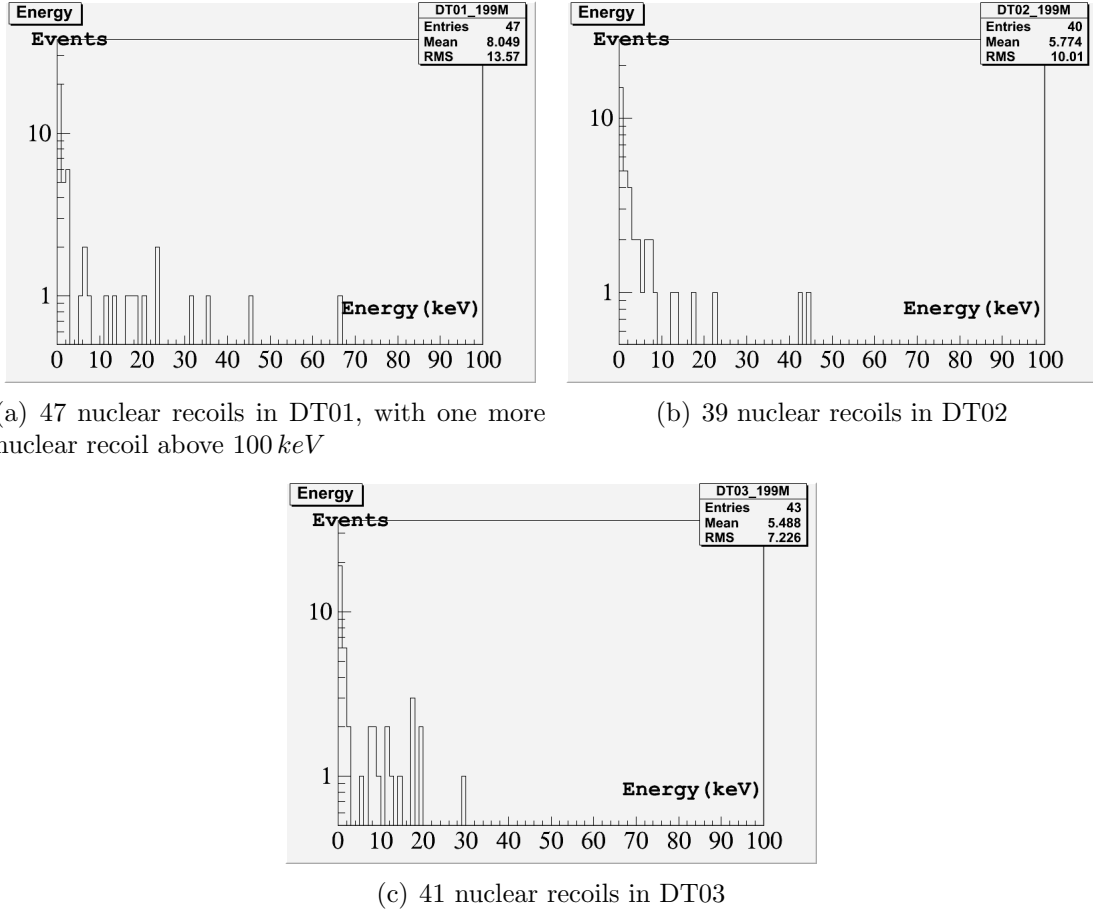


Figure 6.32: Nuclear recoils from background neutrons in three detectors.

According to the neutron production rate calculated from SOURCES, the neutron yield is about 6.7 million per day from the current geometry. So 199 million events from the surface are equivalent to 149 days of measurement time, which then gives the detector rate of  $0.08 / \text{day}$  (DT01; 12 events),  $0.04 / \text{day}$  (DT02; 6 events),  $0.07 / \text{day}$  (DT03; 10 events) for nuclear recoils in the  $10\text{-}100 \text{ keV}$  range for each of the detectors (as this is the typical WIMP search region). These detector rates are all significantly lower than the result from the preliminary simulation, which is  $0.32/\text{detector/day}$  if the same range of interest is applied. This could be seen as a result of the application of the much softer initial neutron spectrum, as well as the presence of the cryostat

and an increased distance between the setup and the laboratory wall in the detailed geometry.

As a comparison, a supplementary simulation is run without the water shield, which shows a detector rate (with all the depositions obtained in the simulation) of 88 /day (DT01; 660 events), 86 /day (DT02; 644 events), 87 /day (DT03; 655 events) correspondingly (Figure 6.33).

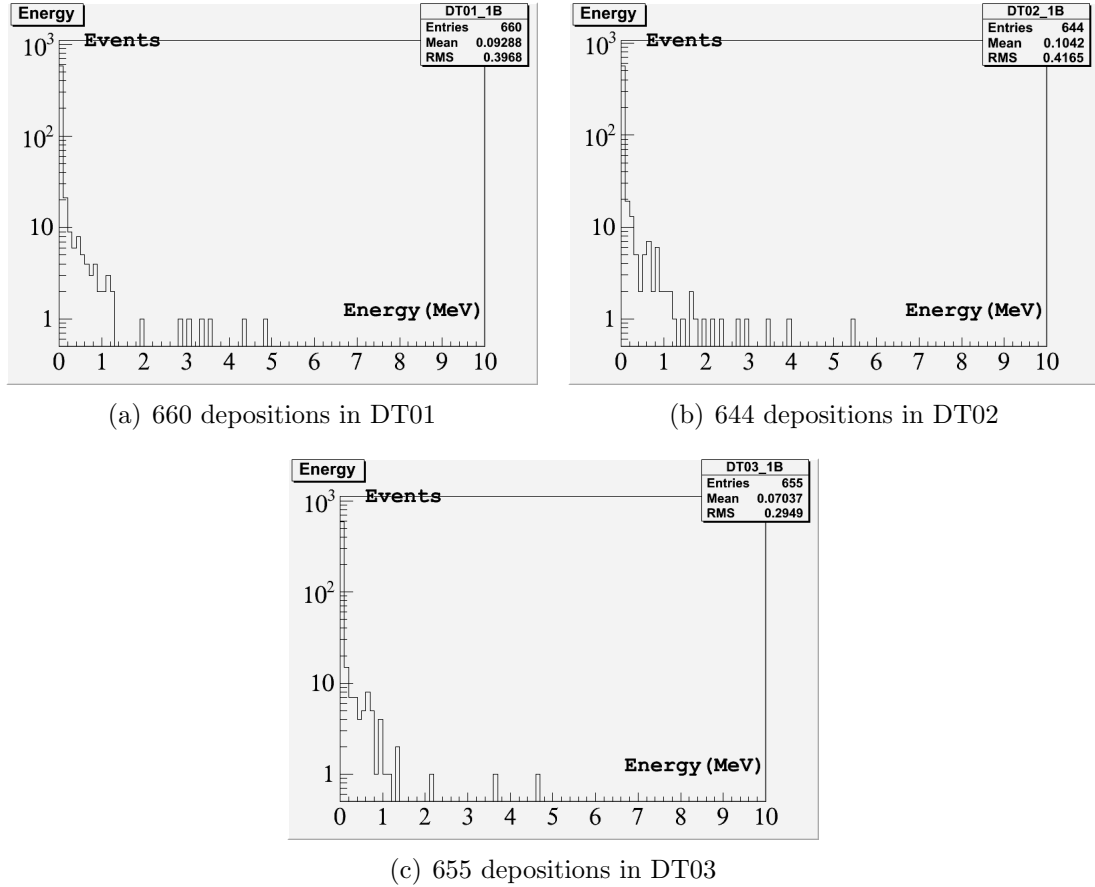


Figure 6.33: Energy deposition from background neutrons in three detectors when the water shield is removed.

The 2% correction from the reflection study (section 6.1.2) is not applied to this analysis, because the 2% is much less than the statistical fluctuation.

Multiple scattering in two or three detectors is also studied. The coincidence between two detectors is plotted in Figure 6.34, where more than 25% of the depositions in each detector are accompanied by a coincidence in another detector. The frequent occurrence of multiple scattering is expected, for it is one of the signatures that could distinguish the background neutron from the single scattered WIMP signal. Therefore, the multiple scattering events are extracted and listed in Table 6.7, where mixed recoil indicates the electron recoil and nuclei recoil are observed concurrently in one event but in multiple detectors.

Table 6.7: Multiple scattering from the neutron background simulation. The whole data set is divided into three energy bins.

Energy		< 1 keV	1-100 keV	> 100 keV	total
Multiple scatters		7	20	3	30
Double coincidence	Mixed	0	0	2	2
	ER	0	0	1	1
	NR	6	17	0	23
Triple coincidence	Mixed	0	0	0	0
	ER	0	0	0	0
	NR	1	3	0	4

Besides the detector rate, the information of the throws that eventually contribute to the detector depositions in the form of nuclear recoils is also collected. The position distribution of those throws are shown in Figure 6.35, where a red cross represents a primary vertex whose daughter “directly” enters the detectors without being translated on the boundary (section 6.2.1), while a blue diamond represents those who “indirectly” enter the detectors after translation on the boundary. The green circle shows where those translations take place at both ends of the tunnel. For all the three types of vertices, they are more concentrated on the top half of the geometry, which can be explained with the absence of the water shield from the top.

To better understand the distribution, especially the distribution of the “direct”

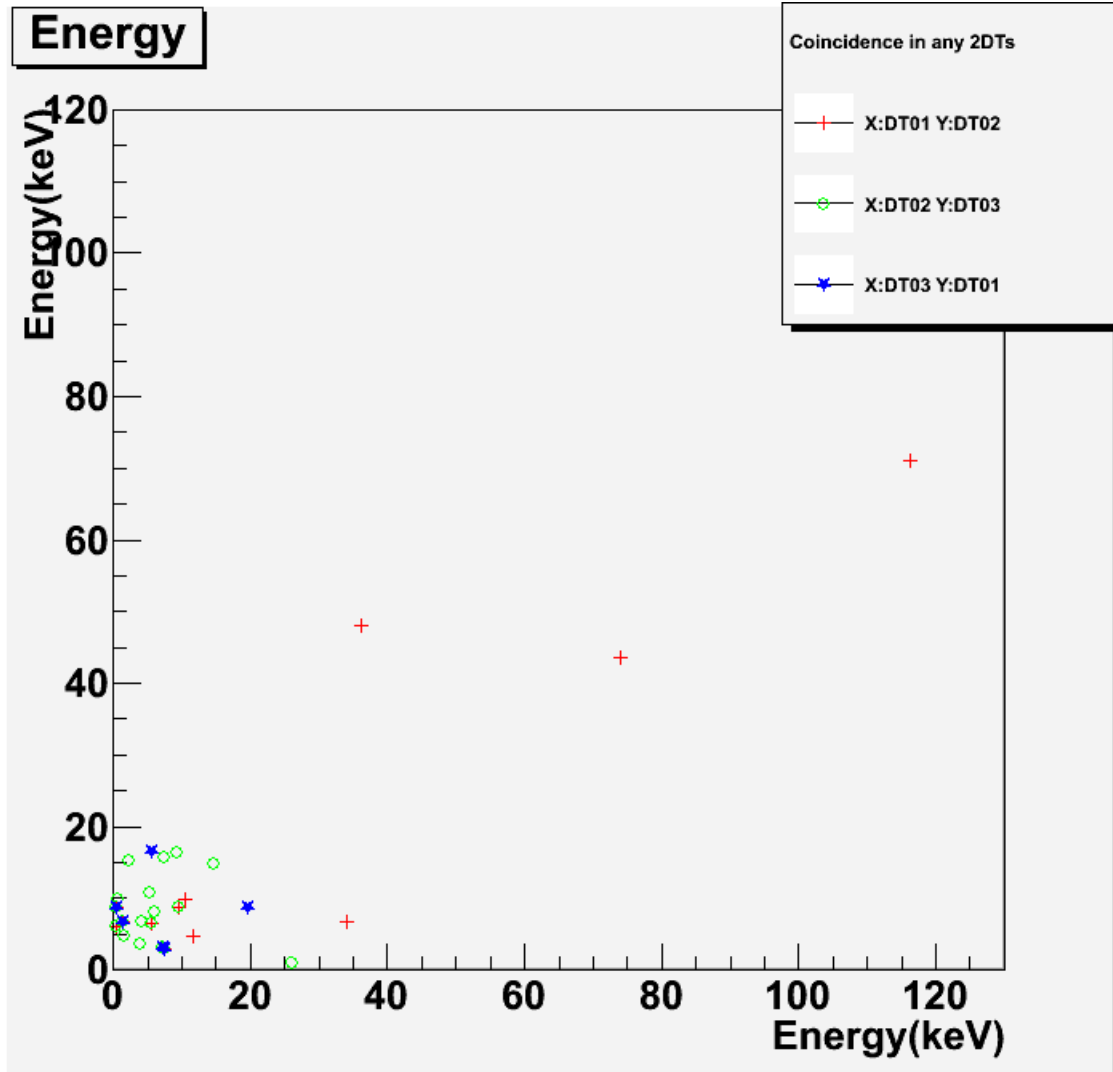
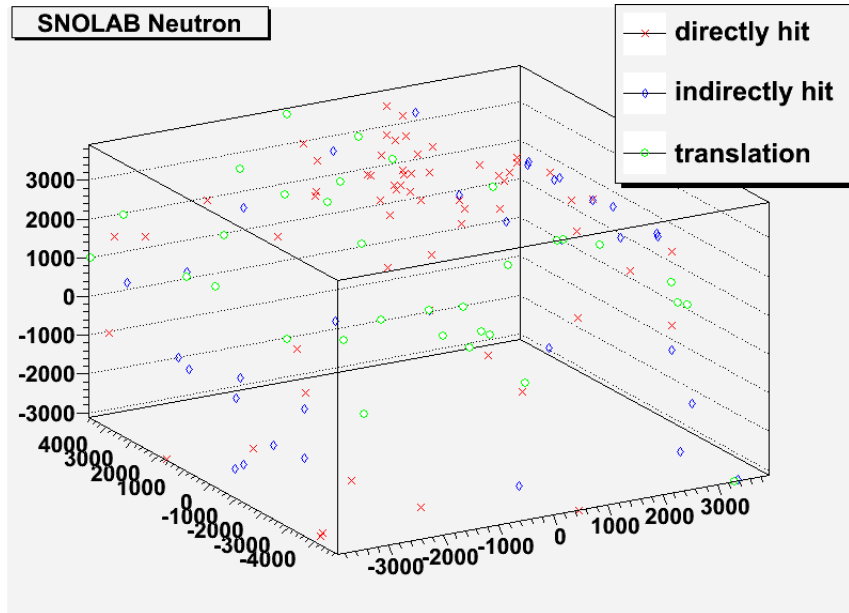


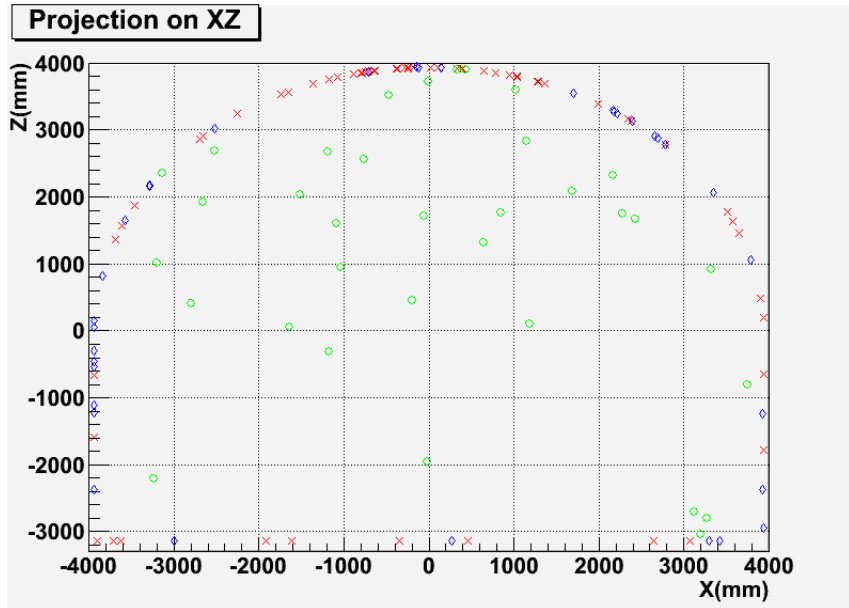
Figure 6.34: Coincidence between two detectors in the background neutron simulation. Coincidence with energy greater than  $120\text{ keV}$  is not plotted. For DT01 and DT02, the coincidence number is 14; for DT02 and DT03, the number is 18; for DT01 and DT03, the number is 6.

and “indirect” hit vertices, the entire laboratory wall surface is divided into three regions: top, bottom and side wall. The distribution for each region can be presented on a 2D plot, which is then free from interference of data points from other regions (Figure 6.36).

To plot the vertex distribution of the top region in a 2D form, which is actually



(a) 3D View



(b) Projection into the X-Z plane

Figure 6.35: Initial position distribution of the detected background neutrons. Red cross: a primary vertex whose daughter “directly” enters the detectors without being translated on the boundary; blue diamond: those who “indirectly” enter the detectors after translation on the boundary; green circle: the place where those translations take place at both ends of the tunnel.

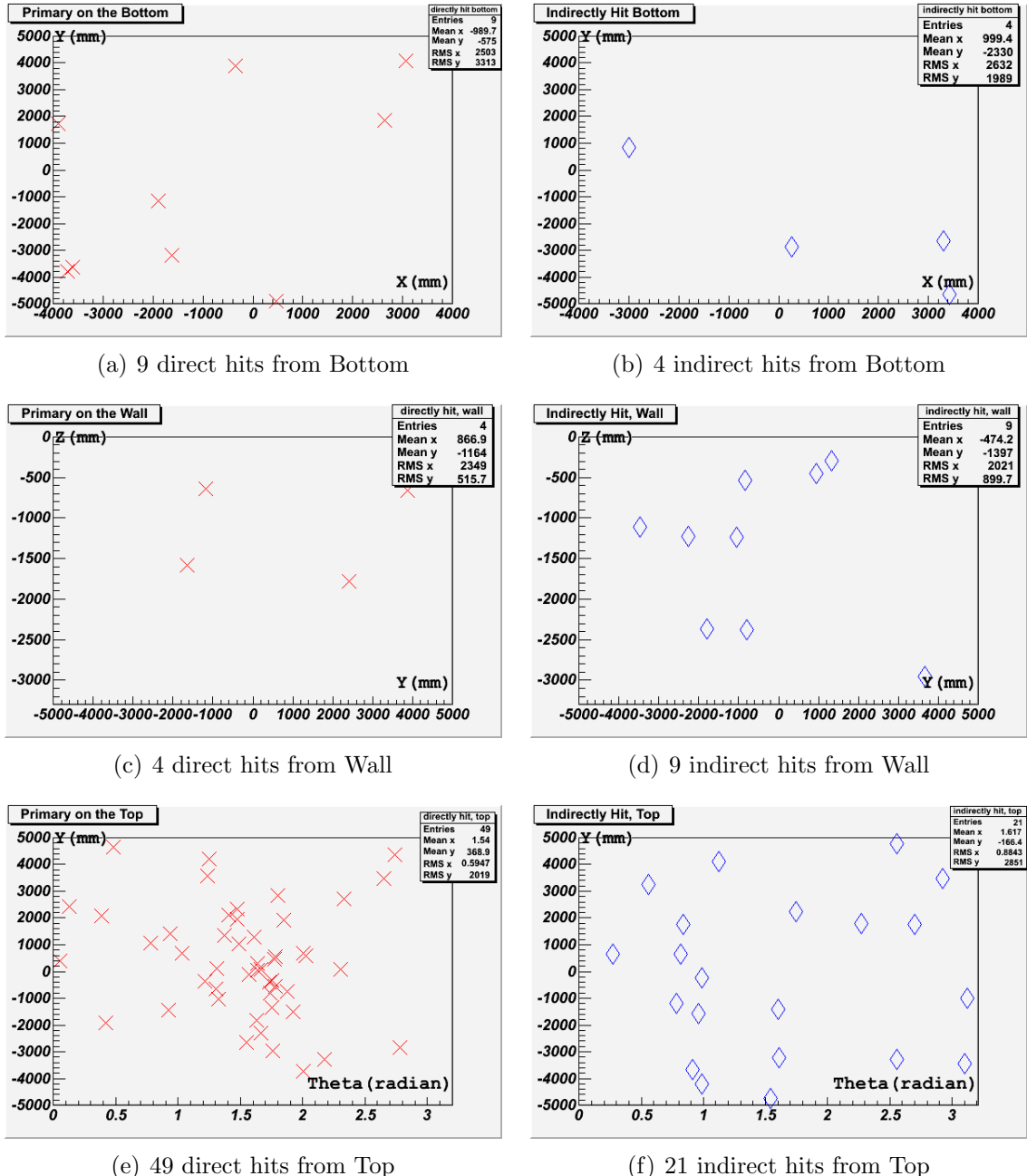


Figure 6.36: 2D view of the initial background neutron (the one that results in nuclear recoils in the detectors) position distribution in the selected regions.

an arch, the X and Z coordinates of each point are converted into the corresponding angle ( $\theta = \arctg \frac{Z}{X}$ ), which is then made as the new “X” coordinate as appears on the 2D plot. Except for Figure 6.36(e), which shows a concentrated distribution near the

center, other plots all exhibit an even distribution within the given low statistics.

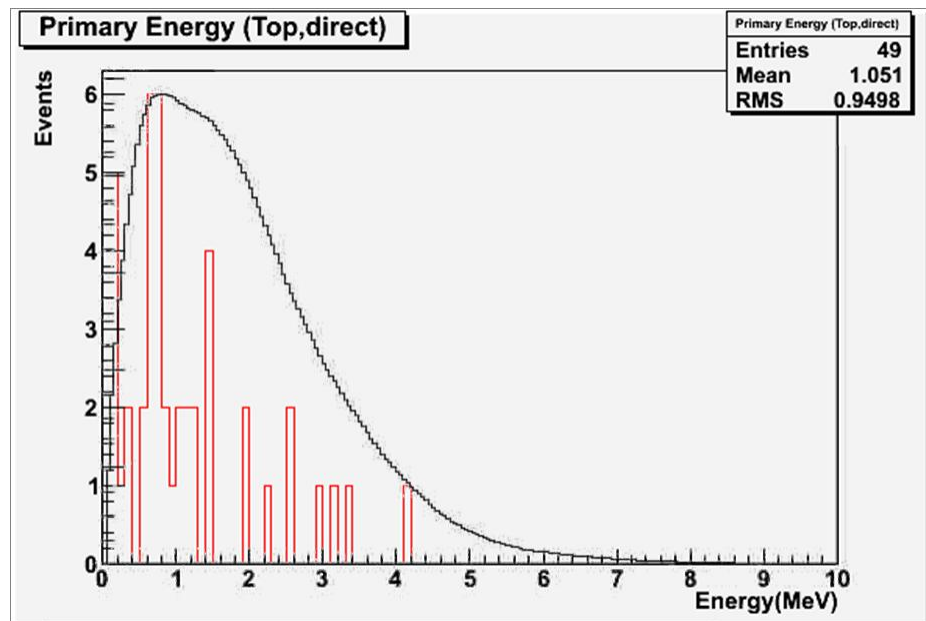
Besides the position distribution, the energy distribution of these primary throws is also extracted from the simulation, which is shown in Figure 6.37. Two energy spectra are plotted. The “Top” region with “directly” hit events is separated from the rest because it has no water shield in that direction, so the energy distribution is expected to be different. Both spectra exhibit a resemblance with the primary neutron spectrum. But the peak is missing in Figure 6.37(b), while the peak is observable in Figure 6.37(a). This is probably due to the absence of water shield which makes the neutron energy distribution less disturbed. In any cases, the spectra are cut off at around  $4\text{ MeV}$ , which is near the energy where the flux from the primary neutron spectrum has dropped by one order of magnitude from its peak value.

### Gamma from the laboratory wall

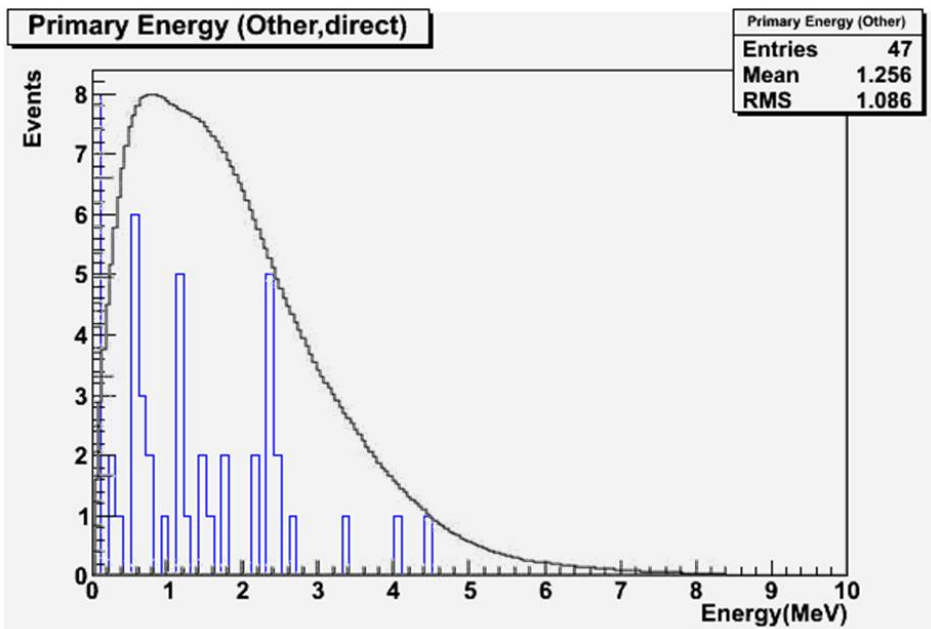
Due to the complexity and the increased dimension of the new geometry, the detailed gamma simulation requires much greater sample size in order to get a similar statistics as the preliminary one. Therefore, the surface spectrum (Figure 6.27) was used to generate throws from the laboratory wall surface for each type of background gamma source. Both the thorium and uranium decay chain gammas and  $^{40}\text{K}$  gammas are considered here.

Due to the similarity of results from all three gamma sources, if not specifically stated, only the plots from thorium decay chain gammas are shown in this section.

The detector depositions for the thorium decay chain gammas are shown in Figure 6.38, which shows significantly more depositions in the top detector. Unlike neutrons, gammas lose energy rapidly through interactions, which makes them less diffusive during the transportation. Therefore the much greater gamma flux from



(a) Top region; directly hit events



(b) Other regions

Figure 6.37: Energy distribution of the initial background neutrons in the selected regions. They are superimposed with the primary neutron spectrum (see Figure 6.28), where closer resemblance is observed for (a).

the top due to lack of shielding from that direction are largely blocked by the top detector. Since there is no excess gamma flux from the bottom, the top detector can be used to represent the one detector setup.

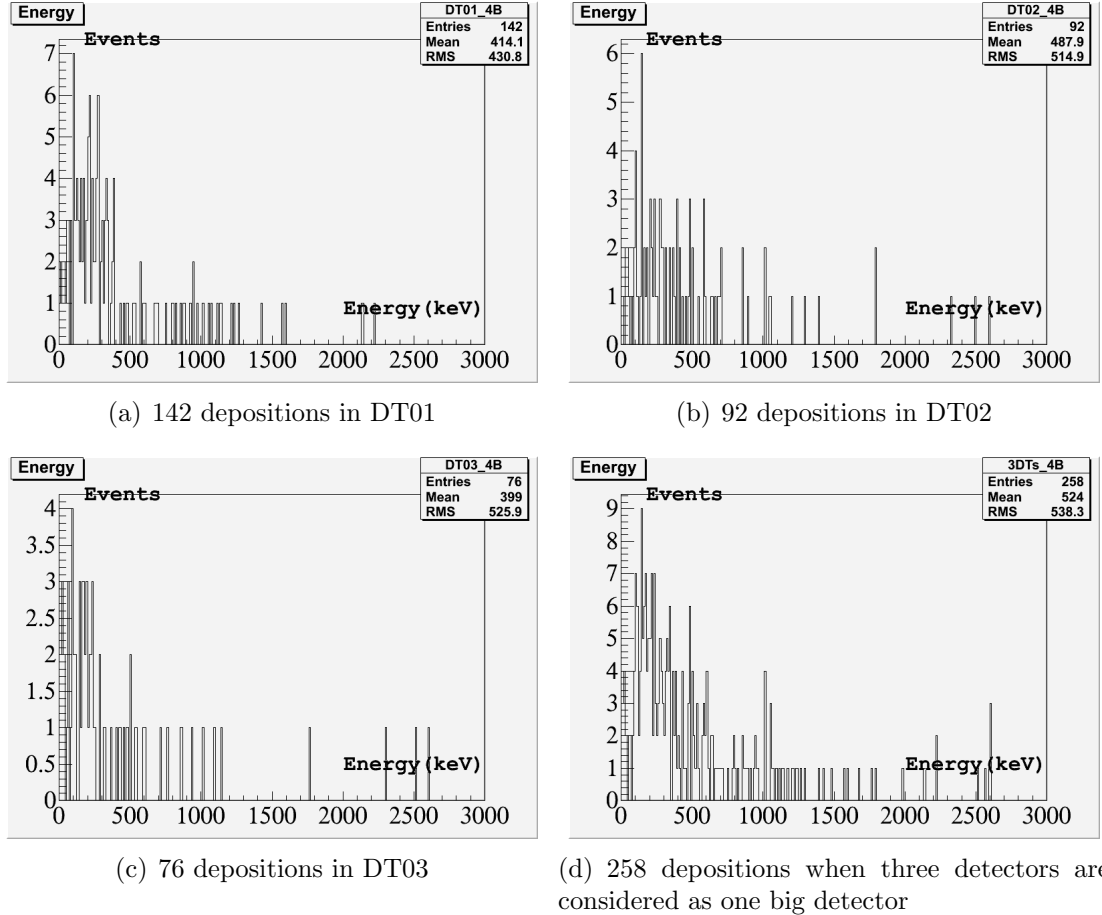


Figure 6.38: Energy deposition from the laboratory wall thorium decay chain gammas. 4 billion throws are generated from the surface in the simulation.

To relate the detector depositions to the detector rate, the decay rate is calculated for each of the gamma sources:

$$D_\gamma = \frac{\ln(2)}{T_{\frac{1}{2}}} \times \frac{\rho V}{A} N_A \times C \quad (6.2)$$

where  $T_{\frac{1}{2}}$  is the half life, A is the atomic weight and C is the contamination level

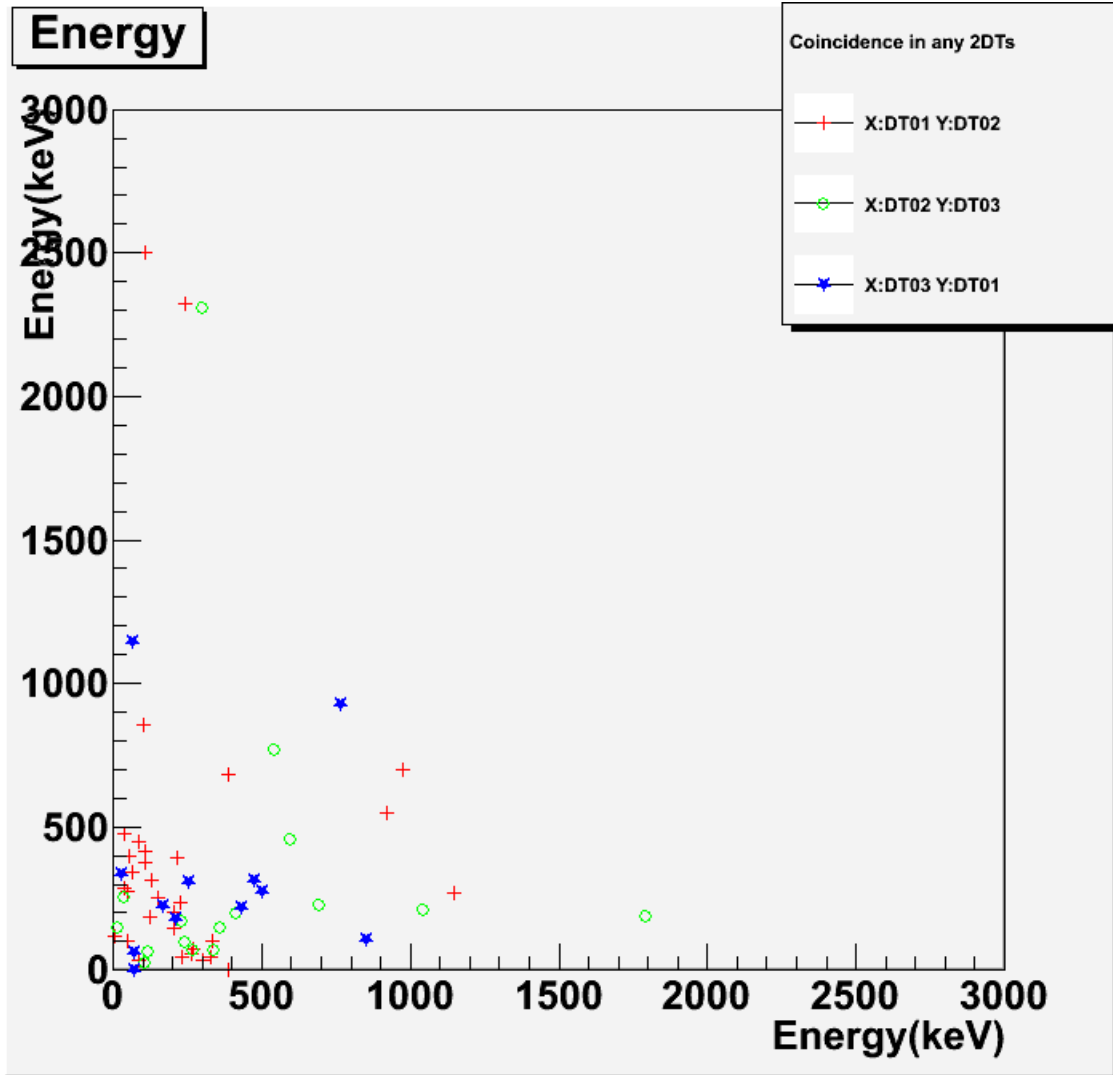


Figure 6.39: Coincidence between two detectors in the the thorium decay chain gamma simulation.

of each gamma source in the volume;  $\rho$  is the density of norite rock ( $2.87\text{ g}/\text{cm}^3$ );  $V$  is the volume of the laboratory wall in the current geometry ( $117\text{ m}^3$ ).

For  $^{40}\text{K}$ , we need to consider the branching ratio to get the gamma production rate. This is because in the thorium/uranium decay chain gamma simulations each event is corresponding to one decay, while in the  $^{40}\text{K}$  gamma simulation each event is representing the emission of one gamma. The calculated rate for each radioactive source is listed in Table 6.8, from which the detector rates can be calculated and are

listed in Table 6.9.

Table 6.8: The calculated gamma rate/decay rate for all three radioactive sources. For thorium and uranium, the decay rate is used to interpret the simulation result, while for  $^{40}\text{K}$  the gamma production rate is used.

Source		Concentration	Rate	
Thorium		5.56 ppm	$2.6 \times 10^{10} / \text{hour}$	
Uranium	U <sup>235</sup>	1.12 ppm	7.3 × 10 <sup>8</sup> /hour	$1.7 \times 10^{10} / \text{hour}$
	U <sup>238</sup>		$1.6 \times 10^{10} / \text{hour}$	
Potassium		1.15 ppm	$3.8 \times 10^{10} / \text{hour}$	

Table 6.9: Detector rates in all three laboratory wall gamma simulations.

Source	Sample size	Equivalent time	Detector No.	Detector rate
Thorium	4 billion	49.11 min	1	2.89 /min
			2	1.87 /min
			3	1.55 /min
Uranium	4 billion	101.22 min	1	1.12 /min
			2	0.66 /min
			3	0.57 /min
Potassium	1.5 billion	21.49 min	1	2.93 /min
			2	1.77 /min
			3	1.30 /min

For the thorium and uranium decay chain gammas, supplementary simulations were run without the presence of the water shield, the results from which are listed in Table 6.10. Through comparison of the two sets of simulations, especially the detector rates of the top detector, it can be observed that the water shield can reduce the gamma interaction rate by a factor of roughly 150.

Besides the detector rates, the vertex distribution is also studied. Under the same convention as used in the neutron analysis, the distributions of the initial vertices of the detected gammas are shown in Figure 6.40. It is fairly obvious that the majority

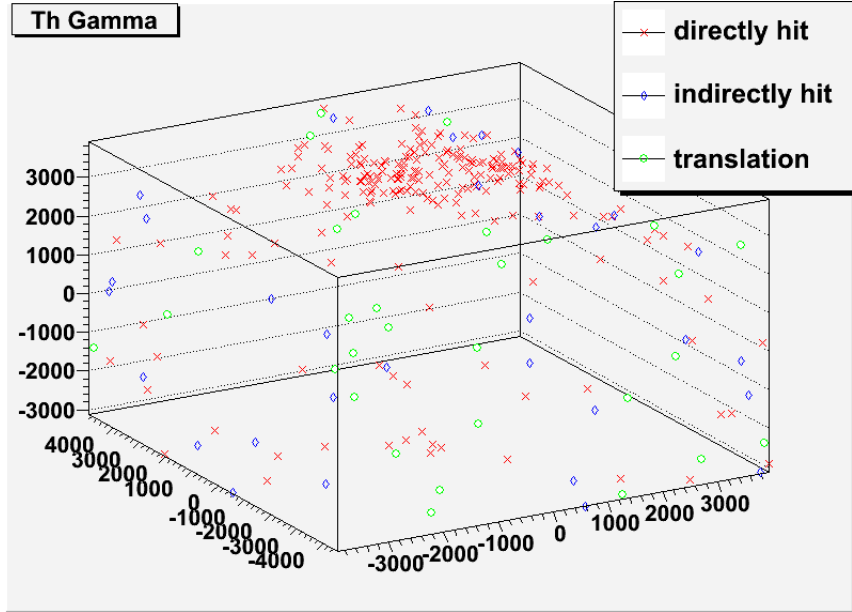
Table 6.10: Detector rates in all three laboratory wall gamma simulations.

Source	Sample size	Equivalent time	Detector No.	Detector rate
Thorium	500 million	6.13 <i>min</i>	1	6.5 <i>Hz</i>
			2	5.8 <i>Hz</i>
			3	6.5 <i>Hz</i>
Uranium	500 million	13.45 <i>min</i>	1	2.8 <i>Hz</i>
			2	2.6 <i>Hz</i>
			3	2.9 <i>Hz</i>

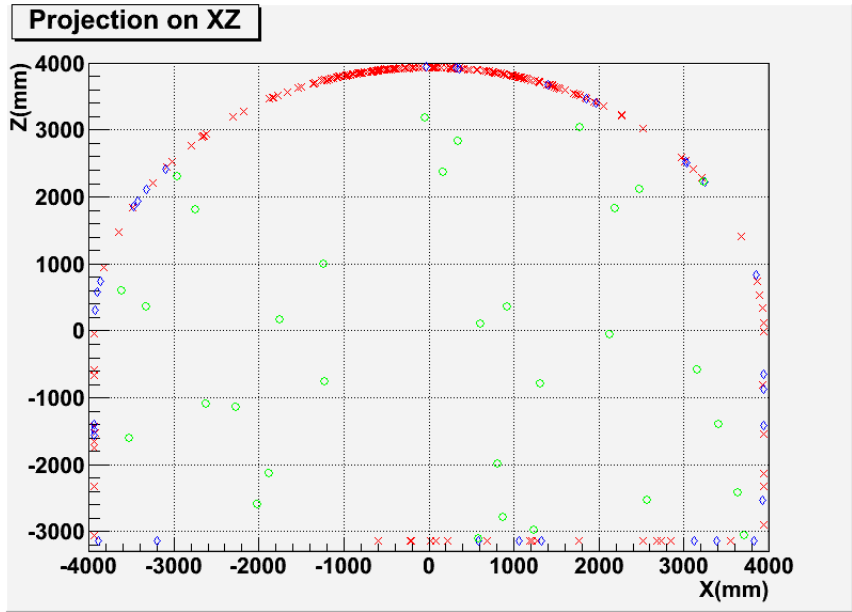
of the depositions are contributed by gamma flux from the top, where the water shield is absent. This trend can be better seen from the 2D plots in Figure 6.41 where 86.3% of the entire “direct” hits are coming from the top arch region for the thorium gammas. This percentage is 92.2% and 94.2% for uranium and potassium gammas respectively. The “indirect” hits are not counted in this calculation, because they are effectively representing particles coming from outside the current geometry.

Including the extremely dense top region, all the defined regions are prone to symmetrical and even distributions except for one specific case, which is shown in Figure 6.41(a), where there are 9 events beyond 1 *m* but no events in the same range on the other side of the axis. This is highly unexpected, because the setup is symmetrical about both X and Y axes. A symmetrical distribution would be expected in the X-Y plane.

We want to check if this is a problem of the code or just a large statistical fluctuation. So we firstly run a simulation of 500 million events from the questionable region and found 2 depositions. The rate was still low but not zero, so at least there was no error that completely prohibits the interactions. Then we were thinking of getting higher statistics with a quick test, so we removed the water shield. The deposited events were found homogeneously distributed on the bottom (Figure 6.42(a) with 459 events from  $< -1 \text{ m}$  and 468 events from  $> 1 \text{ m}$ ). Everything seemed fine without



(a) 3D view (thorium gammas)



(b) Projection into the X-Z plane (thorium gammas)

Figure 6.40: Initial position distributions of the detected thorium gammas.

the water shield. Finally we run a test to see if the presence of the water shield might create the problem. Therefore we put the water shield back but with low density water ( $0.01\text{ g}/\text{cm}^3$ ) to get higher statistics. The result was again showing homoge-

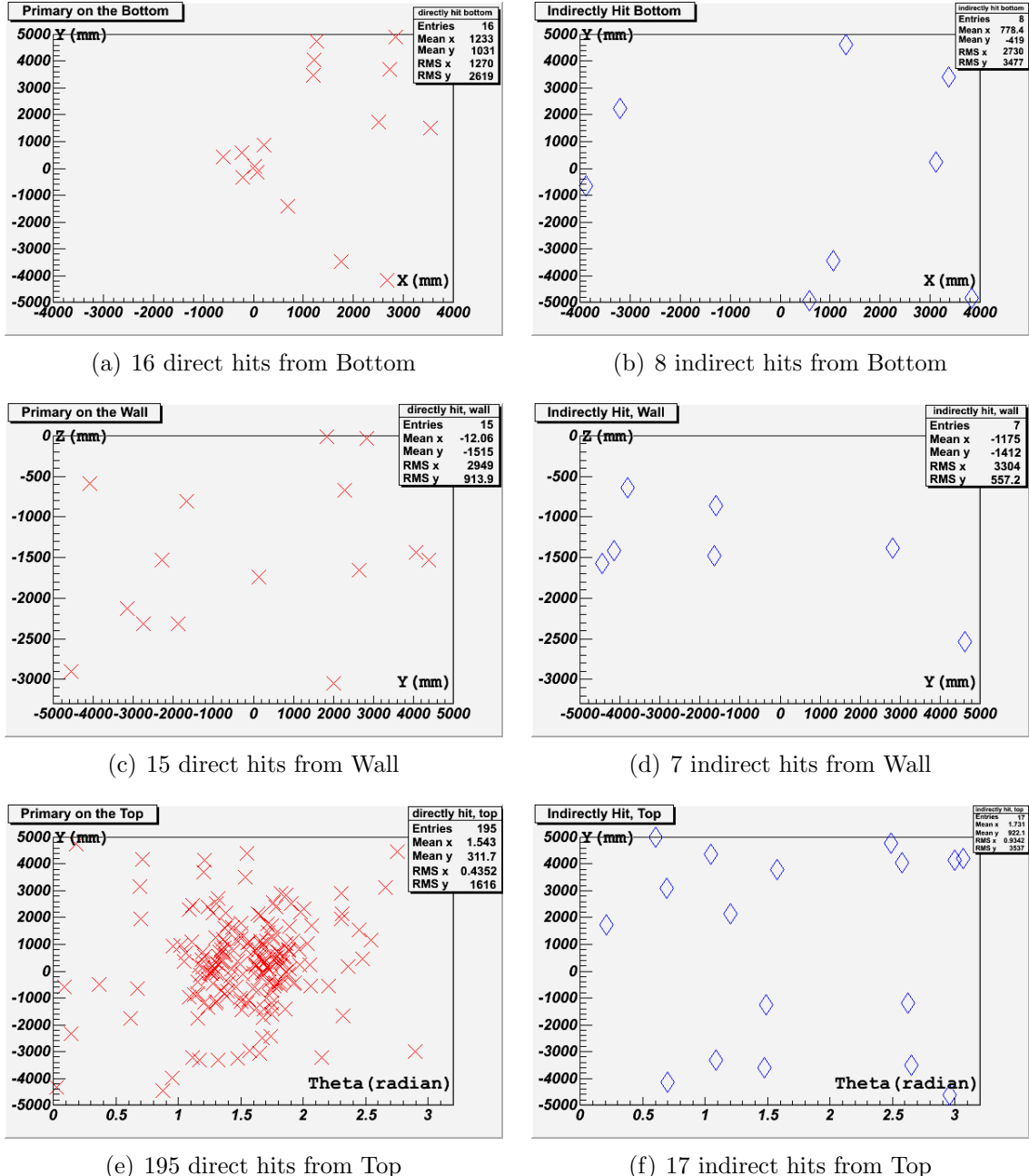
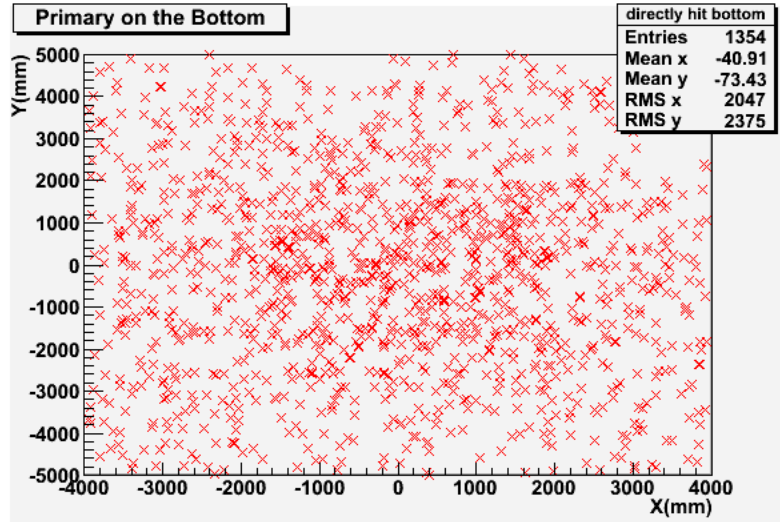
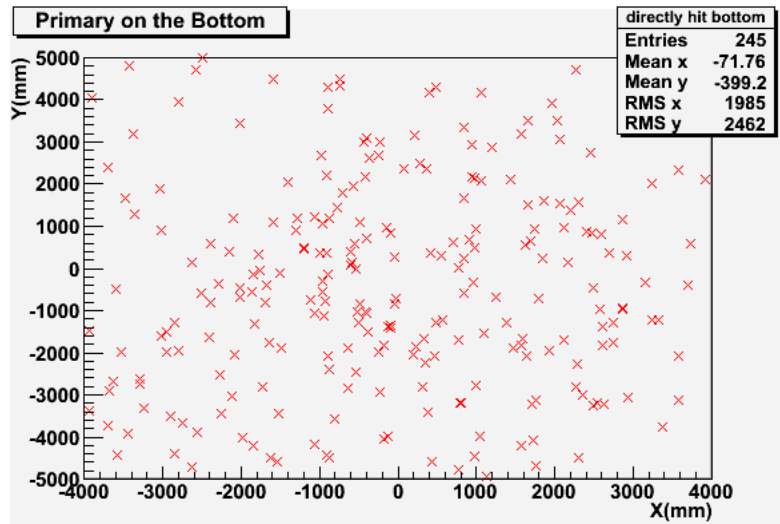


Figure 6.41: 2D view of the initial position distribution for the thorium gammas in the selected regions.

neous distribution on the bottom (Figure 6.42(b) with 76 events from  $< -1\text{ m}$  and 76 events from  $> 1\text{ m}$ ). Thus we came to the conclusion that there was no obvious problem with the code.



(a) Without the water shield



(b) With low density water ( $0.01\text{g}/\text{cm}^3$ )

Figure 6.42: The bottom region vertex distribution of the detected thorium gammas from different simulations.

The reason then may be statistical fluctuation. The probability to observe such an asymmetry can be calculated from the Poisson distribution. If combining the data from the original simulation and the first test simulation, we will effectively have 2 events on one side and 14 on the other side of the bottom (This is because the sample

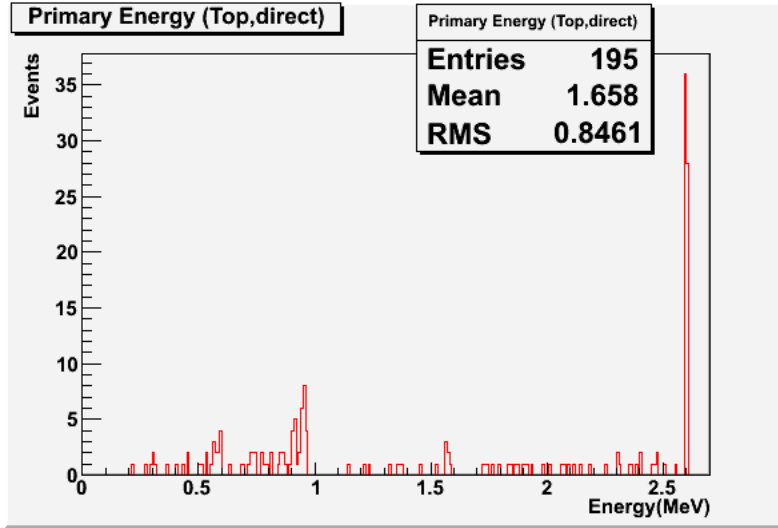
size 500 million is the number of events started in the left half of the bottom in a 2.5 billion events overall run. If assuming the depositions are proportional to the sample size, a 2.5 billion events run will yield  $9 \times 2.5/4 \approx 5$  events on the right half of the bottom. So if the contribution from both the actual 4 billion events run and the hypothetic 2.5 billion events run are summed up, they effectively lead to a result of 2 events on the left half and 14 events on the right half of the bottom.). Then it is fair to assume that the expectation on each side is 8. Together with the knowledge of the Poisson distribution, this gives a probability of 1.4% to obtain at most 2 events and a probability of 1.7% to observe at least 14 events. Therefore the probability to see them concurrently would be 0.024%, or the product of individual probabilities. So even if the abnormal can be blamed to statistical problems, we are still very unlucky in this trial.

Besides the position distribution, the energy distribution of those primaries is also studied. The results for thorium gammas are shown in Figure 6.43. For the “Top” spectrum, the major peaks are identifiable and the distribution is extending to as low as a few hundred keVs. For the other plot, only the most important peak can be identified.

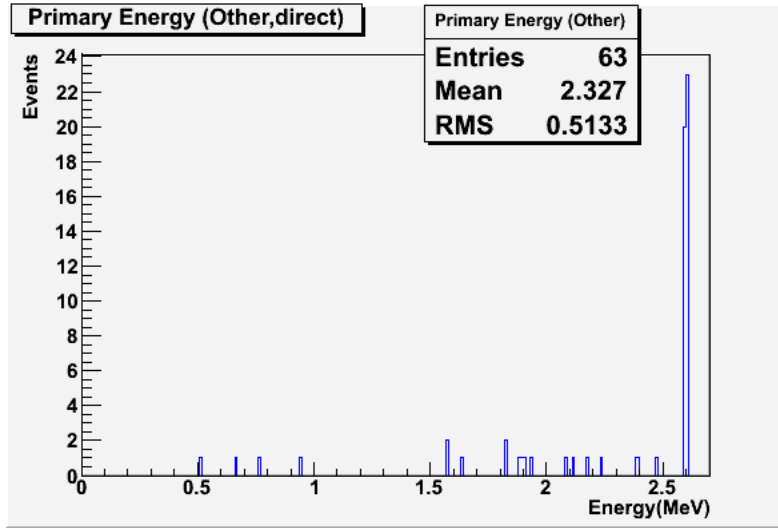
### **Gamma from the water shield**

Radioactivity from the water shield may also be a problem if the water used is not satisfactorily purified. Besides  $^{40}\text{K}$  and the uranium and thorium chains as a whole, we study in particular the effect of radon. Radon is especially important because it can easily be introduced from the laboratory air.

In the radon simulation, the entire set of gammas emitted from the main gamma emitters ( $^{214}\text{Bi}$  and  $^{214}\text{Pb}$ ) in the radon decay chain, which includes hundreds of gam-



(a) Top region; directly hit events



(b) Other regions

Figure 6.43: Energy distribution of the initial thorium chain gammas in the selected regions. The  $2.615\text{ MeV}$ ,  $583\text{ keV}$  gamma from  $^{208}\text{Tl}$  and the  $1.588\text{ MeV}$ ,  $911\text{ keV}$  gamma from  $^{228}\text{Ac}$  can be clearly identified on (a). Confined by statistics, only the  $2.615\text{ MeV}$  peak is identifiable from the other plot.

mas with distinct energy are considered, while in the thorium, uranium and potassium simulations, they used the same choice of gammas as in the previous laboratory wall simulations.

Figure 6.44 shows the radon induced detector depositions. Plots of depositions

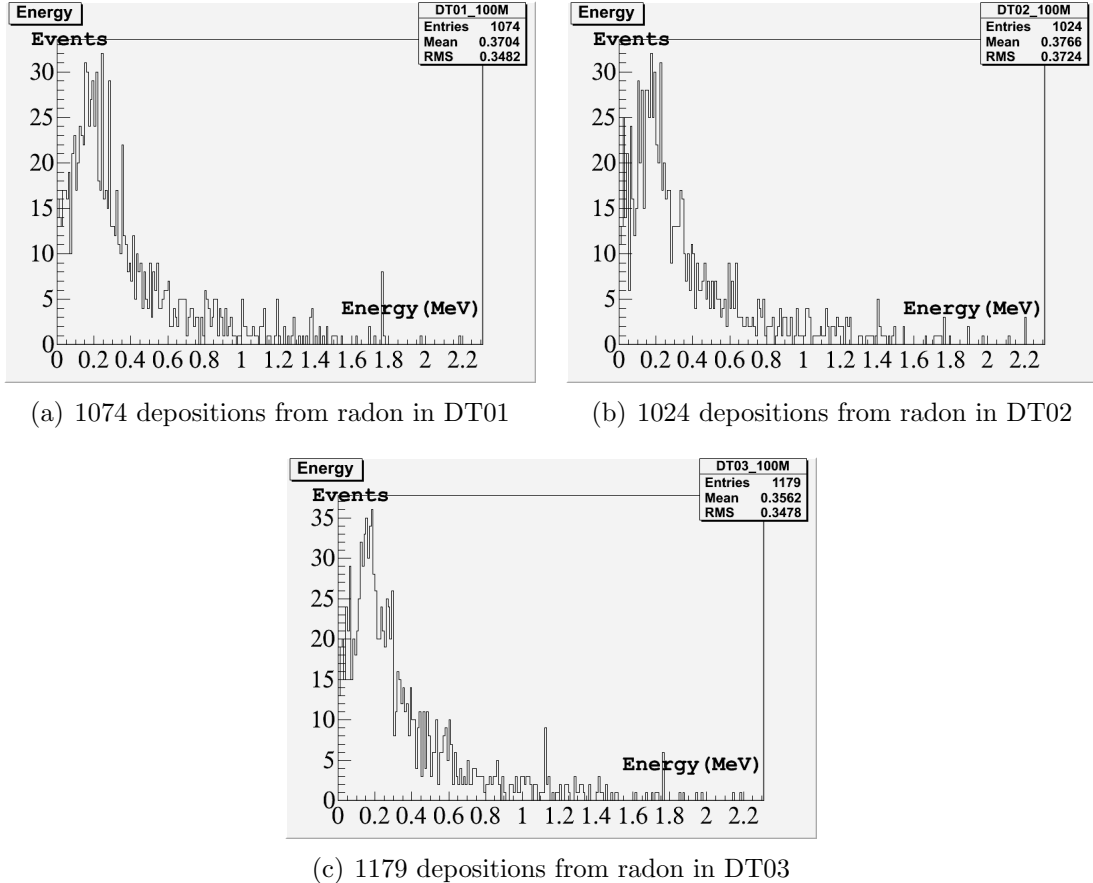


Figure 6.44: Detector depositions from radon contamination in the water shield.

from other sources are omitted due to similar features. The corresponding detector rates are listed in Table 6.11. Given the radon level in the SNOLAB air of typically  $\sim 100 \text{ Bq}/\text{m}^3$  [56] and the the radon solubility in water ( $\sim 0.1$ ), the radon induced detector rate is thus negligible. As to others, the thorium/uranium/potassium contamination level has to be controlled to less than  $0.1/0.02/0.01 \text{ ppm}$  to ensure the respective detector rate below  $0.1/\text{s}$ , the upper limit of the detector rate for each of the radioactive species considered. Fortunately, the contamination level that the SNO water purification system can reach at SNOLAB, which is  $\sim 5 \times 10^{-14} \text{ g/g H}_2\text{O}$  for thorium and  $\sim 20 \times 10^{-14} \text{ g/g H}_2\text{O}$  for uranium [67], is far better than the required purity level.

Table 6.11: Detector rates in all four water shield gamma simulations.

Source	Sample size	Equiv. time	Det.	Detector rate
Rn	100 million	$7.4 \text{ hours}/(\text{Bq}/\text{m}^3)$	1	4.02E-4 /s/(Bq/m <sup>3</sup> )
			2	3.84E-4 /s/(Bq/m <sup>3</sup> )
			3	4.42E-4 /s/(Bq/m <sup>3</sup> )
Th	100 million	$11 \text{ min}/\text{ppm}$	1	1.84 /s/ ppm
			2	1.59 /s/ ppm
			3	1.77 /s/ ppm
U	100 million	$3.4 \text{ min}/\text{ppm}$	1	3.92 /s/ ppm
			2	3.55 /s/ ppm
			3	4.29 /s/ ppm
<sup>40</sup> K	100 million	$10 \text{ s}/\text{ppm}$	1	10.8 /s/ ppm
			2	10.1 /s/ ppm
			3	11 /s/ ppm

As to the  $^{60}\text{Co}$  hidden inside the steel tank, since its rate is so low according to the preliminary simulation, a more detailed simulation regarding it will be unnecessary.

#### 6.2.4 Conclusion

Table 6.12 shows a summary on all the detailed simulations, from which we could conclude that for the external activity we can reach the target rate with the proposed shield, while the SNO water is clean enough for the shielding and no extra radon precautions are necessary for the shielding water.

#### Uncertainty

For all the simulations, uncertainty is not included as part of the final result, which is prevented by the extreme long simulation time. To get the systematical uncertainty of a Monte Carlo simulation, one has to run the same simulation several times with different configurations to examine the importance of each parameter. In our application, simulations of the laboratory wall radiations generally need weeks of com-

Table 6.12: Summary on detailed simulations. The detector rate has been converted to equivalent one detector result. For the neutron simulation, the rate is calculated with nuclear recoils within the range of  $10\text{-}100\text{ keV}$ .

Type	Location	Source	Detector Rate	Total	Target
Gamma	Laboratory wall	Thorium	$0.048/s$	$0.421/s$	$1/s$
	Laboratory wall	Uranium	$0.019/s$		
	Laboratory wall	Potassium	$0.049/s$		
	Water shield	Thorium ( $0.1\text{ ppm}$ )	$0.100/s$		
	Water shield	Uranium ( $0.02\text{ ppm}$ )	$0.100/s$		
	Water shield	Potassium ( $0.01\text{ ppm}$ )	$0.100/s$		
	Water shield	Radon ( $10\text{ Bq}/m^3$ )	$0.005/s$		
Neutron	Laboratory wall	Spontaneous Fission & $\alpha\text{-n}$	$0.08/day$ ( $10\text{-}100\text{ keV}$ )	$0.08/day$	$1/day$

puting time to get enough statistics. And our simulation involves many parameters that could influence the result, such as physics list and shape of the laboratory wall. Therefore it is impossible to finish the uncertainty study within a reasonable amount of time without a further enhancement of the computing efficiency. However, it might make sense to make a reasonable guess of the relative importance of each possible uncertainty source.

**Geometrical effect** The most straightforward source of uncertainty is the geometrical effect, since in simulating the experimental setup, one will always simplify the geometry to some extent. In our application, the overall geometry is the combination of the laboratory wall and the cryostat.

For the laboratory wall, the actual one is a finitely long tunnel with many openings on the side wall and caps on both ends. Compared with the simplified laboratory wall in the simulation, which is an effectively infinitely long tunnel with single cross section, the real geometry would mean a larger space and effectively more corner regions. A larger space may not be a problem. This could be explained by putting a detector in the center of a spherical experimental area. If we increase the dimension

of the area and keep the particle flux per unit area of the wall a constant, then we will have more particles generated from the surface. But the particles that can reach the detector, which is characterized by the solid angle from any point on the wall towards the detector will be reduced. And since the increase of the overall particle flux goes as  $r^2$ , while the decrease of the solid angle for each point on the surface goes as  $\frac{1}{r^2}$ , their effects onto the detector rates are just canceled out, leaving the detector rates unchanged despite of the variation of the dimension of the experimental area. More corner regions, or an increased corner to flat surface area ratio may cause a problem for the neutron simulation. From Figure 6.37 we could clearly see that most of the detector depositions are contributed by neutrons below  $3\text{ MeV}$ . According to Figure 6.29, this is the energy up to which the corner region shows an average 10% excess in flux over the other regions. Weighted by the corner to entire surface ratio, which is about 10% in current geometry, this excess would result in about 1% more neutrons started from the corner than if the flat surface spectrum is used instead. Since in the neutron simulation the average surface spectrum (Figure 6.31) is used to generate the initial neutrons, the  $\sim 1\%$  corner excess is essentially redistributed to other places of the surface. If it is the top region where most of the detector depositions are generated, the  $\sim 1\%$  excess might result in a  $\sim 1\%$  overestimate of the total detector rate. So let's go back to the discussion of the influence of an increased corner to flat surface area ratio to the detector rate. If more corner regions are introduced to the geometry, a larger value of weighted neutron excess will be split among the entire surface and probably cause an overestimate of the detector rate with the same magnitude. However, this is not the case for the gamma simulations. From Figure 6.43, the gammas that can cause depositions in the detectors are mostly above  $500\text{ keV}$ . But the corner effect for gammas is only obvious below  $500\text{ keV}$  (Figure 6.22 and Figure 6.22). So an increased corner area would not affect the detector rate, as the excess gammas can

hardly ever reach the detectors.

For the cryostat, many details such as the flanges are omitted in the simulated geometry. If more material is put into the upper part of the geometry, the detector depositions coming from the top will certainly be reduced. To estimate the effect of current cryostat geometry on stopping the top flux, the position distribution of the primary vertices in the preliminary neutron study (Figure 6.45) is used to compare with the one from the detailed neutron simulation (Figure 6.36). The preliminary work shows about 50 deposited events generated from above the water height and 20 from below, while the detailed simulation shows about 55 from the top region and 15 from other places. It is a surprising result since in the preliminary study the cryostat is essentially not existed. It means that the current geometry of cryostat is not beneficial in preventing the top flux or only contributes a little on this behalf. If we make a very extreme assumption that we could add extra material to the top of the cryostat in a way that the top shielding is as good as anywhere else, we could reduce the detector depositions from the top to the level in other regions. Taking the neutron simulation as an example, this would mean the 55 deposited events started from the top will be reduced to 10 or even 5 as observed in the bottom or wall regions. This then gives a 40%-50% change of the total depositions. However, this condition is very unlikely, because it means you have to put about  $1\text{ m}^3$  water above the cryostat despite of the fact that you will always have a hole on the top of the cryostat.

**Physics list** Physics list, or the set of physics processes one adopts in the simulation is also a main source of uncertainty. However because the physics processes are so complicatedly involved into the particle transportation and interaction, it becomes very hard to qualitatively speculate the influence of adopting different physics lists to the simulation. However, the very good agreement of our test simulations (see section

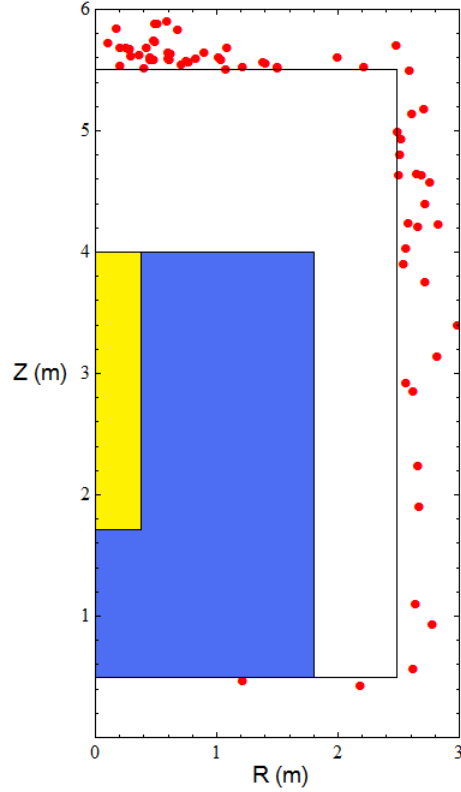


Figure 6.45: position distribution of the primary vertices in the preliminary neutron study. Since the preliminary experimental hall is a cylinder, the distance  $r$  between each vertex and the central axis is calculated. Then the whole set of vertices can be plotted on the  $r$ - $z$  plane. The  $z$  axis here indicates the central axis of the cylinder.

4.2.2) with measured values shows that the uncertainty of the model is at most in the few percent range.

### Work from other authors

For my study, there are other people who also work on similar topics. For instance, the work by E. Tziaferi et al. [68] whose aim is to measure low intensity fast neutron background from rock at the Boulby Underground Laboratory. As part of the main experiment, they did a GEANT4 simulation with thorium and uranium chain  $\alpha$  induced neutrons starting inside the rock volume. The simulated neutrons then

transported outside the rock, passing through a passive shield (Cu and Fe), and were expected to give proton recoils in the detectors. The whole process including the primary particles (their initial neutron spectrum is also calculated by SOURCES) and the different stages the particles have to go through before reaching the detector is very similar to my study. To validate the GEANT4 simulation, they set up a calibration  $^{252}\text{Cf}$  source beside the shield and measured the energy depositions of its neutrons. From the comparison between these two approaches, they found a 11% difference between the produced proton recoil spectra. This is a very small discrepancy, indicating GEANT4 can work satisfactorily in this kind of application.

# Chapter 7

## Summary

To prepare for the construction of the STF at SNOLAB, a set of Monte Carlo simulations has been run with different experimental configurations. Firstly, a very simple setup was used in the simulation, the result from which showed that the proposed background radiation shielding strategy was capable of reducing external background gammas and neutrons to an acceptable level. With the results of these preliminary simulations, the design of the water shielding could be finalized and the respective water tank was purchased.

To better understand how various types of background radiation impact the detectors and also generate simulation results that could be compared with future actual experimental data, much more detailed simulations were carried out in the second stage. Although the geometry implemented was still only an approximation to the real situation, it was certainly a more truthful representation than the one used in the preliminary study. In the gamma simulations, the nearly entire thorium and uranium decay chains and potassium gammas were considered, while the neutron spectrum was generated by SOURCES, rather than the simplified code used in the preliminary work. A stack of three detectors was included in the simulation, not only enabling

a study of multiple scattering in nearby detectors but also effectively increasing the statistics of the simulation. The three detector result can be handily converted into one detector result, though the approach was slightly different between the gamma and the neutron situations, which is to match the cases of one detector run in the future real experiment. It can be observed that the results from the second stage simulations are similar to that from the preliminary study, which confirmed the previous conclusion in the early stage and also potentially indicated the well-functioning of both simulations.

# Bibliography

- [1] M. Kowalski et al. Improved Cosmological Constraints from New, Old, and Combined Supernova Data Sets. *Astrophysical Journal*, 686(2):749–778, 2008.
- [2] F. Zwicky. Die Rotverschiebung von extragalaktischen Nebeln. *Helvetica Physical Acta* 6, pages 110–127, 1933.
- [3] V. Rubin and W. Kent Ford. Rotation of the Andromeda nebula from a spectroscopic survey of emission regions. *Astrophysical Journal*, 159:379–407, 1970.
- [4] Y. Sofue and V. Rubin. Rotation Curves of Spiral Galaxies. *Annual Review of Astronomy and Astrophysics*, 39:137–174, 2001.
- [5] D. Clowe et al. A Direct Empirical Proof of the Existence of Dark Matter. *The Astrophysical Journal Letters*, 648(2), 2006.
- [6] G. R. Blumenthal et al. Formation of galaxies and large-scale structure with cold dark matter. *Nature*, 311:517–525, 1984.
- [7] J. Dunkley et al. Five-year wilkinson microwave anisotropy probe observations: likelihoods and parameters from the WMAP data. *The Astrophysical Journal Supplement Series*, 180(2), 2009.

- [8] M.R. Nolta et al. Five-year wilkinson microwave anisotropy probe (WMAP) observations: Angular power spectra. *Astrophysical Journal Supplement Series*, 180:296–305, 2009.
- [9] S. Burles, K. Nollett, and M. Turner. What is the big-bang-nucleosynthesis prediction for the baryon density and how reliable is it? *Physics Review D*, 63:063512, 2001.
- [10] P. Tisserand et al. Limits on the Macho Content of the Galactic Halo from the EROS-2 Survey of the Magellanic Clouds. *Astronomy and Astrophysics*, 469:387–404, 2007.
- [11] Tai Tsun Wu and C. N. Yang. Phenomenological Analysis of Violation of CP Invariance in Decay of  $K^0$  and  $\bar{K}^0$ . *Physical Review Letters*, 13:380–385, 1964.
- [12] R. D. Peccei and H. R. Quinn. CP Conservation in the Presence of Instantons. *Physics Review Letter*, 38:1440–1443, 1977.
- [13] L. D. Duffy et al. A high resolution search for dark-matter axions. *Physics Review D*, 74:012006, 2006.
- [14] R. Gaitskell. DIRECT DETECTION OF DARK MATTER. *Annual review of nuclear science*, 54:315–359, 2004.
- [15] G. Servant and T.M.P. Tait. Is the lightest Kaluza-Klein particle a viable dark matter candidate? *Nuclear Physics B*, 650:391, 2003.
- [16] E. Kolb and M. Turner. *The Early Universe-reprints*. Addison-Wesley, 1989.
- [17] H. Georgi and S. Dimopoulos. Softly broken supersymmetry and SU(5). *Nuclear Physics B*, 193:150–162, 1981.

- [18] G. Jungman, M. Kamionkowski, and K. Griest. Supersymmetric dark matter. *Physics Reports*, 267:195–373, 1996.
- [19] H. Baer et al. Signals for minimal supergravity at the CERN Large Hadron Collider: Multijet plus missing energy channel. *Physical Review D*, 52:2746–2759, 1995.
- [20] B. C. Allanach et al. Searching for narrow graviton resonances with the ATLAS detector at the large hadron collider. *Journal of High Energy Physics*, 2000:JHEP09, 2000.
- [21] D. Rainwater T. Plehn and D. Zeppenfeld. Determining the Structure of Higgs Couplings at the CERN Large Hadron Collider. *Physical Review Letters*, 88:051801, 2002.
- [22] D. Hooper and E. Baltz. Strategies for Determining the Nature of Dark Matter. *Annual review of nuclear science*, 58:293–314, 2008.
- [23] W. de Boer, V. Zhukov C. Sander, A. V. Gladyshev, and D. I. Kazakov. The supersymmetric interpretation of the EGRET excess of diffuse Galactic gamma rays . *Physics Letters B*, 636:13–19, 2006.
- [24] F. W. Stecker, S. D. Hunter, and D. A. Kniffen. The Likely Cause of the EGRET GeV Anomaly and its Implications. *Astroparticle Physics*, 29:25–29, 2008.
- [25] D. Hooper and L. Goodenough. Dark Matter Annihilation in The Galactic Center As Seen by the Fermi Gamma Ray Space Telescope. arXiv:1010.2752v1, 2010.
- [26] F. Aharonian et al. HESS observations of the galactic center region and their possible dark matter interpretation. *Physics Review Letter*, 97:221102, 2006.

- [27] M. Kamionkowski, K. Griest, G. Jungman, and B. Sadoulet. Model independent comparison of direct versus indirect detection of supersymmetric dark matter. *Physics Review Letter*, 74:5174–5177, 1995.
- [28] J. Hall. New Dark Matter Limits from the Chicagoland Observatory for Underground Particle Physics (COUPP). In *Fermilab Wine and Cheese Seminar*, March 2010.
- [29] L. Baudis. Dark Matter Lecture 2: Principles of direct WIMP detection. BND Graduate School, Rathen, Germany, 2009.
- [30] J. Engel. Nuclear form-factors for the scattering of weakly interacting massive particles. *Physics Letters B*, 264:114–119, 1991.
- [31] V. Sanglard et al. Final results of the EDELWEISS-I dark matter search with cryogenic heat-and-ionization Ge detectors. *Physics Review D*, 71:122002, 2005.
- [32] G. Angloher et al. Commissioning run of the CRESST-II dark matter search. *Astroparticle Physics*, 31:270–276, 2009.
- [33] G. Angloher et al. Limits on WIMP dark matter using scintillating  $CaWO_4$  cryogenic detectors with active background suppression. *Astroparticle Physics*, 23:325, 2005.
- [34] E. Aprile et al. The XENON100 dark matter experiment at LNGS: Status and sensitivity . *Journal of Physics: Conference Series*, 203:012005, 2010.
- [35] M. Boulay and A. Hime. Technique for direct detection of weakly interacting massive particles using scintillation time discrimination in liquid argon. *Astroparticle Physics*, 25:179–182, 2006.

- [36] S. Archambault et al. Dark Matter Spin-Dependent Limits for WIMP Interactions on  $^{19}\text{F}$  by PICASSO. *Physics Letters B*, 682:185–192, 2009.
- [37] T. Saab and R. Clarke et al. Design of QET phonon sensors for the CDMS ZIP detectors. *Nuclear Instruments and Methods*, 444:300–303, 2000.
- [38] Z. Ahmed and D. Akerib et al. Results from the Final Exposure of the CDMS II Experiment. *Science*, 327:1619, February 2010.
- [39] J.D. Lewin and RF. Smith. Review of mathematics, numerical factors, and corrections dark matter experiments based on elastic nuclear recoil. *Astroparticle Physic*, 6:87–112, 1996.
- [40] R. W. Shonkwiler and F. Mendivil. *Explorations in Monte Carlo Methods*. Springer Science+Business Media, LLC, 2009.
- [41] G. Rubino and B. Tuffin. *Rare Event Simulation using Monte Carlo Methods*. John Wiley–Sons, Ltd., 2009.
- [42] CERN. *Geant4 User’s Guide for Application Developers Version geant4 9.3*, 2010.
- [43] T. Perera. *The Limiting Background In a Dark Matter Search at Shallow Depth*. PhD thesis, Case Western Reserve University, 2002.
- [44] S. Kamat. *Extending the Sensitivity to the Detection of WIMP Dark Matter with an Improved Understanding of the Limiting Neutron Backgrounds*. PhD thesis, Case Western Reserve University, 2005.
- [45] J. O. Johnson and T. A. Gabriel. *Micap: A Monte Carlo Ionization Chamber Analysis Package*, Feburary 1993.

- [46] GEANT4 collaboration. 20 MeV neutrons on Gd: High Precision Neutron model. [http://geant4.web.cern.ch/geant4/results/validation\\_plots/thin\\_target/hadronic/low\\_energy/test1/low\\_energy\\_n.shtml](http://geant4.web.cern.ch/geant4/results/validation_plots/thin_target/hadronic/low_energy/test1/low_energy_n.shtml), March 2007.
- [47] E. Browne and R. B. Firestone. *Table of Radioactive Isotopes*. Wiley-Interscience Publication, 1986.
- [48] Rinard P.M. Neutron interactions with matter. LA-UR-90-732 357-377, In Passive Nondestructive Assay of NuclearMaterial, Los Alamos Technical Report NUREG/CR-5550, 1991.
- [49] Evaluated Nuclear Data File (ENDF). <http://www.nndc.bnl.gov/sigma/>. National Nuclear Data Center, Brookhaven National Laboratory.
- [50] R. W. Ogburn IV. *A Search for Particle Dark Matter Using Cryogenic Germanium and Silicon Detectors in The One- and Two-Tower Runs of CDMS-II at Soudan*. PhD thesis, Stanford University, 2008.
- [51] K. Ruddick. MINOS Internal Note, 1996. NuMI-L-210.
- [52] S. Eichblatt. Estimating the Neutron Background from Natural Radioactivity in the Soudan Mine, 1997. CDMSNote 9701011.
- [53] J. A. Formaggio and C.J. Martoff. BACKGROUNDS TO SENSITIVE EXPERIMENTS UNDERGROUND. *Annual Review of Nuclear and Particle Science*, 54:361–412, 2004.
- [54] D.-M. Mei and A. Hime. Muon-induced background study for underground laboratories. *Physical Review D*, 73:053004, 2006.

- [55] D. S. Akerib et al. Present Status of the SuperCDMS program. *Low Temperature Physics*, 151:818–823, 2008.
- [56] SNOLAB. *SNOLAB User's Handbook revision 2*, 2006.
- [57] R. Heaton et al. Neutron Production from Thick-Target ( $\alpha$ -n) Reactions. *Nuclear Instruments and Methods in Physics Research A*, 276:529–538, 1989.
- [58] Segrè E. *Nuclei and particles: an introduction to nuclear and subnuclear physics*. Reading, Massachussetts: Benjamin-Cummins, 2nd edition, 1977.
- [59] W. Charlton. Sources: A code for calculating (alpha, n), spontaneous fission, and delayed neutron sources and spectra . *Progress in Nuclear Energy*, 51:608–613, 2009.
- [60] R. Heaton et al. Alpha-induced neutron activity in materials. *Nuclear Geophysics*, 4:499, 1990.
- [61] R. Heaton. Neutron shielding calculations for the sno detector. Master's thesis, Queen's University, 1988.
- [62] E. Chi. 3D layout of SNOLAB. Technical report, SuperCDMS collaboration, 2010.
- [63] Y.A. Akovali. NDS 76,127 (1995).
- [64] C. Lewis et al. Solubility of Radon in Selected Perfluorocarbon Compounds and Water. *Industrial and engineering chemistry research*, 26:356–359, 1987.
- [65] ILIAS. Radiopurity of Materials. <http://radiopurity.in2p3.fr/search.php?Material=Steel>.

- [66] Uranium and Thorium decay chains. [http://hepwww.rl.ac.uk/ukdmc/  
Radioactivity/UTh\\_chains.html](http://hepwww.rl.ac.uk/ukdmc/Radioactivity/UTh_chains.html).
- [67] The SNO Collaboration. Electron Energy Spectra, Fluxes, and Day-Night Asymmetries of 8B Solar Neutrinos from the 391-Day Salt Phase SNO Data Set. *Physics Review C*, 72:055502, 2005.
- [68] E. Tziaferi et al. First measurement of low intensity fast neutron background from rock at the Boulby Underground Laboratory. *Astroparticle Physics*, 27:323–338, 2007.